Quantitative Analysis of the Evolution and Reorganization of Microstructure in Primates

By

Daniel James Miller

Dissertation

Submitted to the Faculty of the

Graduate School of Vanderbilt University

in partial fulfillment of the requirements

for the degree of

DOCTOR OF PHILOSOPHY

in

Psychology

August 11, 2017

Nashville, Tennessee

Approved:

Jon H. Kaas, Ph.D.

Troy A. Hackett, Ph.D.

Anita Disney, Ph.D.

Geoffrey F. Woodman, Ph.D.

Acknowledgments:

I'd like to thank the entire Kaas lab and the animal care personnel for technical support, and in particular I'd like to thank Robert Friedman, Iwona Stepniewska, Huixin Qi, Chia-chi Liao, Jamie Reed, Mary Feurtado, and Pooja Balaram for their inclusion and guidance in everything from basic histology to sterile surgery.

I'd like to thank the Vanderbilt Institute for Digital Learning, and in particular Dr. Ole Molvig, for their financial support and encouragement in the pursuit of novel digital tools.

I'd like to thank Blaise Andrew Gratton for building Anatolution; his creativity in problem solving all the issues encountered when constructing the website made it possible to deploy this digital learning tool to train students and cross-validate the results presented in this work.

I'd like to thank Dr. Chet C. Sherwood for introducing me to comparative neuroanatomy and for teaching me the basics of histology and stereology.

I'd like to thank Dr. Troy A. Hackett for his unrelenting skepticism and unerring advice regarding the vagaries of anatomical research.

I'd like to thank Dr. Jon H. Kaas for all of his advice, enduring support and encouragement throughout the development of this thesis.

TABLE OF CONTENTS

LIST OF TABLES

LIST OF FIGURES

CHAPTER 1

OUTSTANDING ISSUES IN NEUROANATOMY

Introduction

One of the primary goals in neuroscience is to elucidate the relationship between the brain and behavior, which ultimately requires a combination of structural and functional information about the physiological modules that constitute the nervous system. However, the relationship between brain structure and function is plural, and descriptions of circuitry extends from the level of genes and gene products to the cellular aggregates which form entire neurological systems. Accordingly, the anatomical details which inform our understanding of circuit function are varied, and range from measurements of cellular anatomy in some of the oldest and most widely used histological procedures, to noninvasive measurements using recently developed technology, to minute observations of the size and location of connections between cell subtypes. In this dissertation, we are primarily concerned with anatomical measurements of cellular morphology available with the light microscope. Thus, we present data reflecting the myriad molecular cascades which result in modified cellular anatomy, and which are presumed to correlate with changes in physiological signaling.

Around the turn of the 20th century, the scientific community was in the midst of evaluating whether and how cell theory, the notion that all organisms ultimately consist of cells, might apply to the nervous system (Jones, 2007). Some scientists, such as Camillo Golgi, supported the 'reticular' view of nervous system organization which proposed (cytoplasmic) continuity between cells as the mechanism of brain function (Guillery, 2007). However, increasingly powerful microscopes with higher optical resolution combined with the advent and continued refinement of Golgi's silver impregnation method by investigators like Santiago Ramon y Cajal (Lopez-Munoz et al., 2006) led to a series of observations suggesting that 'discontinuities' between cells (i.e. synapses) was the standard of cellular organization in the brain (Yuste, 2015). Around the same time, Cecile and Oskar Vogt lead a team of researchers including Korbinian Brodmann to use details of cellular anatomy as the basis of an encompassing, holistic description of the structural subdivisions of the brain. The Vogts are now famous for coining the terms 'cytoarchitecture' and 'myeloarchitecture' to refer to descriptions of cellular bodies and myelinated axons, respectively, and which they ultimately used as the basis for their structural map of the nervous system. The Vogts and their collaborators set out to provide a systematic map of the brain to allow subsequent investigators using physiological methods a way to directly compare their observations in order to improve our understanding of the brain, both its evolution as well as its disorder in disease. The advent of noninvasive methods like magnetic resonance imaging (MRI) has returned some focus to anatomical maps of the brain, and the application of quantitative methods such as stereology hold great promise to improve the precision and accuracy of these maps, which were initially largely disregarded by other investigators for a lack of transparency and reproducibility (Nieuwenhuys, 2013). As Cajal's calibrations of Golgi's method and exquisite attention to the details visible with improving microscope technology lead to a more sophisticated understanding of neurobiological organization (i.e. the 'neuron doctrine'), so too do contemporary quantitative methods hold great promise to move our understanding of the relationship between the brain and behavior forward by enabling transparency and reproducibility (Zilles & Amunts, 2009).

Despite the great promise of applying novel methods to questions of fundamental importance to our understanding of the brain, many logistical limitations constrain their direct application and interpretability (Amunts & Zilles, 2015; Herculano-Houzel et al., 2015). For example, stereological methods were developed through collaborations among biologists and mathematicians to increase the precision of estimates of 3D objects only available through 2D planes of focus (i.e. objects visible under a microscope). Despite the widespread adoption and utility of design-based or stereological methods, the

increased precision comes at the significant price of rigorous experimental design (Mouton et al., 2002; Schmitz & Hof, 2005). For instance, stereological methods require that objects be relatively homogenous, or in other words that the objects to be investigated are normally distributed and have an equal probability of being sampled – which is actually more difficult to achieve than might be at first apparent (Geuna & Herrera-Rincon, 2015). Stereological investigations are only unbiased when the objects of interest can be unambiguously identified, for example through immunolabeling (Giannaris & Rosene, 2012) or a combination of morphological criteria (Lewitus et al., 2012; Garcia-Cabezas et al., 2016), and when a single feature of each object is used for measurements or counting (Gundersen et al., 1988). Such stringent criteria thus require highly trained investigators to spend precious time looking through the microscope, or more laborious and time-intensive histological procedures to visualize discrete cellular anatomical features of interest. It is unsurprising then that a great deal of effort has gone into automating these types of analyses, or in streamlining a specific set of procedures to answer a single question. As an example of the latter, the isotropic fractionator was developed in an effort to streamline tissue processing in order to more quickly and cheaply count cells of different types (Herculano-Houzel & Lent, 2005). This method also has the additional advantage of being compatible with automated cell counting procedures such as flow cytometry, at the increased cost of the requisite reagents and instrumentation (Collins et al., 2010). However, the isotropic fractionator dissolves and homogenizes samples of interest, which results in a loss of spatial information that may be of value to the investigator. Similarly, because studies employing the isotropic fractionator method dissect samples prior to histological processing, it is often difficult or impossible to correctly and reliably identify a specific anatomical region of interest (ROI) for analysis (Herculano-Houzel et al., 2015). Given these limitations, other investigators (Inglis et al., 2008) have tried to use recent advances in computer vision to identify and measure anatomical samples using the traditional slice-based methods which retain spatial information and thus suffer from violating the assumption of homogeneity which entails more laborious sampling procedures (Avendano & Dykes, 1996b; Giannaris & Rosene, 2012). However, strategies deploying computer-vision procedures suffer from a lack of precision and sensitivity to variable morphological details in images crowded with non-target objects (such as artefactual staining, or when only a fraction of the objects within the image are under investigation), and recent analyses indicate poor performance compared to investigators trained in the recognition of these objects and which have the visual perceptive powers of the human retina (Schmitz & Hof, 2005). Taken together, these considerations make it clear that no single analysis fits all investigations, and that multiple trade-offs in the resources available and the research question to pursue lead the diligent investigator to consider mixed approaches.

In summary, although our understanding of the relationship between the structure and function of specific modules within the brain has seen great progress over the last century and more, in large part due to the development of novel technologies (Guillery, 2007), numerous issues remain outstanding, and each of them may require an alternative approach. In particular, the trade-off between precision and speed in the analysis of anatomical samples remains unresolved and investigators must largely choose one over the other. Furthermore, this trade-off occurs at multiple levels of the analysis, such that speed in dissection may produce increases in the precision of specific measurements, such as the absolute number of objects, while obfuscating others, such as their location within specific sensory systems. Similarly, the use of novel histological procedures may facilitate the identity of objects within a given circuit, but at a dramatic increase in cost of instrumentation and reagents. Finally, the use of computational strategies such as computer-vision procedures may, with significant investment in instrumentation and reagents, enable a relatively rapid analysis with an acceptable degree of accuracy, but even this synergy is inherently limited by the technical factors of skill in tissue processing, still requires the validation of a trained investigator, and is not applicable to the vast majority of specimens available for post-mortem analysis (Inglis et al., 2008). Thus, the analysis of neuroanatomical specimens is limited by a variety of technical and monetary constraints, and in the course of this dissertation we explore some of these issues, identifying some solutions and proposing a variety of directions for future research.

Research Rationale

The aim of the present research was to evaluate the differential effect of specific methodological decisions to visualize regions and objects of interest in order to optimize the subsequent analysis of two archival collections where the type, number, and size of regions or objects of interest is thought to broadly correlate with circuit function.

First, we set out to evaluate the trade-offs among different approaches to tissue preparation and counting strategies in the pursuit of data on the cellular composition of brain samples. This was achieved by counting the number of neurons and glia in the primary visual field of the cerebral cortex (V1) in two hemispheres of a single chimpanzee, one of which was flattened for use with the isotropic fractionator and flow cytometry using fluorescent markers, the second of which was prepared using traditional slice-based procedures for stereology with a battery of histological stains on adjacent series of sections.
Next, we deployed an optimal strategy to collect two distinct types of information about brain samples: (A) to determine the evolution of the glia-to-neuron ratio in the primary geniculo-recipient layer 4 of V1 across primates; this was achieved by using a battery of histological stains in adjacent series of sections to identify V1 from adjacent fields and layer 4 within the cortical mantle, and to then count the number of neurons and glia. (B) Determine the cellular morphological effects of dorsal column lesions on the cuneate nucleus of the brainstem; this was achieved by using a batter of histological stains in adjacent series of sections to identify and measure the volume of the cuneate nucleus, as well as to count and measure the volume of neurons within the cuneate nucleus.

References

Amunts K, Zilles K. (2015) Architectonic mapping of the human brain beyond Brodmann. Neuron. Dec 16; 88(6):1086-07.

Avendano C, Dykes RW. (1996) Quantitative analysis of anatomical changes in the cuneate nucleus following forelimb denervation: a stereological morphometric study in adult cats. J Comp Neurol. July 8;370(4):491-500.

Collins CE, Young NA, Flaherty DK, Airey DC, Kaas JH. (2010). A rapid and reliable method of counting neurons and other cells in brain tissue: a comparison of flow cytometry and manual counting methods. Front Neuroanat. 4:5.

Garcia-Cabezas MA, John YJ, Barbas H, Zikopoulos B. (2016). Distinction of Neurons, Glia and Endothelial Cells in the Cerebral Cortex: An Algorithm Based on Cytological Features. Front Neuroanat. Nov 1;10:107.

Geuna S, Herrera-Rincon C. (2015) Update on stereology for light microscopy. Cell Tissue Res. Apr;360(1):5-12.

Giannaris EL, Rosene DL. (2012) A stereological study of the numbers of neurons and glia in the primary visual cortex across the lifespan of male and female rhesus monkeys. J Comp Neurol. Oct 15;520(15):3492-508.

Guillery RW. (2007). Relating the neuron doctrine to the cell theory. Should contemporary knowledge change our view of the neuron doctrine? Brain Res Reviews. Oct; 55(2):411-21.

Gundersen HJ, Jensen EB. (1987). The efficiency of systematic sampling in stereology and its prediction. J Microsc. 147(3):229-63.

Herculano-Houzel, S., Lent, R. (2005). Isotropic fractionator: a simple, rapid method for the quantification of total cell and neuron numbers in the brain. J Neurosci. 25(10):2518-21.

Herculano-Houzel S, von Bartheld CS, Miller DJ, Kaas JH. (2015). How to count cells: the advantages and disadvantages of the isotropic fractionator compared with stereology. Cell Tissue Res. Apr;360(1):29-42.

Inglis A, Cruz L, Roe DL, Stanley HE, Rosene DL, Urbanc B. (2008). Automated identification of neurons and their locations. J Microscopy. June;230(pt 3):339-52.

Jones EG. (2007). Neuroanatomy: Cajal and after Cajal. Brain Res Reviews Oct; 55(2): 248-55.

Lopez-Munoz F, Boya J, Alamo C. (2006). Neuron theory, the cornerstone of neuroscience, on the centenary of the Nobel Prize to Santiago Ramon y Cajal. Brain Res Bulletin. Oct 16; 70(4-6):391-405.

Lewitus E, Hof PR, Sherwood CC. (2012). Phylogenetic comparison of neuron and glia densities in the primary visual cortex and hippocampus of carnivores and primates. Evolution. 66(8):2551-63.

Mouton PR. (2002). Principles and Practices of Unbiased Stereology: An Introduction for Bioscientists (The Johns Hopkins Univ Press, Baltimore).

Nieuwenhuys R. (2013). The myeloarchitectonic studies on the human cerebral cortex of the Vogt-Vogt school, and their significance for the interpretation of functional neuroimaging data. Brain Struct Funct. Mar; 218(2):303-52.

Schmitz C, Hof PR. (2005). Design-based stereology in neuroscience. J Neurosci. 130(4):813-31.

Yuste R. (2015). On testing neural network models. Nat Rev Neurosci. Dec; 16(12):767.

Zilles K, Amunts K. (2009). Receptor mapping: architecture of the human cerebral cortex. Cur Opin Neurobio. Aug; 22(4):331-9.

CHAPTER 2

COMPARISON OF METHODS

Introduction

Determining the cellular composition of neurobiological tissue is critical to our understanding of the structure and function of the brain. Differences in the organization of neurobiological tissue, whether it is the arrangement of cells or the relative amount of an organism's nervous system dedicated to a particular sensory modality, are important components of the neurobiological circuitry underlying behavior (Catania et al., 1993; Krubitzer et al., 1995; Sur et al., 1980).

Scientists have employed a variety of techniques with varying degrees of success to more fully characterize the microstructure and circuitry of specific brain areas and systems. An early example of such a procedure is "direct enumeration," which consists of homogenizing brain tissue and determining the density of cell nuclei in re-suspended fluid samples (Nurnberger & Gordon, 1957; Zamenhof, 1976). A major critique of this approach was concern over the potential loss of cells or nuclei during the mechanical dissociation of tissue (Clarke & Oppenheim, 1995). Alternative procedures were developed to analyze specific parameters of sectioned tissue samples, and since the 1960's these stereological techniques have become the gold-standard for quantitative investigations of biological tissues (Glaser & Glaser, 2000). However, stereological methods have also been critiqued for inattention to tissue processing deformations that may lead to inaccurate estimates (von Bartheld, 2002). Traditionally, for example, guard zones were used to avoid tissue containing "lost caps" that resulted from cells being destroyed by direct contact with the knife blade (Baryshnikova et al., 2006). However, recent work suggests the absence of "lost caps" in fixed tissues cut on a freezing microtome, but reports that the distribution of particles along the z-axis (from one cut edge to the other) is non-uniform, concluding that the traditional use of guard zones may introduce bias into the estimate for these tissues (Carlo & Stevens, 2011). Indeed, tissue deformations that introduce bias into stereological investigations have been reported for a number of tissue processing protocols and constitute a major cause for concern (Von Bartheld, 2012). Thus, the extent to which these distinct methodologies produce accurate estimates of specific biological parameters of interest remains controversial (Bahney & von Bartheld, 2014). Accordingly, whether these methods produce comparable results has also been of interest for several decades as agreement between methods provides support for the conclusion that we are, in fact, producing reasonable estimates of a specific biological parameter of interest, and forms the motivation for our work. An additional challenge to this type of work is the ability to accurately identify the region of interest for quantitative analysis. Immunohistochemical preparations have enhanced our ability to identify discrete brain areas by providing information on an increased number of the molecular properties of the brain (Balaram et al., 2013; Raghanti et al., 2008; Sherwood et al., 2007; Takahata et al., 2009). Indeed, stereological analysis has seen widespread success in part because of the ability to employ immunohistochemical protocols to tag neurons (Mullen et al., 1992) as well as histological procedures to visualize cells, including the Nissl stain (Miller et al., 2012), and neurotransmitter biomarkers, such as acetylcholinesterase (Miller et al., 2013), in adjacent brain slices. Not only does this increased number of staining procedures give researchers more to investigate with the techniques at their disposal, it also provides an enriched view of the neurobiology under investigation and facilitates the rapid and reliable identification of brain areas. Importantly, recent years have witnessed the application of some of these newer technologies to older procedures. For example, the isotropic fractionator (Herculano-Houzel & Lent, 2005) is the product of combining "direct enumeration" with immunohistochemistry to investigate, for example, the number of neuronal and non-neuronal cells in a tissue sample. In addition, results from manual counts using the isotropic fractionator method (Herculano-Houzel & Lent, 2005) have been replicated using modern flow cytometry to more rapidly quantify the cellular composition of

neurobiological samples, termed the flow fractionator (Collins et al., 2010; Young et al., 2012). A principal reason these procedures have seen widespread use in recent years is that each has specific advantages. For instance, while stereological analysis of brain slices provides a wealth of anatomical detail, the preparation of histological sections is time-consuming, and adequately sampling brain tissue can be challenging. Conversely, the isotropic fractionator can more rapidly produce reliable estimates of some of the same parameters, such as the cellular composition of a brain sample, via homogenization of samples (Herculano-Houzel & Lent, 2005). Recently, the use of flow cytometry to automatically count samples prepared using the isotropic fractionator was demonstrated to further decrease the amount of time necessary to estimate cellular populations, and to provide results less variable than those obtained from hand counts using a microscope, although with an increased equipment cost (Collins et al., 2010; Young et al., 2012). Furthermore, although stereological studies can employ a range of histological markers to identify individual regions of interest, the isotropic fractionator and flow fractionator can each be used for samples taken from cortex that has been separated from the white matter and flattened into a sheet, in which specific brain areas, such as the primary visual cortex (V1), are readily identifiable during dissection. Despite the theoretical ability of these procedures to estimate the same parameters, no study has to-date directly compared results from the use of the isotropic fractionator, the flow fractionator and the stereological optical fractionator in a single brain region.

The present study is therefore the first to investigate the similarity of estimates obtained using the isotropic fractionator, the flow fractionator and the stereological optical fractionator from a specific region of the brain within a single individual. We determined the total number of cells by staining free-floating suspensions of nuclei for DNA with 4',6-diamidino-2-phenylindole (DAPI), and the percentage of neuronal cells by staining suspensions of nuclei with both DAPI and an antibody to the neuronal nuclei marker NeuN (Mullen et al., 1992) in samples from flattened V1 of the right hemisphere using the isotropic fractionator (Collins et al., 2010; Herculano-Houzel & Lent, 2005; Young et al., 2012). We then determined the total number of cells and the percentage of neuronal cells in the same samples with the flow fractionator (Collins et al., 2010; Young et al., 2012). Finally, we recorded the location of cells along the z-axis to determine the presence and extent of possible non-uniform tissue shrinkage that could bias our stereological estimates, and calculated the total number of cells and neurons using the stereological optical fractionator (Schmitz & Hof, 2005) in adjacent series of brain slices from the left hemisphere stained for Nissl substance or NeuN, respectively. Determining the agreement in results between these methods is important because each of these methods are in current use and the reliability of our conclusions and inferences based upon such data will depend upon how they compare. In addition, if estimates from these methods agree, this will provide investigators with a greater degree of experimental flexibility and increase the data to which they have access when interpreting their results. In short, determining the transparency of results from these techniques facilitates the integration of a larger set of data in the development of formal relationships between the cellular composition and behavioral function of brain regions across a broad range of taxa and in both clinical and basic scientific applications.

Materials & Methods

Sample

Both hemispheres of the brain from a single, non-neuropathological adult female chimpanzee (*Pan troglodytes*; 53 years) were obtained from the Texas Biomedical Research Institute's Southwest National Primate Research Center. The brain was collected after post-mortem flushing with 0.1% phosphate buffered saline (PBS), and was shipped overnight in 0.1% PBS. Upon arrival, the cerebral cortex was separated from the subcortical structures, bisected and then cleaned of vasculature and pia. In the right hemisphere, the sulci were opened in order to flatten the cortical sheet, which was then fixed in 2% PFA in PBS for 72 hours at 4 degrees Celsius. The left hemisphere was cut into blocks and fixed in 4% PFA in PBS for 24 hours at 4 degrees Celsius, followed by immersion in 30% sucrose overnight prior

to sectioning at 50 µm on a sledge microtome (American Optical, model #860, clearance angle = 19˚) while the tissue was held below 0 degrees Celsius.

Details of the tissue processing methods employed in flattening cortex and preparing samples for the isotropic fractionator protocol appear in prior publications (Collins et al., 2010; Herculano-Houzel & Lent, 2005; Young et al., 2012). Briefly, the flattened (right) cortical hemisphere was photographed and placed onto a light box. Primary visual cortex (V1 or Brodmann's area 17) in flattened cortex is easily identifiable when backlit due to its dense myelination and caudal position. Identifiable cortical areas (V1) were drawn on the printed image of the flattened cortex and V1 was separated from the rest of cortex and subdivided into pieces using a scalpel. Each piece was photographed, weighed and documented as a single sample. Photographs were taken in order to measure the surface area of each piece using ImageJ, which were combined with the average cortical thickness of V1 based upon measurements (mean depth = 1.8 mm, n=42) in serial sections from the left hemisphere to determine the volume of V1. Each sample from the flattened cortical tissue (n=61) was homogenized using a glass Tenbroeck tissue grinder (Fisher Scientific) in a dissociation solution of sodium citrate, triton-X 100 and distilled water. The total suspension volumes were determined based upon sample weight, and ranged between 3 and 5 ml. The resulting solution contains free-floating nuclei, which were stained with 4', 6-diamidino-2-phenylindole (DAPI), which indiscriminately stains cellular nuclei, and an antibody to Neuronal Nuclei (NeuN, MAB377, Millipore), which stains most neuronal nuclei (Mullen et al., 1992). The isotropic fractionator and flow fractionator procedures described below permit the estimation of total cell number as well as the percentage of neurons in the sample, assuming that each nucleus corresponds to one cell.

Isotropic Fractionator

Nuclei in samples from the flattened (right) V1 and processed using the isotropic fractionator were stained with DAPI and an antibody to NeuN and quantified by hand in a Neubauer counting chamber under a fluorescent microscope (Herculano-Houzel & Lent, 2005). Specifically, free-floating, DAPI-stained or DAPI+/NeuN+ double-stained nuclei from the main suspension samples were counted to estimate total cell number or percentage of neurons, respectively (Figure 1, Table 1). Initial manual counts of DAPI-stained or DAPI+/NeuN+ double-stained nuclei were performed by a technician blind to the flow cytometry data, and control samples revealed excellent agreement between the initial and final manual counts performed by DJM on DAPI-stained nuclei (nonparametric T-test, $P = 0.967$, n = 17), and between manual and flow counts of DAPI+/NeuN+ double-stained nuclei (nonparametric T-test, $P = 0.123$, n = 13). All suspensions were vigorously mixed prior to chamber loading and counting, and each of the 61 samples from right V1 was processed using the isotropic fractionator method.

Flow Fractionator

Nuclei in samples from the flattened (right) V1 and processed using the flow fractionator were stained with DAPI and an antibody to NeuN and quantified by a flow cytometer (Collins et al., 2010; Young et al., 2012). The flow fractionator also requires the addition of a known number of Countbright Beads (Invitrogen) (Young et al., 2012) (Figure 1). Specifically, free-floating, DAPI-stained or DAPI+/NeuN+ double-stained nuclei from the main suspension samples were counted in tandem with a fixed volume of fluorescent Countbright beads (Invitrogen Inc.) using a Becton Dickson 5-laser LSRII flow cytometer (for details, see Collins *et al.*, 2010; Young *et al.*, 2012) (Figure 1). All samples were vigorously mixed before counts were determined, and all counts were made in duplicate to assess variability. The flow cytometry technician was blind to the sample attributes prepared by DJM and to the manual count data. All flow cytometry experiments were conducted in the Vanderbilt University Medical Center Flow Cytometry Shared Resource. Each of the 61 samples from right V1 was processed in duplicate using the flow fractionator method.

Optical Fractionator

This study also employed a traditional histological procedure to reveal cell bodies based upon the presence of staining for Nissl-substance (Nissl), as well as immunohistochemical staining for NeuN (Young et al., 2013), in which V1 is easily identifiable (Figure 1), for stereological quantification. Specifically, adjacent 1-in-10 series of sections cut from the left hemisphere on a freezing sledge microtome were processed for Nissl-substance using 1% thionin acetate (T3387 Sigma-Aldrich) dissolved to 0.025% into an acetate buffer (containing sodium acetate and acetic acid to a pH of 5.1-5.5) after mounting on glass slides and dried overnight in an oven set to 37˚ Celsius, or free-floating with an antibody to NeuN. Sections were dehydrated in a graded series of alcohol (70%, 95%, 100%) followed by immersion in xylene prior to being coverslipped with Permount (SP15-500 Fisher). Neurons were apparent in both Nissl- and NeuN-stained materials because of the presence of a round nucleus. Glia were apparent in Nissl-stained sections because of their smaller size and darkly stained punctation. All stereological analyses were performed by a single investigator (DJM) using a computer-assisted stereology system consisting of a Nikon E80i light microscope with a motorized stage and the commercially available StereoInvestigator software (MicroBrightField Bioscience, Williston, VT). The volume of each region of interest was estimated using the Cavalieri principle (frame area = 500 µm × 500 µm) at 4× magnification (Table 1). An initial pilot study, in which sections were outlined at 2× magnification and counts were placed at 100× magnification using an oil immersion objective lens under Köhler illumination when the top of the nucleus, in the case of neurons, or the top of the cell profile, in the case of glia, came into focus within the probe dimensions (Schmitz & Hof, 2005), was performed to determine stereological parameters. Specifically, the pilot study indicated the appropriate number of sections to be investigated (n = 10), probe area (40 µm × 40 µm), probe height (10 µm), dual vertical guard zone height (2 µm), frame step (1966 µm × 2595 µm), frequency of thickness measurement (1 in 8; measured thickness: mean = 16.8 µm, SEM = 0.31 µm) while maintaining an acceptably low coefficient of error (Gundersen (m=1) CE < 0.025; 1st Schmitz & Hof CE < 0.024; 2nd Schmitz & Hof CE < 0.019) (Gundersen & Jensen, 1987; Schmitz & Hof, 2005).

In addition, these preliminary data indicated that the chromagens used to visualize cells or nuclei achieved full penetration of the tissue, based upon the homogeneity of cell counts across the depth of probes used to investigate NeuN-stained materials, and the failure to reject the null hypothesis, in Nissl-stained materials, that there was no difference in the number of cells allocated to sequential counting bins along the z-axis ($F(1,8) = 0.82$, $P > 0.39$, $n = 10$ bins for a probe depth of 10 µm). Additional analysis of the vertical (z) distribution of particles was performed at 100× magnification by recording the z-axis location of cells (nuclei; $n = 1399$) within the measured depth of tissue at sampling sites ($n = 207$) from across V1 in Nissl-stained material. A total of 640 sampling sites were investigated using the optical fractionator workflow to estimate cell and neuron number (mean number of sites per section = 32.4, 34.2; standard error of the mean (SEM) = 5.8, 4.8; NeuN, Nissl respectively). The number of cells or neurons was calculated by multiplying the number of counts by the reciprocals of the area section fraction (asf), serial section fraction (ssf) and the tissue section fraction (tsf) (Schmitz & Hof, 2005). The percent of neuronal cells in brain slices investigated using stereology was calculated by taking the number of cells estimated using NeuN-stained sections divided by the number of cells estimated using Nissl-stained sections.

Statistical Analysis

The goals of this project were (1) to determine if manual and automated methods of counting single and double-stained nuclei in suspension volumes of homogenized tissue samples resulted in statistically indistinguishable estimates of total cell and neuron numbers from readily identifiable regions of interest in flattened cortical preparations, (2) to compare these results with estimates of the same parameters in the same region of interest from the other hemisphere in a single individual using stereological procedures on sectioned tissue, and (3) to determine the distribution of particles in the z-

domain of Nissl-stained sections. Pursuant to the first goal, we determined manual counts as well as automated flow counts from at least two aliquots from each homogenized sample of flattened cortex used in this study (n = 61, Table 1). Next, we determined within-measures agreement by calculating the non-parametric T statistic on repeated measurements of each aliquot, testing the difference between means, such that a *P* value smaller than 0.05 was taken to indicate a significant difference between the measurements (Table 2). We then used the Bland-Altman (1986) approach of comparing the differences between the measurements to the means of the measurements in our analysis of the isotropic fractionator and the flow fractionator data (Supplementary Figures 1-4). In addition, we report Lin's concordance correlation, a statistic that approximates the variation of the data about the linear regression (Lin, 1989) (Table 2). Pursuant to the second goal of comparing results from samples of flattened cortex with results from coronal brain slices, we calculated the density of cells or neurons per cubic millimeter by taking the parameter estimate of the sample divided by the measured volume of that sample. For example, when using the optical fractionator, the investigator draws an outline of the region of interest in each of the 10 sections selected for analysis. The Cavalieri method then utilizes this outline to estimate the surface area of that section. The volume of the section is then calculated by taking the surface area multiplied by the thickness of the section as it was originally cut on the freezing microtome. The density of cells or neurons is then calculated by dividing the number of cells or neurons estimated using the optical fractionator by the volume of each section determined by the Cavalieri method. The 10 sections are then ordered by density. In contrast, the surface area of each flattened cortical sample was measured using ImageJ and multiplied by the depth of V1 cortex measured in the intact left hemisphere cut as brain slices to determine the volume of each sample. The average of the isotropic fractionator and flow fractionator estimates was then divided by the volume of each sample to calculate cell or neuronal density (Table 1). In addition, these averages were ordered by density and placed into 10 bins of approximately 6 samples each (the 10^{th} bin contained 7 samples). The non-parametric T statistic was then calculated on the ordered (a) flattened cortical sample and (b) intact brain section density estimates (Table 2). Pursuant to the third aim of determining the distribution of particles in the z-domain of brain slices from tissue fixed before sectioning while frozen on a sliding microtome, we normalized the z-axis location of each cell within the corresponding depth of the sampling site in which it was observed and divided this normalized data into 10 bins corresponding to percentiles of tissue depth. We then used linear regression to investigate the presence of a statistically distinguishable relationship between the frequency and location of cell counts along the z-axis.

Results

Our investigation of chimpanzee (*Pan troglodytes*) primary visual cortex (V1, Figure 1) revealed excellent agreement between the estimated number of cells or neurons derived from tissue processed as samples from flattened cortex and quantified manually using the isotropic fractionator (Herculano-Houzel & Lent, 2005) and automatically using the flow fractionator (Collins et al., 2010; Young et al., 2012), or from tissue processed as coronal sections and quantified using the computer-assisted optical fractionator method (Schmitz & Hof, 2005, Figure 2). Specifically, the stereological estimate (961 million) of total cell number from coronal slices of V1 was 94.6% of the estimate based upon manual and automated counts (1 billion) of flattened cortex. The percent of all the cells that are neurons, calculated from flattened samples (65.4%), was 90.3% of the percent estimated using stereology (72.4%). Manual and automated count estimates (658 million) of the number of neurons in V1 were 95.6% of the stereological estimate (695 million, Table 1).

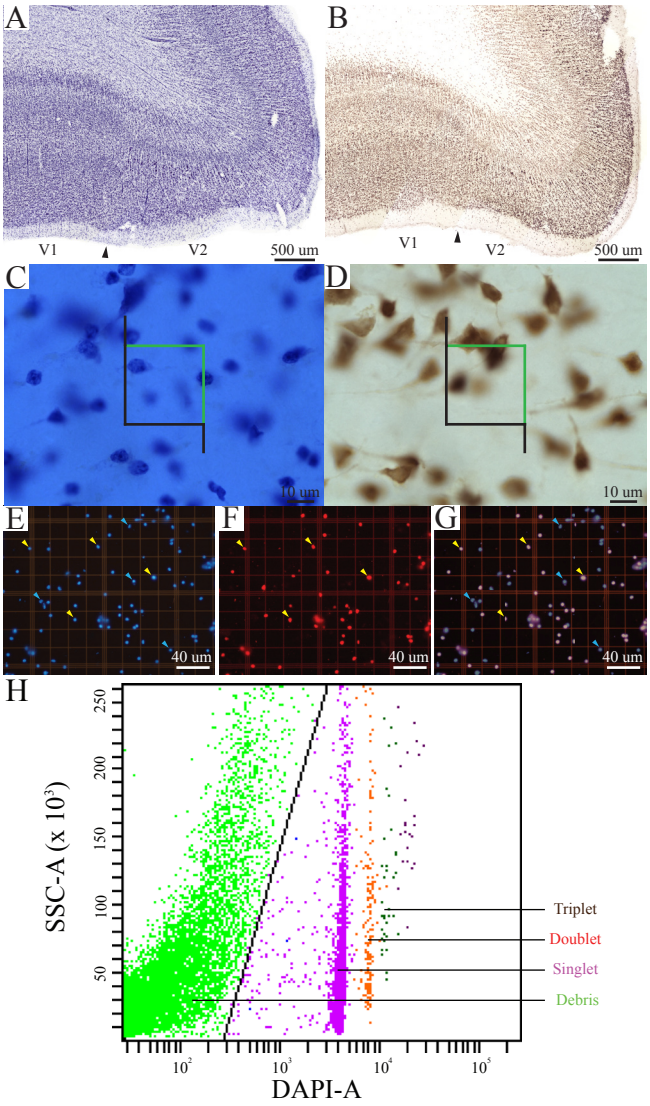

Figure 1. Summary figure of the optical, isotropic, and flow fractionator workflows.
Low magnification (~1×, scale bar = 500 µm) images of coronal brain slices at the V1/V2 cortical boundary (indicated by the arrowhead) stained for Nissl (A) and an antibody to NeuN (B) showing the characteristic laminar profile of V1 that was used to guide stereological measurements. High magnification images (100×, scale bar = 10 µm) of the outer stripe of Gennari in V1 in coronal brain slices stained for Nissl (C) and an antibody to NeuN (D), with the stereological probe illustrating lines of inclusion (green) and exclusion (black). High magnification (20×, smallest individual boxes are 50 µm by 50 µm, scale bar = 40 µm) images of flattened cortical samples processed using the isotropic fractionator and quantified using the Neubauer chamber (shown in E, F and G). Panel E shows DAPI-stained nuclei, panel F shows NeuN-stained nuclei and panel G is a merged image of panels F and G. Yellow arrowheads indicate nuclei double-positive for fluorescent staining of DAPI and NeuN, indicating neuronal nuclei, and blue arrowheads indicate nuclei that stained for DAPI, but did not stain for NeuN, indicating non-neuronal nuclei (E, F and G). Panel H shows an example of our data generated using the flow fractionator and presented on a SSC-A (side scatter area) vs. DAPI-A (DAPI-fluorescent area) scatterplot. A polygon gate was used to select the nuclei based on DAPI expression. This analysis profile allowed us to quantify the concentration of individual nuclei (singlet, teal), clusters of two nuclei (doublet, red) and clusters of

three nuclei (triplet, black) in a known volume of sample. The green dots on the left side of the plot indicate debris excluded by the polygon gate (black diagonal line).

Tissue	Quantification	Parameter	Sample	Estimate
Flat	Neubauer Chamber	All Cells	n = 61	998,480,148
Flat	Flow Cytometry	All Cells	n = 61	1,015,656,849
Slice	Optical Fractionator	All Cells	n = 324	961,086,450
Flat	Neubauer Chamber	Neurons	n = 61	651,739,214
Flat	Flow Cytometry	Neurons	n = 61	664,726,981
Slice	Optical Fractionator	Neurons	n = 316	695,478,260
Flat	Neubauer Chamber	Percent Neurons	n = 13	62.0 %
Flat	Flow Cytometry	Percent Neurons	n = 61	65.1 %
Slice	Optical Fractionator	Percent Neurons	n = 10	72.4 %
Flat	Image J	Volume (mm^3)	n = 61	5,275
Slice	Cavalieri (Nissl)	Volume (mm^3)	n = 10	4,819
Slice	Cavalieri (NeuN)	Volume (mm^3)	n = 10	4,778
Flat	Neubauer Chamber	Cell Density	n = 61	192,184
Flat	Flow Cytometry	Cell Density	n = 61	195,551
Slice	Optical Fractionator	Cell Density	n = 10	197,331
Flat	Neubauer Chamber	Neuron Density	n = 61	125,641
Flat	Flow Cytometry	Neuron Density	n = 61	128,005
Slice	Optical Fractionator	Neuron Density	n = 10	146,008

Table 1. Adult chimpanzee visual cortex total cell and neuron estimates based on three quantification techniques.
Summary table showing the parameter estimates obtained from flattened cortical samples (Flat) and brain slices (Slice).

The current investigation also found that V1 volume of the right hemisphere estimated from images of flattened samples using ImageJ (5.3 cm^3) was within 10% of V1 volume in the left hemisphere estimated from serial sections using the Cavalieri stereological method (4.8 cm^3, Table 1). Thus, the density of cells in flattened samples of V1 ranged from 110,783 to 329,632 cells/mm^3, with an average of 193,867 cells/mm^3 (Figure 2, Table 1). The density of neurons in flattened samples of V1 ranged from 52,936 to 234,039 neurons/mm^3, with an average of 126,823 neurons/mm^3. The density of cells in coronal slices of V1 ranged from 123,263 to 213,806 cells/mm^3, with an average of 197,331 cells/mm^3. The density of neurons in coronal slices of V1 ranged from 108,656 to 162,511 neurons/mm^3, with an average of 146,008 neurons/mm^3. These results appear in Figure 2 and Table 1. Therefore, our investigation revealed that the density of cells and neurons from flattened samples were 98.2% and 86.9% of the stereological estimates, respectively.

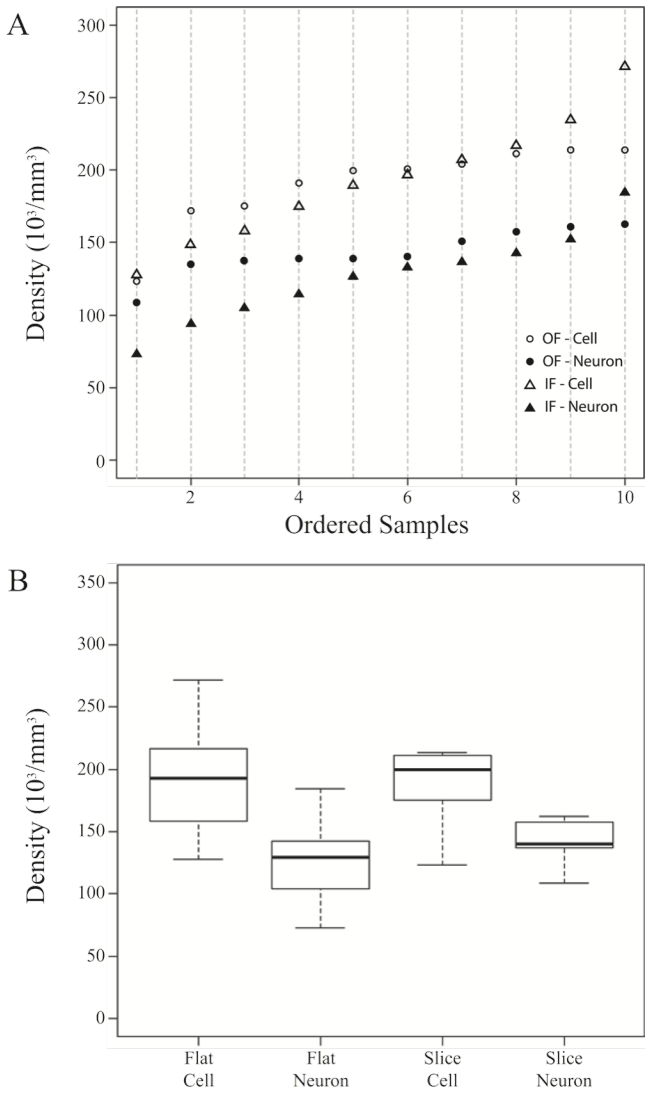

Figure 2. Summary cellular density plots.
Summary plots showing the density (in thousands of cells per mm3) of cells and neurons estimated from flattened cortical samples (Flat) and brain slices (Slice) (A,B). In these plots, the flattened cortical sample estimate is the average of counts using the Neubauer chamber and flow cytometry for each sample. Estimates from flattened cortical samples were ordered and placed into 10 bins of 6 sequential values (the 10th bin contains 7 values, $n = 61$) and are shown for all cells by an open triangle and for neurons by a closed triangle (A). Stereological density estimates from brain slices (Slice) were ordered ($n = 10$) and are shown for all cells by open circles and for neurons by closed circles (A). (B) Is a boxplot depicting the median (thick line), inter-quartile range (box), minimum (lower dotted error bar), and maximum (upper dotted error bar) cellular densities in flattened cortical samples and brain slices.

Corroborating the results of previous studies (Collins et al., 2010; Young et al., 2012), we observed excellent agreement between repeated measurements using the isotropic fractionator (non-parametric T-test, $P = 0.221$, Lin's Concordance = 0.812, $n = 61$) and the flow fractionator (non-parametric T-test, $P = 0.486$, Lin's Concordance = .877, $n = 61$) to estimate the total number of cells. Similarly, we observed low within-sample variance when using the optical fractionator to estimate the

number of neurons (Gundersen coefficient of error (CE) = 0.018 (Gundersen, 1987); 1st CE = 0.028, and 2nd CE = 0.021 (Schmitz & Hof, 2005)) and the total number of cells (Gundersen CE = 0.027 (Gundersen, 1987); 1st CE = 0.023, and 2nd CE = 0.018 (Schmitz & Hof, 2005)), or when using the Cavalieri method to estimate V1 volume (Gundersen CE = 0.012, Gundersen, 1987). In addition, we observed no difference when comparing estimates of the number of neurons (non-parametric T-test, $P = 0.124$, $n = 10$) or the total number of cells (non-parametric T-test, $P = 0.239$, $n = 61$) based on manual counts under the microscope and automated counts using the flow cytometer (Table 1).

Our investigation employed a constant estimate of the cortical depth of V1 (~1.8 mm, n = 42) to determine the volume of samples from flattened cortex because estimates based upon sample weights were more variable, likely as a result of the inclusion of some white matter. As noted, this approach produced a volume estimate of right V1 that was 10% larger (5.3 mm^3) than the (4.8 mm^3) estimate obtained using the Cavalieri method in brain slices from left V1. Despite this difference, our calculations of total cellular density in chimpanzee V1 comparing an average of the isotropic fractionator and the flow fractionator with the optical fractionator were statistically indistinguishable (non-parametric T-test, $P = 0.922$, $n = 10$). In contrast, our calculations of neuronal density using these techniques were statistically distinguishable (non-parametric T-test, $P = 0.027$, $n = 10$, Table 2). The increased estimate of V1 volume from flattened cortex highlights the need for the anatomical specificity available in stained brain slices and may account for the discrepancy between average neuronal density estimates using these techniques (see Discussion).

Table 2. Summary variance statistics table.
Summary table showing the statistical tests performed to assess variation in measurements taken with a single quantification method (Within) and between quantification methods (Between) in tissue processed as flattened cortical samples (Flat) or brain slices (Slice). P-values lower than 0.05 were considered significant. See Materials and Methods for full details of statistical analyses.

Analysis	Tissue	Quantification	Parameter	Test Statistic	P-value	Sample	Figure
Within	Flat	Flow Cytometry	Total Cells	Nonparametric Paired T-test	0.486	n = 61	Fig S1
				Lin's Concordance Statistic	0.877	n = 61	
	Flat	Neubauer Chamber	Total Cells	Nonparametric Paired T-test	0.221	n = 61	Fig S2
	Slice	Stereology	Total Cells	Gundersen CE (m=1)	0.027	n = 324	
			Total Neurons	Gundersen CE (m=1)	0.018	n = 316	
			Volume (Nissl)	Gundersen CE (m=1)	0.017	n = 324	
			Volume (NeuN)	Gundersen CE (m=1)	0.008	n = 316	
Between	Flat vs. Flat	Flow Cytometry vs. Neubauer Chamber	Total Cells	Nonparametric Paired T-test	0.239	n = 61	Fig S3
				Lin's Concordance Statistic	0.892	n = 61	
	Flat vs. Flat	Flow Cytometry vs. Neubauer Chamber	Percent Neuron	Nonparametric Paired T-test	0.124	n = 61	Fig S4
				Lin's Concordance Statistic	0.416	n = 61	
	Slice vs. Flat	Stereology vs. Isotropic Fractionator	Cell Density	Nonparametric Paired T-test	0.922	n = 10	Fig 2
				Lin's Concordance Statistic	0.787	n = 10	
			Neuron Density	Nonparametric Paired T-test	0.027	n = 10	Fig 2
				Lin's Concordance Statistic	0.599	n = 10	

The current work revealed that the distribution of particles along the z-domain of sectioned materials fixed before sectioning while frozen on a sliding microtome and mounted on a glass slide before staining for Nissl-substance was vulnerable to the "lost caps" phenomena (Baryshnikova et al., 2006), and exhibited a linear decrease in cell density with increasing tissue depth (superficial = near coverslip, deep = near glass slide, Figure 3).

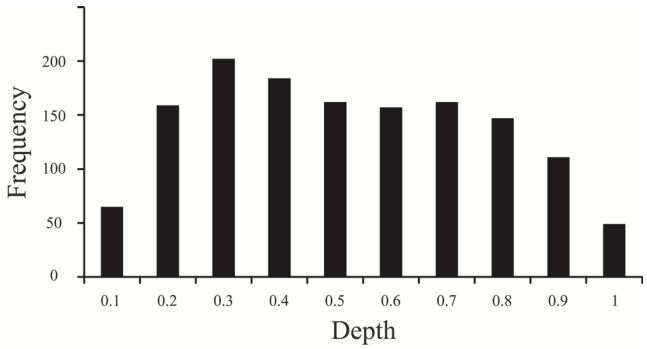

Figure 3. Distribution of particles along the z-axis of Nissl-stained brain slices.
Histogram of data based on 1399 cells (nuclei) from 207 sampling sites throughout V1 illustrating the frequency of cell counts (Y axis) normalized over the depth (X axis) of sections fixed before cutting frozen on a sliding microtome and mounted before staining for Nissl substance. The convention here is that bins to the left (e.g. bin #0.1) are near the coverslip or the exposed edge of tissue during staining (superficial), and bins to the right (e.g. bin #1) are near the glass slide (deep).

Specifically, our measurements indicated that the top and bottom 10% of tissue (bins 0.1 and 1, respectively) each exhibited ~40% of the average z-domain cell count ("lost caps", see Baryshnikova et al., 2006). Including the entire z-axis in the stereological probe would therefore have resulted in an underestimate of the cellular population by ~12.9%. After excluding the top and bottom 10% of tissue, we identified a linear decrease in the density of cell counts as the depth of tissue increased, such that tissue near the slide (deep) contained ~20% fewer counts than (superficial) bins near the coverslip ($F(1,6) = 7.7$, $P = 0.032$, Adjusted $R^2 = 0.48$). The current work, based upon the results of a pilot study indicating the use of 2 µm guard zones, effectively sampled the tissue from 2-12 µm of the average 16.8 µm available, or from the 12^{th} – 71^{st} percentiles along the z-axis. Based on the average counts per bin after excluding the top and bottom 10 percentiles (bin #0.1 [adjacent to the coverslip], and bin #1 [adjacent to the glass slide]), our calculations indicate that this sampling range (12-71%, or bins 2-7) resulted in an estimate of cell number approximately 2.6% above the sample mean.

Discussion

Our estimates of cellular and neuronal populations in the primary visual cortex of a chimpanzee using the isotropic fractionator, the flow fractionator or the optical fractionator agree within 5% (Table 1). This work also contributes data indicating that the measurement of V1 volume from flattened preparations agrees with stereological estimates from brain slices within 10% (Table 1). Our investigation therefore provides evidence of the agreement between estimates of the density of cells and neurons based upon sampling flattened cortex or brain slices (Figure 2).

We provide data on the volume of chimpanzee V1 (4.8 – 5.3 cm^3) consistent with the 4.64 cm^3 (de Sousa et al., 2010) and 5.52 cm^3 (Bush & Allman, 2004) estimates from previous studies. In particular, our stereological estimate of 4.8 cm^3 supports the de Sousa et al. (2010) study that also used the Cavalieri method to estimate the volume of V1 in the left hemisphere of chimpanzees at 4.64 cm^3. The difference between our estimates in the left (4.8 cm^3) and right hemispheres (5.3 cm^3) may reflect inter-hemispheric asymmetry in V1 volume, given that previous work has reported differences in humans of 5% (Murphy, 1985) and 13% (Andrews et al., 1997). This difference in V1 volume may be related to behavioral specializations as has been observed in the primary motor cortex related to hand preference (Hopkins et al., 2010; Sherwood et al., 2007). On the other hand, it is possible that mechanical deformation of the cortical sheet induced during the flattening procedure increased our surface area measurement which, when combined with depth measurements from the intact left hemisphere, produced a slight over-estimate of V1 volume in the right hemisphere. However, given that our estimates were within 10% of each other, and that our calculations fall well within the range suggested by previous studies and exhibit inter-hemispheric asymmetry similar to what has been reported in humans, these results suggest that our measurements provide reasonable estimates of the volume of V1 in the chimpanzee brain.

Results from our investigation of the distribution of particles along the z-axis in sectioned materials stained for Nissl after mounting suggest that the use of guard zones to exclude the top and bottom 10% of tissue avoids underestimating the total number of cells by approximately 13% (effect of "lost caps", Figure 3, see Baryshnikova et al., 2006). However, the implementation of 2 μm guard zones resulted in an effective probe sampling range of the 12-71st percentiles along the z-axis which resulted in a slight overestimation of cell number by approximately 2-3%, based upon the observed decrease in cell density as the observer approaches the glass slide. However, previous work has reported an increase in cell density as the observer moves from the tissue near the coverslip towards the glass slide upon which the tissue was mounted, and the absence an effect of "lost caps," such that cells near sectioned edges were not notably fewer in number than in the middle of the brain slice (Carlo & Stevens, 2011). The inverse effects observed in these two studies are likely explained by the observation that the tissue Carlo & Stevens (2011) measured was processed in a manner identical to that employed in the current investigation, except for two things: (1) Carlo & Stevens (2011) report flipping the tissue such that the edge of the tissue immediately adjacent to but above the knife blade during sectioning was positioned closest to the coverslip in the final stained product, whereas the current study did not flip the tissue in this manner, and (2) Carlo & Stevens (2011) measured brain tissue that underwent perfusion fixation prior to sectioning, while the current investigation measured tissue that underwent a saline flush during perfusion and was subsequently fixed by immersion before sectioning. The opposing gradients of cell loss are therefore likely the result of the same phenomena in both studies such that cells immediately above the microtome blade during sectioning exhibit an increased density, an effect of tissue compression that occurs prior to mounting the tissue (Baryshnikova et al., 2006), and are simply being measured across the tissue in opposing directions. Similarly, the presence of "lost caps" in the current investigation but the absence of this effect in Carlo & Stevens (2011) data is therefore likely the result of whether the brain was fixed by perfusion (resulting in no lost caps), or not (resulting in approximately 60% cell loss at the cut edges). This conclusion is supported by similar observations from different labs that cells are lost at cut edges in immersion fixed (Andersen & Gundersen, 1999; Bahney & von Bartheld, 2014) but not perfusion fixed tissues (Gardella et al., 2003). Thus, these studies together suggest that compression occurs regardless of fixation and is characterized by an effect somewhere between the currently reported 20% (clearance angle = 19˚) and previously reported 50% (clearance angle = 7.5˚, Carlo & Stevens, 2011) decrease in cell density as the observer moves away from the edge of tissue adjacent to and above the knife edge during sectioning. In addition, perfusion fixation appears to mitigate the effect of "lost caps," which results in the loss of a significant number of cells or particles near the surface of sections from immersion-fixed tissues (~60%). Given that the ultimate goal of stereological investigations is to estimate biological parameters of interest in such a way that the original relationships among those parameters are not systematically distorted, our data suggest that the use of guard zones in these tissue preparations are

critical, and that awareness of the extent to which the stereological probe employed samples a known distribution of objects within the available tissue can provide reasonable estimates, for example, of the number of cells and neurons. In summary, our data provide evidence in support of the traditional stereological approach to focus on sampling the "core" of sectioned material, because this avoids the largest source of bias due to the "lost caps" effect at tissue edges (von Bartheld, 2012). In addition, our data provide evidence to suggest that the use of guard zones resulting in an effective sampling range from anywhere within the 10-30th to the 70-90th percentiles produce results within 3-4% of the observed or sample mean.

This study corroborated previous work (Young et al., 2012) comparing the total number of cells in a sample measured using the isotropic fractionator and the flow fractionator (Figures 4-6). We found that the total number of cells estimated from flattened cortical samples was 5% greater than the stereological estimate (Table 1). However, our stereological investigation likely overestimated the actual number of cells in our sample by approximately 3%, resulting in a discrepancy between hemispheres of approximately 8%. Given that previous investigations of human V1, as well as the current volumetric analysis, indicate inter-hemispheric differences on the order of 5-13% (Murphy, 1985; Andrews et al., 1997), these data suggest that the observed differences in cell number reflect biological asymmetry between the hemispheres. The close agreement between these results and previous studies therefore strongly suggests that each of these distinct techniques estimate a similar parameter, the total number of cells in chimpanzee V1.

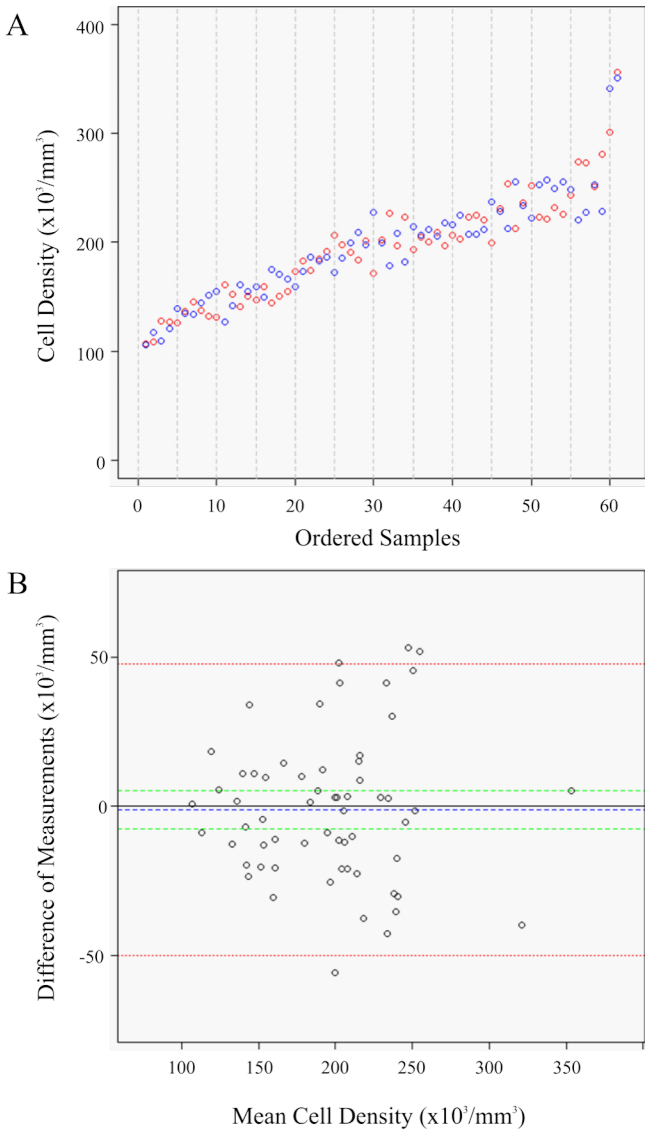

Figure 4. Analysis of flow cytometry estimates.
Repeated measures graph depicting the agreement between the first (red) and second (blue) density measurements on ordered samples (A). The vertical dotted lines indicate every 5th sample (A). Bland-Altman plot showing the agreement between the first and second measurement taken from each sample by comparing the difference between repeated measurements on the Y axis against the mean of each sample estimate plotted along the X axis (B). The blue dotted line indicates the sample mean, the green dotted lines indicate the 95% interval, and the red dotted line indicates a single standard deviation from the mean (B). All density estimates are in thousands of nuclei per mm^3 (A, B).

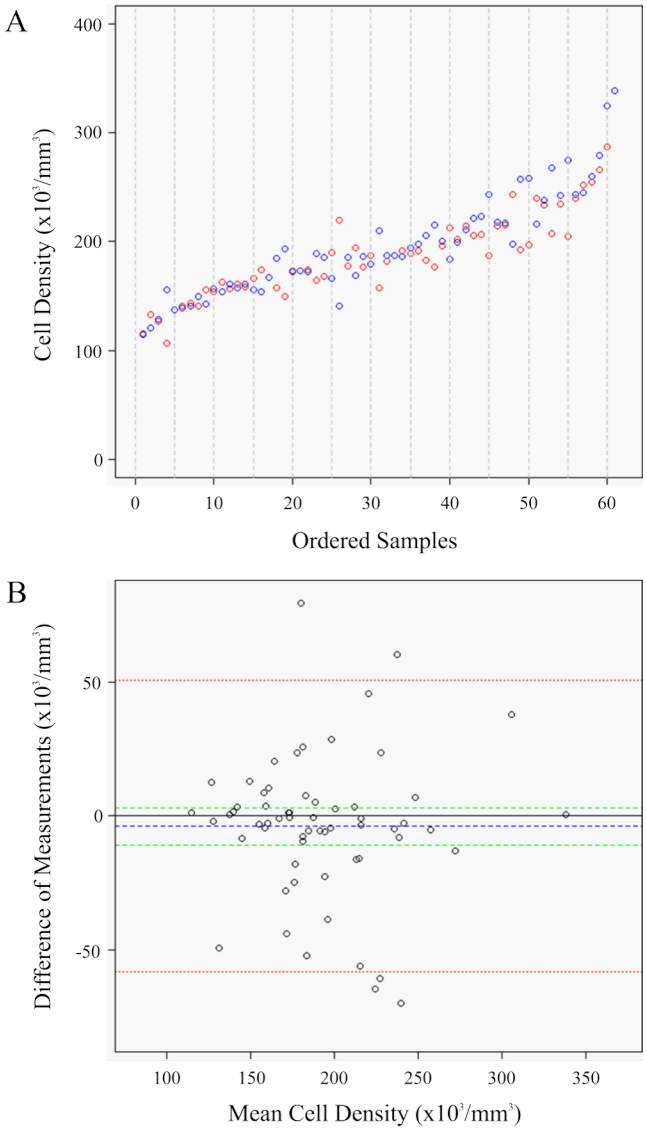

Figure 5. Analysis of manual counts using the Neubauer chamber.
Repeated measures graph depicting the agreement between the first (red) and second (blue) density measurements on ordered samples (A). The vertical dotted lines indicate every 5th sample (A). Bland-Altman plot showing the agreement between the first and second measurement taken from each sample by comparing the difference between repeated measurements on the Y axis against the mean of each sample estimate plotted along the X axis (B). The blue dotted line indicates the sample mean, the green dotted lines indicate the 95% interval, and the red dotted line indicates a single standard deviation from the mean (B). All density estimates are in thousands of nuclei per mm^3 (A, B).

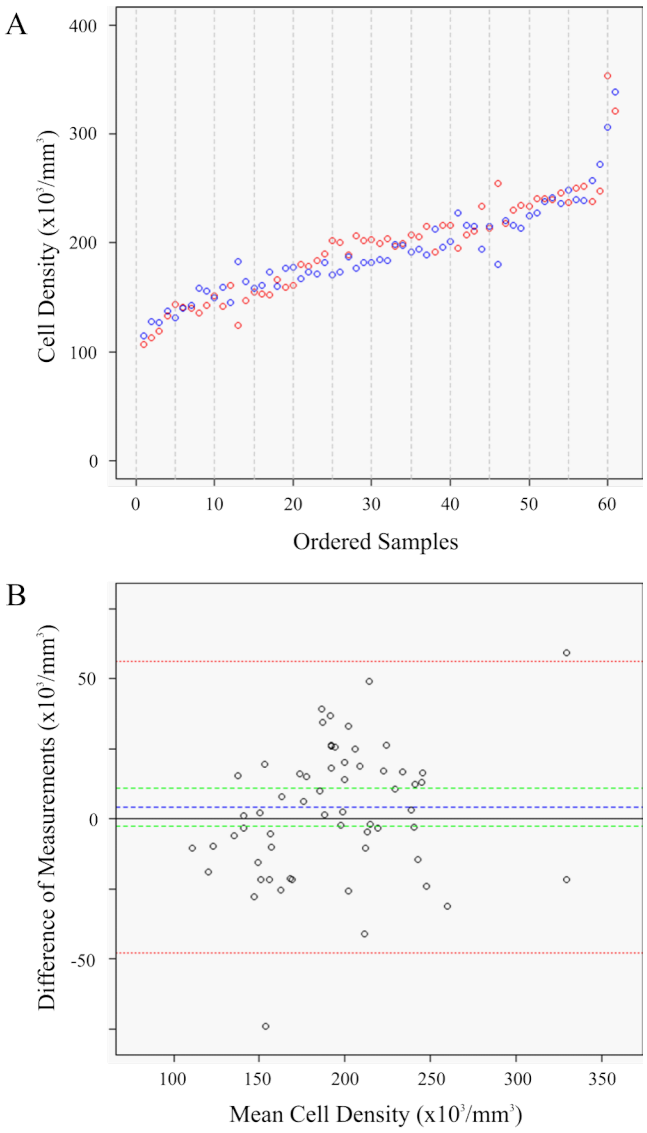

Figure 6. Analysis of flattened cortical sample estimates.
Repeated measures graph depicting the agreement between the average density count using the Neubauer chamber (red) and the flow cytometer (blue) on ordered samples (A). The vertical dotted lines indicate every 5th sample (A). Bland-Altman plot showing the agreement between these quantification procedures by comparing the difference between estimates on the Y axis against the mean of each sample estimate plotted along the X axis (B). The blue dotted line indicates the sample mean, the green dotted lines indicate the 95% interval, and the red dotted line indicates a single standard deviation from the mean (B). All density estimates are in thousands of nuclei per mm^3 (A, B).

This work provides evidence in agreement with previous studies investigating the percentage of neuronal cells in samples measured using the isotropic fractionator and the flow fractionator (Collins et al., 2010; or Figure 7).

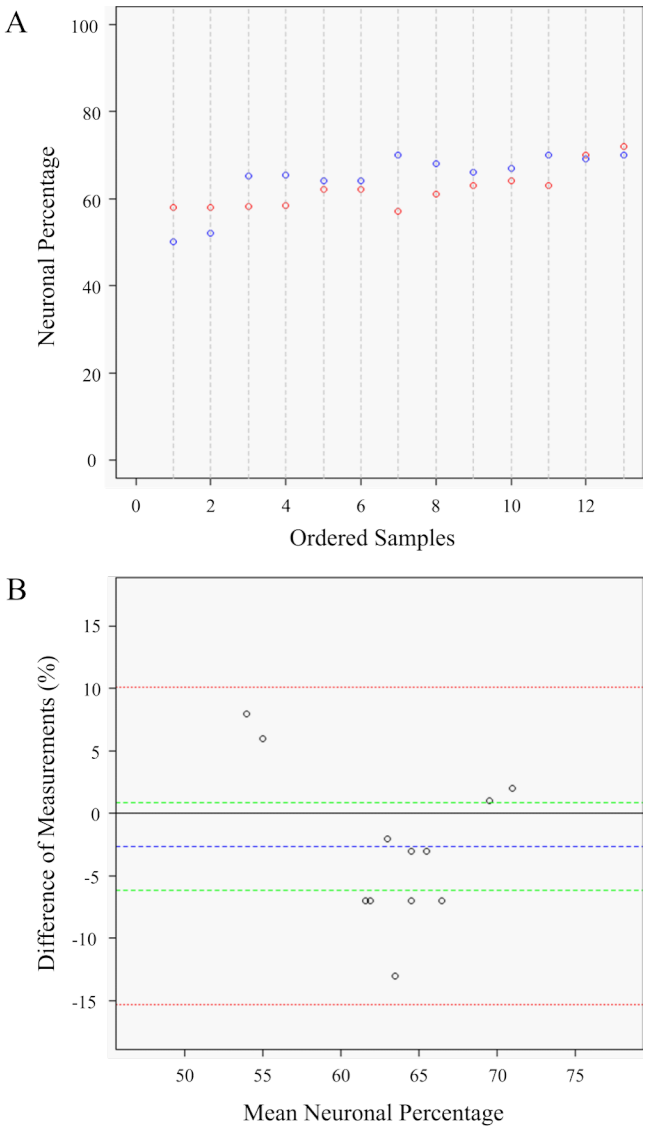

Figure 7. Analysis of neuronal percentage.
Repeated measures graph depicting the agreement between the average neuronal percentage using the Neubauer chamber (red) and the flow cytometer (blue) on ordered samples (A). The vertical dotted lines indicate individual samples (A). Bland-Altman plot showing the agreement between these quantification procedures by comparing the difference between estimates on the Y axis against the mean of each sample estimate plotted along the X axis (B). The blue dotted line indicates the sample mean, the green dotted lines indicate the 95% interval, and the red dotted line indicates a single standard deviation from the mean (B). All density estimates are in thousands of nuclei per mm^3 (A, B).

It should be noted that the estimate of the absolute number of neurons in tissue samples from flattened cortex is a derivative of the estimate of the total number of cells using DAPI. This contrasts with the stereological estimate of neuron number, which is based upon an independent run of the optical fractionator in a series of sections stained for NeuN, adjacent to the Nissl-stained series. The percentage of neuronal cells based upon our stereological investigation is calculated as the number of cells in NeuN-stained sections divided by the number of cells in Nissl-stained sections. Therefore, our comparison of the

number of neurons using these techniques is two-fold: (a) we compared the percentage of all the neuronal cells, and (b) we compared the absolute number of neurons estimated. We found that the mean percentage of neuronal cells in chimpanzee V1 estimated from flattened cortical samples was 65.4%, while the mean percentage of neuronal cells estimated using stereology was 72.4%. Given that our stereological analysis likely produced a ~3% overestimate of cell number, the percentage of neuronal cells estimated from brain slices may be approximately ~74%. This difference in the percentage of neuronal cells is likely due to the inclusion of a minimal amount of white matter in the flattened cortical sample preparation. Next, we calculated the absolute number of neurons and discovered that the estimate from flattened cortical samples (658 million) was 5% lower than the stereological estimate of 695 million (Table 1). Given that previous evidence indicates a >5% rightward bias in V1 size and cell number, the observation that right V1 contains 5% fewer neurons suggests that neurons may be lost during implementation of the isotropic fractionator method (Clarke & Oppenheim, 1995). Although future research may further clarify this issue, the reasonably close (~10%) agreement between these estimates suggest that our quantification procedures approximate the same parameter, the total number of neurons in chimpanzee V1.

Our data provide evidence that there are approximately 195,000 (193,867 – 197,331) cells per mm^3 of chimpanzee V1, out of which around 136,000 (126,823 – 146,008) are neurons. These data differ somewhat from the results of a previous study of cellular density in chimpanzee V1 which reported ~330,000 cells per mm^3, out of which 208,930 were neurons (Lewitus et al., 2012). Interestingly, both of these results place the density of neurons in chimpanzee V1 in range of the upper 60 percentiles. However, the discrepancy between the absolute density of neuronal and non-neuronal cells in these studies is likely due to a combination of factors including tissue preparation, the type of fixation and the histological staining protocol employed. For instance, Lewitus et al. (2012) excluded layer 1 from their estimates as a result of variable tissue quality, and measured cortical thickness only twice for each section investigated, the combination of which may have contributed to the higher cellular densities they observed. However, our results are in agreement with this and other published studies indicating a high density of neurons in primary visual cortex, particularly in primates (Campi et al., 2011; Collins et al., 2010; 2013; Lewitus et al., 2012).

The density of cells and neurons based on flattened samples were 98.2% and 86.9% of the stereological estimates, respectively. However, the observation that our stereological data probably overestimated (~3%) the total number of cells may account for the observed ~2% difference in cell density between hemispheres. These results demonstrate that the density of cells can be determined with high precision, whether measured using traditional stereological tools or with more recently developed techniques such as the isotropic fractionator and flow fractionator. In our hands, these distinct methodologies produced estimates of the density of neurons that agreed within 15%. The source of this discrepancy may involve the inclusion of a minimal amount of white matter in flattened cortical samples during dissection, the slight overestimation of regional volume because of deformations in the cortical sheet induced during the flattening procedure, the loss of neuronal cells, or some combination of these. Despite these relatively small differences, our ability to replicate the composition and density of cellular populations in the chimpanzee primary visual cortex provides evidence supporting our ability to compare results from distinct methodologies in determining the distribution of different types of cells in the brain.

Conclusions

Our research indicates the reproducibility of estimates of the cellular composition of brain tissue using distinct tissue processing and quantification methodologies when the accurate identification of a single cortical region of interest is possible. Our results thus demonstrate the validity of using the isotropic fractionator, flow fractionator or optical fractionator to obtain cell and neuron counts. Ultimately, these results facilitate a more comprehensive understanding of neurobiological circuitry by presenting investigators with evidence that these techniques estimate the same parameters of interest, allowing the investigator an additional line of evidence to aid in the interpretation of experimental results.

Our results are also significant because they indicate that V1 in chimpanzees, our closest living genetic relatives, conforms to the general finding in primates that V1 contains more densely packed neurons than other cortical areas (Carlo & Stevens, 2013; Collins et al., 2013; Rockel et al., 1980; Young et al., 2013). This means that, beyond the observation that layer 4 contains small neurons, each of the cortical layers in V1 contains neurons that are on average smaller than in other cortical areas. Smaller neurons tend to have fewer synaptic inputs (Elston et al., 2005; Jacobs et al., 2001) and are thus thought to be less likely to dramatically transform incoming sensory signals. Primate brains are known to contain a large proportion of neocortical tissue devoted to visual perception. Furthermore, compared to other mammals, V1 in primates has the specialized task of distributing sensory input to cortical regions throughout the visual system that are integral for visual percepts. Accordingly, our findings are consistent with the observation that primate V1 is characterized by small, densely packed neurons, which may have facilitated the evolution of primate V1 into a region particularly effective at providing multiple downstream cortical regions with the relatively raw sensory input necessary for higher-order functional operations.

Interpretation

In the analysis of neuroanatomical data, the diligent investigator must decide early on what hypotheses are of interest, as the methods required to obtain the appropriate data may only be available through alternative procedures. For example, where studies seek to understand the relationship between gross subdivisions of the brain and computational indices of discrete anatomical objects, destructive methods that have the benefit of being cheap, fast and reliable may be optimal. However, in studies where morphological characteristics are of primary interest, the slower, more time consuming methods of slice-based histology may be of greatest utility. On the other hand, novel methods are continually being developed and its possible that an optimal solution exists in the literature, even if not well-known or deployed by many laboratories. Alternatively, its possible the investigator is trying to make use of existing materials, for which the decision about tissue preparation has been made. Although some recent work has shown promise to integrate faster, destructive methods with the slower preparation methods deployed in most of the worlds neuroanatomical collections (Gabi et al., 2016), these methods still require a high degree of skilled labor engaged in time-consuming activities. The remaining frontier for the quantitative analysis of neuroanatomical data thus falls largely in the realm of deploying increasingly efficient computational strategies to garner insight from limited biological specimens, although it appears as has been recently noted by a variety of investigators that an optimal solution likely requires the complementary blend of human expertise and computational power (Inglis et al., 2008).

Acknowledgments

The majority of this chapter has been published previously in Miller et al., 2014.

References

Andersen BB, Gundersen HJ. (1999). Pronounced loss of cell nuclei and anisotropic deformation of thick sections. J Microsc. 196(Pt 1):69-73.

Andrews TJ, Halpern SD, Purves D. (1997). Correlated size variations in human visual cortex, lateral geniculate nucleus, and optic tract. J Neurosci. 17(8):2859-68.

Bahney J, von Bartheld C. (2014). Validation of the isotropic fractionator: comparison with unbiased stereology and DNA extraction for quantification of glial cells. J Neurosci Methods. 222:165-74.

Balaram P, Hackett TA, Kaas JH. (2013). Differential expression of vesicular glutamate transporters 1 and 2 may identify distinct modes of glutamatergic transmission in the macaque visual system. J Chem Neuroanat. 50:21-38.

Baryshnikova LM, Von Bohlen Und Halbach O, Kaplan S, Von Bartheld CS. (2006) Two distinct events, section compression and loss of particles ("lost caps"), contribute to z-axis distortion and bias in optical dissector counting. Microsc Res Tech. 69(9):783-56.

Bland JM, Altman DG. (1986). Statistical methods for assessing agreement between two methods of clinical measurement. Lancet. 1(8476):307-10.

Brodmann K. (1909). Vergleichende Lokalisationslehre der Groβhirnrinde in ihren Prinzipien dargestellt auf Grund des Zellenbaues. Leipzig: Barth-Verlag.

Bush EC, Allman JM. (2004). Three-dimensional structure and evolution of primate primary visual cortex. Anat Rec A Discov Mol Cell Evol Biol. 281(1):1088-94.

Campi KL, Collins CE, Todd WD, Kaas JH, Krubitzer L. (2011). Comparison of area 17 cellular composition in laboratory and wild-caught rats including diurnal and nocturnal species. Brain Behav Evol. 77(2):116-30.

Carlo CN, Stevens CF. (2013). Structural uniformity of neocortex, revisited. Proc Natl Acad Sci USA. 110(4):1488-93.

Catania KC, Northcutt GR, Kaas JH, Beck PD. (1993). Nose stars and brain stripes. Nature. 364: 493.

Clarke PG, Oppenheim RW. (1995). Neuron death in vertebrate development: in vitro methods. Methods Cell Biol. 46:277-321.

Collins CE, Leitch DB, Wong P, Kaas JH, Herculano-Houzel S. (2013). Faster scaling of visual neurons in cortical areas relative to subcortical structures in non-human primate brains. Brain Struct Funct. 218(3):805-16.

Collins CE, Young NA, Flaherty DK, Airey DC, Kaas JH. (2010). A rapid and reliable method of counting neurons and other cells in brain tissue: a comparison of flow cytometry and manual counting methods. Front Neuroanat. 4:5.

De Sousa AA, Sherwood CC, Mohlberg H, Amunts K, Schleicher A, MacLeod CE, Hof PR, Frahm H, Zilles K. (2010). Hominoid visual brain structure volumes and the position of the lunate sulcus. J Hum Evol. 58(4):281-92.

Elston GN, Oga T, Fujita I. (2005). Regional specialization in pyramidal cell structure in the visual cortex of the Galago: an intracellular injection study of striate and extrastriate areas with comparative notes on New World and Old World monkeys. Brain Behav Evol. 66(1):10-21.

Gardella, D, Hatton WJ, Rind HB, Rosen GD, von Bartheld CS. (2003). Differential tissue shrinkage and compression in the z-axis: implications for optical dissector counting in vibratome-, plastic- and cryosections. J Neurosci Methods. 124(1):45-59.

Glaser JR, Glaser EM. (2000). Stereology, morphometry and mapping: the whole is greater than the sum of its parts. J Chem Neuroanat. 20(1):115-26.

Gundersen HJ, Jensen EB. (1987). The efficiency of systematic sampling in stereology and its prediction. J Microsc. 147(3):229-63.

Hässler RG. (1967). Comparative anatomy of the central visual system in day- and night-active primates. In: Hässler R, Stephen S, editors. Thieme, Stuttgart: Evolution of the forebrain. Springer. p. 419-434.

Herculano-Houzel S, Lent R. (2005). Isotropic fractionator: a simple, rapid method for the quantification of total cell and neuron numbers in the brain. J Neurosci. 25(10):2518-21.

Hopkins WD, Taglialatela JP, Russell, JL, Nir TM, Schaeffer J. (2010). Cortical representation of lateralized grasping in chimpanzees (*Pan troglodytes*): a combined MRI and PET study. PLoS One. 5(10):e13383.

Jacobs B, Schall M, Prather M, Kapler E, Driscoll L, Baca S, Jacobs J, Ford K, Wainwright M, Treml M. (2001). Regional dendritic and spine variation in human cerebral cortex: a quantitative golgi study. Cereb Cortex. 11(6):558-71.

Jerison HJ. (1955). Brain to body ratios and the evolution of intelligence. Science. 121: 447-449.

Krubitzer LA, Manger P, Pettigrew J, Calford M. (1995). Organization of somatosensory cortex in monotremes: in search of the prototypical plan. J Comp Neurol. 351(2):261-306.

Lewitus E, Hof PR, Sherwood CC. (2012). Phylogenetic comparison of neuron and glia densities in the primary visual cortex and hippocampus of carnivores and primates. Evolution. 66(8):2551-63.

Lin LI. (1989). A Concordance correlation coefficient to evaluate reproducibility. Biometrics. 45(1):255-68.

Miller DJ, Duka T, Stimpson CD, Schapiro SJ, Baze WB, McArthur MJ, Fobbs AJ, Sousa AM, Sestan N, Wildman DE, Lipovich L, Kuzawa CW, Hof PR, Sherwood CC. (2012). Prolonged myelination in human neocortical evolution. Proc Natl Acad Sci USA. 109(41):16480-5.

Miller DJ, Lackey EP, Hackett TA, Kaas JH. (2013). Development of myelination and cholinergic innervation in the central auditory system of a prosimian primate (*Otolemur garnetti*). J Comp Neurol. 521(16):3804-16.

Miller DJ, Balaram P, Young NA, Kaas JH. (2014). Three counting methods agree on cell and neuron number in chimpanzee primary visual cortex. Frontiers in Neuroanatomy, 8.

Mullen RJ, Buck, CR, Smith AM. (1992). NeuN, a neuronal specific nuclear protein in vertebrates. Development. 116(1):201-11.

Murphy GM Jr. (1985). Volumetric asymmetry in the human striate cortex. Exp Neurol. 88(2):288-302.

Nurnberger, J.I., Gordon, M.W. (1957). The cell density of neural tissues: direct counting method and possible applications as a biologic referent. Prog Neurobiol. 2:100-138.

Raghanti MA, Stimpson CD, Marcinkiewicz JL, Erwin JM, Hof PR, Sherwood CC. (2008). Cholinergic innervation of the frontal cortex: differences among humans, chimpanzees, and macaque monkeys. J Neurosci. 155(1):203-20.

Rockel AJ, Hiorns RW, Powell TP. (1980). The basic uniformity in structure of neocortex. Brain. 103(2):221-44.

Schmitz C, Hof PR. (2005). Design-based stereology in neuroscience. J Neurosci. 130(4):813-31.

Sherwood CC, Raghanti MA, Stimpson CD, Bonar CJ, de Sousa AA, Preuss TM, Hof PR. (2007). Scaling of inhibitory interneurons in areas V1 and V2 of anthropoid primates as revealed by calcium-binding protein immunohistochemistry. Brain Behav Evol. 69(3):176-95.

Sherwood CC, Wahl E, Erwin JM, Hof PR, Hopkins WD. (2007). Histological asymmetries of primary motor cortex predict handedness in chimpanzees (*Pan troglodytes*). J Comp Neurol. 503(4):525-37.

Sur M, Merzenich MM, Kaas JH. (1980). Magnification, Receptive-Field area, and "hypercolumn" size in areas 3b and 1 of somatosensory cortex in owl monkeys. J Neurophysiol. 44(2):295-311.

Takahata T, Higo N, Kaas JH, Yamamori T. (2009). Expression of immediate-early genes reveals functional compartments within ocular dominance columns after brief monocular inactivation. Proc Natl Acad Sci USA. 106(29):12151-5.

von Bartheld CS. (2002). Counting particles in tissue sections: choices of methods and importance of calibration to minimize biases. Histol Histopathol. 17(2):639-48.

von Bartheld CS. (2012). Distribution of particles in the z-axis of tissue sections: relevance for counting methods. Neuroquantology. 10(1):66-75.

Young NA, Collins CE, Kaas JH. (2013). Cell and neuron densities in the primary motor cortex of primates. Front Neural Circuits. 7:30.

Young NA, Flaherty DK, Airey DC, Varlan P, Aworunse F, Kaas JH, Collins CE. (2012). Use of flow cytometry for high-throughput cell population estimates in brain tissue. Front Neuroanat. 6:27.

Zamenhof S. (1976). Final number of Purkinje and other large cells in the chick cerebellum influenced by incubation temperatures during their proliferation. Brain Res. 109(2):392-4.

CHAPTER 3

EVOLUTION OF MICROSTRUCTURE IN THE PRIMATE PRIMARY VISUAL CORTEX

Introduction

The primary visual field of the cerebral cortex (V1; also known as Brodmann's area 17) was one of the first described regions of the brain (Brodmann, 1909; Hassler, 1967), and previous work has described the location, connections, subdivisions, and size of V1 in a variety of mammals (Casagrande & Kaas, 1994), including physiological work in primates demonstrating its integral role in nearly all visual perceptual processes as lesions to this area may result in the phenomenon of cortical blindness or blindsight (Cowey & Stoerig, 1989; Stoerig & Cowey, 2007). In addition, research has shown that in primates, V1 receives the vast majority of information routed through the lateral geniculate nucleus of the thalamus (LGN) from the retina, and that the primary terminal ramification of LGN neurons is to the lower tier of granule cells or layer 4 (Hassler, 1967; reviewed in Casagrande & Kaas, 1994; Casagrande & Ichida, 2011). Indeed, despite extensive knowledge of the physiology, connectivity, and cellular composition of V1 and the granular cell layer 4 in specific animal models (Hubel & Weisel, 1959; Sun et al., 2016; Lund, 1988), we lack basic quantitative data on the variation of this circuitry across primates. One of the characteristic features of the primate visual system is the projection from V1 to the middle temporal (MT) visual area (Allman & Kaas, 1972; Casagrande & Kaas, 1994), which is involved in the perception of motion. Indeed, across primates, area MT receives input from the layer of larger pyramidal neurons lying between the upper and lower tiers of granular cells that form the basis of the confusion between major schema of V1 laminar organization (Casagrande & Kaas, 1994). According to Brodmann (1909), V1 contains six layers, and based solely upon cytoarchitectonic criteria and the depth across the cortical mantle at which these layers appeared, he suggested the presence of four subdivisions of the granular layer (4A, 4B, 4C alpha, 4C beta). The aforementioned upper granular layer was designated 4A, the layer of larger pyramidal cells was 4B, and the lower tier of granule cells was designated as subdivisions of 4C. Subsequent analysis of nocturnal and diurnal primates however, led Hassler (1967) to revise Brodmann's schema, putting Brodmann's 4A and 4B into Hassler's layer 3, and to then rename Brodmann's layers 4C alpha and beta as 4A and 4B, respectively (Hassler, 1967; reviewed in Casagrande & Kaas, 1994). Thus, area MT receives input from Brodmann's 4B or part of Hassler's layer 3 – the layer of larger pyramidal neurons between the granular layers. The advent of anatomical tracers provided a novel source of evidence to help resolve the controversy, despite the continued use of Brodmann's schema, by demonstrating support for Hassler's schema by the shared connectivity profile across a range of primates of this intervening layer of pyramidal neurons (Hassler 3C) that project to area MT and support the perception of motion (Casagrande & Kaas, 1994). Layer 3C projection neurons receive input from the lower tier of granule cells, actually the top half of this tier or Hassler's layer 4A, which are targeted by the magnocellular (M) neurons of the LGN (reviewed by Casagrande & Ichida, 2011). The M neurons of the LGN receive input from a variety of retinal cells and exhibit extensive physiological overlap with P neurons of the LGN, not only suggesting that each morphological class of cells in the LGN actually consists of multiple classes, but indicating that discrete neurobiological functions arise downstream (Casagrande & Ichida, 2011; Sherman & Guillery, 2005). Further complicating the issue, M cells of the LGN project to cortical neurons in the middle of Hassler's layer 4, as do the P cells of the LGN, which also project to the very bottom portion of the lower tier of granule cells in V1 (Hassler's 4B). Thus, given the extensive physiological overlap between M and P cells in the LGN, the lower tier of granule cells in V1 (Hassler's layer 4) is the primary geniculorecipient cortical layer in V1 and acts as a waystation for nearly all the information coming from the retina through the LGN.

The cellular composition of neurobiological circuits represents an important, albeit incomplete, index of the anatomical constraints through which physiological information flows. For example, cells of

the thalamus (e.g. M, P, K) are often characterized based upon morphology, and yet the physiological profile of different cell classes may exhibit extensive overlap, or cells within the same morphological class may receive input from distinct sources (Sherman & Guillery, 2005). Regardless, previous work has shown that the distribution of cell subtypes in gross anatomical structures of the brain follow general scaling rules (Herculano-Houzel et al., 2015), and that variation in scaling parameters may occur within discrete regions or even across closely related taxa exhibiting distinct foraging behaviors (Campi et al., 2010). Additional work has shown that the relationship between different classes of cells, for example the glia to neuron ratio, may reveal important information about the metabolic needs and projection patterns of neurobiological circuits (Mota & Herculano-Houzel, 2014). These observations suggest anatomical indices may reveal important aspects of nervous system circuitry to aid in the interpretation of the relationship between brain structure and function. However, detailed information on the cellular composition of discrete pathways with well-defined physiological roles are often unavailable. Together, these observations indicate important gaps exist in our understanding of the anatomical indices associated with important functional pathways within the primate nervous system. Thus, this project seeks to gain a better understanding of the visual system by gathering basic quantitative data on the volume, relative size, and cellular composition of important subdivisions of the visual system in the primate cerebral cortex.

Materials & Methods

Sample

All procedures involving animals and animal tissues followed the NIH Guidelines for the Use of Laboratory Animals, and were approved in advance by the Vanderbilt University Institutional Animal Care and Use Committee when not received from outside institutions. The study sample consisted of tissue from the primary visual cortex of non-neuropathological adults in the following species: human (*Homo sapiens*, n = 1), chimpanzee (*Pan troglodytes*, n = 1), baboon (*Papio Anubis*, n = 1), macaque (*Macaca mulatta*, n =1; *Macaca nemestrina*, n =1; *Macaca fascicularis*, n = 1), squirrel monkey (*Saimiri sciureus*, n = 3), owl monkey (*Aotus trivirgatus*, n = 3), marmoset (*Callithrix jacchus*, n = 2), tamarin (*Saguinus oedipus*, n = 1) and galago (*Otolemur garnetti*, n = 5). The human specimen was obtained from an 82 year old female through the Anatomical Request Program at the University of Tennessee Memphis Health Sciences Center (Memphis, TN, USA). The baboon and chimpanzee specimens were purchased from the Texas Biomedical Research Institute's Southwest National Primate Research Center (San Antonio, TX, USA). Other specimens were obtained in the context of unrelated, ongoing experiments at Vanderbilt University. The human specimen was extracted from the skull postmortem and postfixed for 2 weeks in 10% formalin prior to being shipped overnight to Vanderbilt University (Nashville, TN, USA). The chimpanzee specimen was collected after post-mortem flushing with 0.1% phosphate buffered saline (PBS; 0.1 molar, pH 7.4; Sigma-Aldrich, Saint Louis, MO, USA), and then shipped overnight in PBS. Other specimens were injected with a lethal dose of sodium pentobarbital (60 mg/kg or more; Sigma-Aldrich, Saint Louis, MO, USA) and perfused intracardially, first with PBS, and then in quick succession by 4% paraformaldehyde (PFA, Sigma-Aldrich, Saint Louis, MO, USA) in PBS, and finally 4% PFA in PBS with 10% sucrose. Upon arrival or following perfusion, the cerebral cortex was separated from the subcortical structures, bisected and then cleaned of vasculature and pia. Samples were then blocked and immersed in 30% sucrose and PBS between 24 and 72 hours prior to sectioning at between 30 and 50 µm on a sledge microtome (American Optical, model #860, clearance angle = 19˚) while the tissue was held below 0 degrees Celsius. Upon sectioning, brain slices are grouped into series (often, 1 in 10 series are used for large brains such as the human, chimpanzee, and baboon, and 1 in 6 series are often used for smaller specimens; however this varies according to the needs of the primary research project for which the sample was obtained and some of the smaller brain specimens were also 1 in 10) for use in a battery

of histological visualization procedures. Only specimens where the entire extent of the primary visual field of the cerebral cortex (V1) was available for study were included in this project.

Histology and Identification of Anatomical Regions and Objects

All specimens included in this research project had, at a mimimum, a single series of sections stained with thionin for Nissl substance, and upon which the majority of stereological counts were collected. Neighboring section series stained for cytochrome oxidase (CO), acetylcholinesterase (ACHE), an antibody for neuronal nuclei (NeuN; AB667 from Millipore, Billerica, MA, USA), an antibody for parvalbumin (PV; Sigma-Aldrich P3088, Saint Louis, MO, USA), and an antibody for vesicular glutamate transporter 2 (VGLUT2; Millipore, Billeca, MA, USA), were not always available across the sample but were used when available to perform counts or help identify the location of the primary visual cortical field as well as, according to Hassler (1967), the primary geniculo-recipient granular cell layer 4 (Balaram et al., 2013; 2014; Balaram & Kaas, 2014; Mullen et al., 1992; Wong-Riley, 1979). For details of histological and immunohistochemical procedures, see Balaram et al., 2013; 2014.
The use of multiple stains and previously published descriptions facilitated the identification of V1 and Layer 4 in each primate brain (Casagrande & Kaas, 1994; Hassler, 1967; Lund, 1988; Wong & Kaas, 2010). We defined the primary visual cortex by its highly laminated structure (this region is also known as 'striate' cortex), in which the outer line of Baillarger or the Stripe of Gennari is evident even prior to histological processing (Brodmann, 1909; also see Nieuwenhuys, 2013), and which can furthermore be identified by the characteristic staining visible in preparations for a variety of markers, such as the dense staining of CO, ACHE, PV and VGLUT2 in the middle of the cortical mantle or sheet (Balaram & Kaas, 2014). We defined the cortical mantle as the tissue between the pia mater on the surface of the brain, and the transition into white matter towards the deep portions of the brain, often visible as anatomies visible with different histological procedures either disappeared or staining patterns ceased to change with increasing depth (or as in Nissl, neurons were no longer visible but replaced by glial cells). We defined the granular cell layer by the high density of small, round neurons receiving input from the lateral geniculate nucleus (LGN) visible in preparations for both Nissl and NeuN. Although not selective for geniculostriate projections, staining for VGLUT2 and PV facilitated the identification of the granular cell layer which is heavily innervated by the LGN in primates (Aihara et al., 2000; Balaram et al., 2013; Garcia-Marin et al., 2012; Hendrickson et al., 1991; Wong & Kaas, 2010). Similarly, sections stained for CO and ACHE facilitated the identification and location of the granular cell layer 4 in V1, although these stains reveal more diffuse synaptic input (Wong-Riley, 1979; Balaram & Kaas, 2014) than the original cellular morphological or cytoarchitectural definition of the granular cell layer (Brodmann, 1909; Casagrande & Kaas, 1994; Hassler, 1967).

Thionin was used following Nissl's staining method to visualize ribosomes within the cell body to reveal the cellular morphology used to distinguish neurons from glia, and which constitutes the basis for the majority of counting performed in this project. Immunolabelling with an antigen to NeuN selectively reveals the presence of neurons (Mullen et al., 1992; Wolf et al., 1996), and was also used in the determination of neuron number in this project. Cell types were distinguished by pre-defined morphological features or by their visualization using immunohistochemistry (Garcia-Cabezas et al., 2016; Giannaris & Rosene, 2012; Pelvig et al., 2008). In Nissl stained materials, we only distinguished neurons from glia; glial cell subtypes (i.e. oligodendrocytes and astrocytes; microglia or pericytes and endothelial cells were not included) were not tabulated independently but compared as a group to neuron number. Neurons were distinguished from glia based upon their size, opacity, and the presence of nucleoli. As recently reviewed by Garcia-Cabezas et al. (2016), neurons were distinguished by the presence of darkly stained nucleoli within a more moderately stained nucleus within the more pale-staining perikaryon or cytoplasm-filled cell soma, and which was often, but not always, noticeably larger than other objects within the field of view.

Stereological measurement of regional volume and cell number

All measurements and images were collected using a computerized stereology system that consisted of a Nikon E80i microscope outfitted with ×2 to ×100 oil immersion (NA = 1.3) objective lenses, and connected to a motorized stage (Ludl Instruments) running the commercially available StereoInvestigator software (MBF Bioscience, Williston, VT) on a Dell desktop with 8 GB RAM and 1TB storage. Contours were drawn under ×2 objective lens magnification, and images were acquired or counts were made with 100× oil immersion objective lens magnification under Köhler illumination. A mean of 311 probes, with a standard error of the mean (SEM) of 39, were investigated per specimen included in this report. We used the Cavalieri estimator and optical fractionator workflows available with StereoInvestigator to measure the volume of anatomical regions and the number of neurons and glia in our samples, respectively. DJM performed initial pilot tests in each species included in this project to establish the appropriate stereological sampling parameters to maintain a low coefficient of error (Gundersen (m=1) CE < 0.05) (Schmitz & Hof, 2005): number of sections to be investigated (n = 9-12, mode = 10), probe area (from 15 μm^2 to 30 μm^2, mode = 15 μm^2), probe height (6-10 µm, mode = 6 µm), guard zone (3 µm), frame step (V1: 500 μm^2 to 2000 μm^2, Layer 4: 200 μm^2 to 350 μm^2) and frequency of thickness measurements (1 in 8). DJM conducted all the regional volumetric analyses using the Cavalieri method (200 μm^2 in the smallest and up to 1000 μm^2 in the largest brains and regions under investigation) in sections stained for Nissl and NeuN. DJM performed the first counts using the optical fractionator in each species in this study before using the systematic random sampling image stack acquisition workflow to archive stereological images for subsequent analysis by additional investigators (as well as for DJM's confirmatory analyses) through our custom crowdsourcing website built with support from the Vanderbilt Institute for Digital Learning.

Objects were marked as neurons or glia either according to evidence of cellular morphology as discussed above, or by immunolabeling. We used the top of the cell soma as the unique identifying feature of each object to avoid the double-counting problem. Lines of inclusion and exclusion defined the probe dimensions within the X and Y domain, and the bottom section was excluded as the third dimensional (Z domain) line of exclusion. We replicated these stereological parameters on our custom crowdsourcing website, with the addendum that markers were placed in the first image where the top of the cell soma came into focus within the dimensions of the probe. The total number of cells was then determined by multiplying the number of counts by the reciprocals of the area section fraction, serial section fraction, and the tissue section fraction (Schmitz & Hof, 2005).

Statistical Analysis

All statistical procedures were performed using the R language and environment. Stereological parameters were designed to produce data that approximate a normal distribution by increasing the sampling frequency in highly heterogeneous biological samples. We investigated cell subtype distribution in a large number of samples (probes > 300) per region of interest (ROI), which has been shown to reduce the variance of data distributed in non-normal fashion (Schmitz & Hof, 2005). Accordingly, we evaluate hypothesized changes to mean estimates by calculating confidence intervals on the mean and standard deviation (SD), generally at the 95% level (alpha = 0.05) unless otherwise indicated. We also deploy analysis of variance (ANOVA) to evaluate differences in measurements of sample variability. All log transformations of data in this report were performed using a base of 10. Phylogenetic general least squares (PGLS) regression was also used to evaluate differences between species in this report with a phylogenetic tree based upon the Goodman et al. (2005) review, and with the R packages "ape" and "geiger." We assessed intra-class correlation coefficients per Koo & Li (2016) guidelines before pooling data across users, and report good to excellent intra-rater and inter-rater reliability. DJM and AH had intra-rater reliability estimates of 0.92 (n = 7, CI: 0.88 to 0.96) and 0.85 (n = 6, CI: 0.8 to 0.9), respectively, and inter-rater reliability was 0.77 (n = 5; CI: 0.71 to 0.83).

Results

Volumetrics

We found that the volume of the cortical mantle, as well as the granular cell layer 4, varies across primate V1 (Table 1) from approximately 200 mm^3 and 40 mm^3 in V1 mantle and layer 4 in the smallest new world monkeys, respectively, to more than about 3,000 mm^3 and 700 mm^3 in V1 mantle and layer 4 in hominoids, respectively (Table 2). Comparing the ratio of cortex devoted to layer 4, we estimate the average across primates to be 19.6%, with a SD of 1.5%, revealing the upper and lower 95% confidence intervals of the normalized distribution to range from 16.7% to 22.6%. These data indicate a general trend of increased volume in nocturnal (*Aotus, Otolemur*) compared to diurnal primates, and reveal that the *Aotus* has a significantly greater amount of tissue (24.4%) devoted to layer 4 than diurnal primates (Figures 1 – 5).

Genus	**Case**	**Side**	**Stain**
Homo	11_20	Left	Nissl
Pan	11_38	Left	Nissl
Papio	11_31	Left	Nissl
Macaca	10_14	Right	Nissl
Macaca	10_36	Left	Nissl
Macaca	11_47	Left	Nissl, NeuN
Saimiri	09_43	Left, Right	Nissl, NeuN
Saimiri	10_11	Right	Nissl
Saimiri	11_24	Right	Nissl
Aotus	07_77	Right	Nissl
Aotus	11_18	Left, Right	Nissl
Aotus	11_36	Left	Nissl, NeuN
Saguinus	00_05	Left	Nissl
Callithrix	01_114	Right	Nissl
Callithrix	06_48	Right	Nissl
Otolemur	05_13	Right	Nissl
Otolemur	06_50	Left	Nissl
Otolemur	08_10	Right	Nissl
Otolemur	13_08	Left	Nissl
Otolemur	14_25	Right	Nissl, NeuN

Table 3. Specimens included in this study.
Table displays all specimens used in this project, where both layer 4 and cortical mantle were available. Nissl, thionin; NeuN, antigen to neuronal nuclei; Mantle, from the pia mater to white matter (also called the cortical sheet); Layer 4, primary geniculo-recipient granular cell layer of the cortical mantle.

Genus	Species Average Mantle	Species Average Layer 4	Specimen Average Ratio	Sample
Homo	5,420	1,044	0.193	n = 1
Pan	3,498	657	0.189	n = 1
Papio	2,754	534	0.194	n = 1
Macaca	1,816	360	0.194	n = 3
Saimiri	995	177	0.174	n = 3
Aotus	461	105	0.244	n = 3
Saguinus	195	36	0.186	n = 1
Callithrix	202	39	0.183	n = 2
Otolemur	240	48	0.210	n = 4

Table 4. Volumetrics of V1 mantle and layer 4 in primates.
Each genus (sample size) included in this study. Volumetric estimates based upon the Cavalieri method in sections stained for Nissl and NeuN to reveal the location and extent of V1 mantle and layer 4 in cubic millimeters (mm^3). Ratio is the volume of layer 4 divided by the volume of the entire cortical mantle per specimen, showing the species average and sample size.

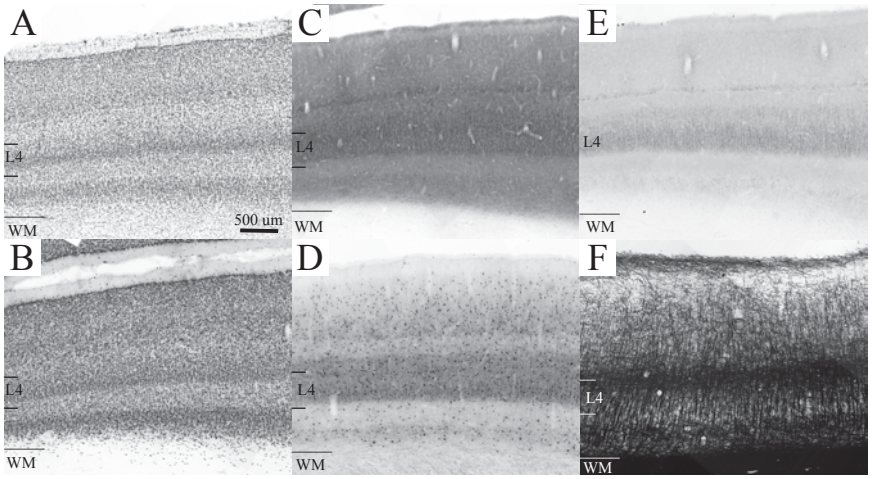

Figure 8. Low magnification image montages depicting V1 layer 4 in the macaque (*Macaca*).
Image stitches were acquired from nearly adjacent sections cut approximately perpendicular to the cortical mantle using a middle range magnification objective lens (x10) across the principal histological stains used to identify V1 layer 4 in the macaque monkey (*Macaca*). Stains for (A) Nissl substance using thionin, (B) antigen to neuronal nuclei (NeuN), (C) cytochrome oxidase, (D) parvalbumin, (E) antigen to vesicular glutamate transporter 2, (F) acetylcholinesterase. Layer 4 boundaries were only strictly defined using observations of cellular anatomy visible with Nissl or NeuN. WM, white matter; L4, layer 4; µm, micrometers. Scale bar is 500 µm.

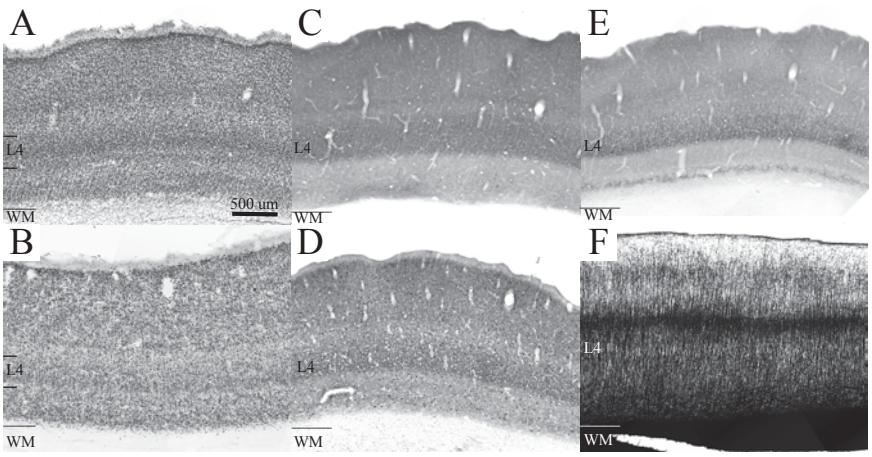

Figure 9. Low magnification image montages depicting V1 layer 4 in the squirrel monkey (*Saimiri*). Image stitches were acquired from nearly adjacent sections cut approximately perpendicular to the cortical mantle using a middle range magnification objective lens (x10) across the principal histological stains used to identify V1 layer 4 in the squirrel monkey (*Saimiri*). Stains for (A) Nissl substance using thionin, (B) antigen to neuronal nuclei (NeuN), (C) cytochrome oxidase, (D) parvalbumin, (E) antigen to vesicular glutamate transporter 2, (F) acetylcholinesterase. Layer 4 boundaries were only strictly defined using observations of cellular anatomy visible with Nissl or NeuN. WM, white matter; L4, layer 4; µm, micrometers. Scale bar is 500 µm.

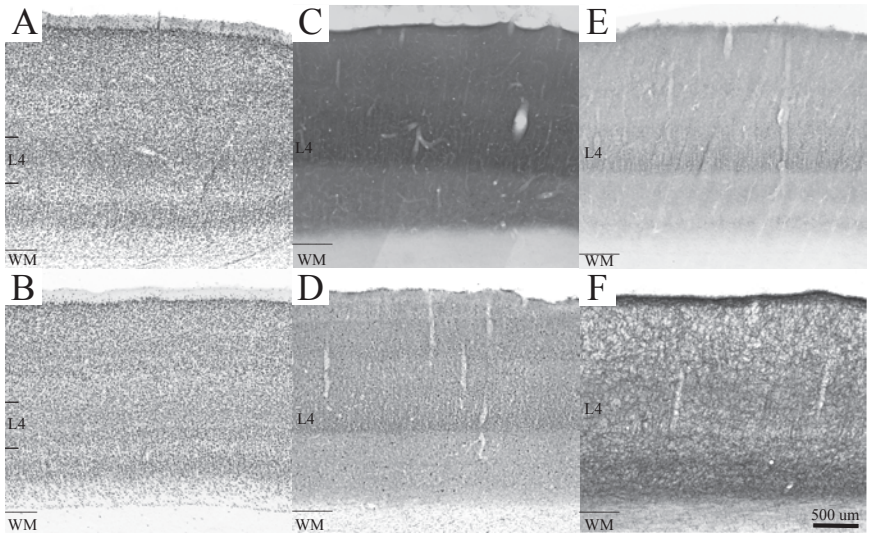

Figure 10. Low magnification image montages depicting V1 layer 4 in the owl monkey (*Aotus*). Image stitches were acquired from nearly adjacent sections cut approximately perpendicular to the cortical mantle using a middle range magnification objective lens (x10) across the principal histological stains used to identify V1 layer 4 in the owl monkey (*Aotus*). Stains for (A) Nissl substance using thionin, (B) antigen to neuronal nuclei (NeuN), (C) cytochrome oxidase, (D) parvalbumin, (E) antigen to vesicular glutamate transporter 2, (F) acetylcholinesterase. Layer 4 boundaries were only strictly defined using observations of cellular anatomy visible with Nissl or NeuN. WM, white matter; L4, layer 4; µm, micrometers. Scale bar is 500 µm.

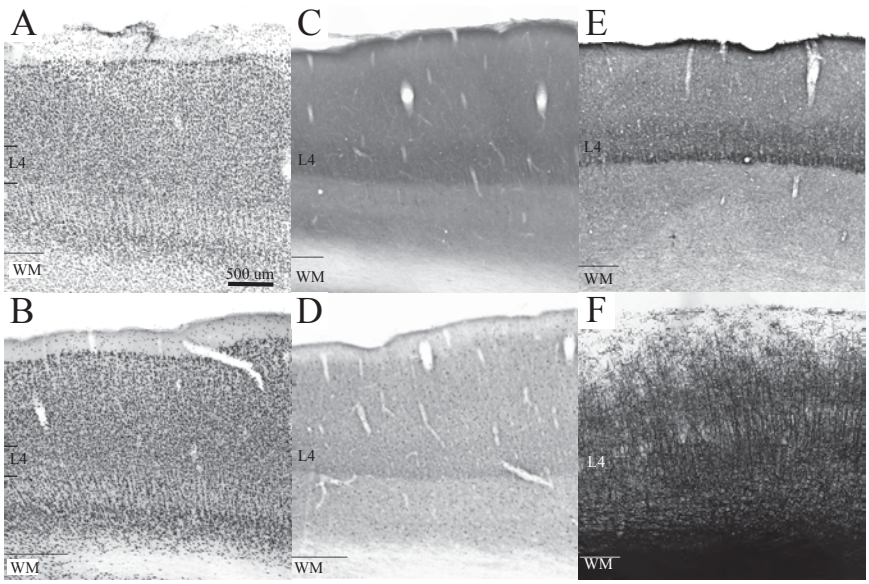

Figure 11. Low magnification image montages depicting V1 layer 4 in the galago (*Otolemur*).
Image stitches were acquired from nearly adjacent sections cut approximately perpendicular to the cortical mantle using a middle range magnification objective lens (x10) across the principal histological stains used to identify V1 layer 4 in the prosimian galago (*Otolemur*). Stains for (A) Nissl substance using thionin, (B) antigen to neuronal nuclei (NeuN), (C) cytochrome oxidase, (D) parvalbumin, (E) antigen to vesicular glutamate transporter 2, (F) acetylcholinesterase. Layer 4 boundaries were only strictly defined using observations of cellular anatomy visible with Nissl or NeuN. WM, white matter; L4, layer 4; µm, micrometers. Scale bar is 500 µm.

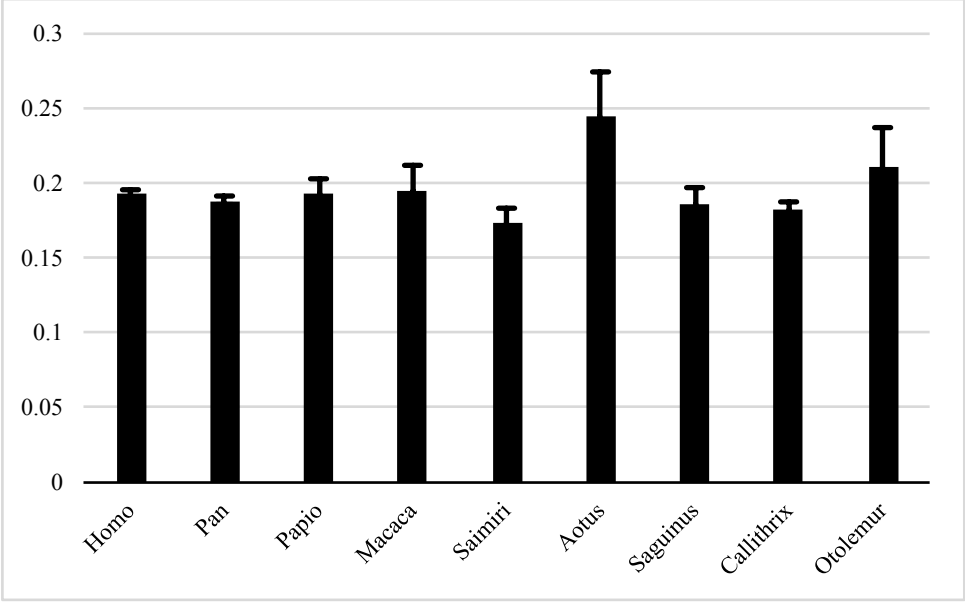

Figure 12. Volumetric ratio of layer 4 to mantle in V1 across primates.
Bar graph depicts ratio of volume in granular cell layer 4 to mantle in V1. Error bars depict SD. Ratio values in *Aotus* significantly different at the 95% level (alpha = 0.05).

Cellular composition

Our estimates indicate the total population of cells in V1 mantle ranges from 44 million in *Otolemur* to approximately 1.8 billion in *Homo* (Table 3). In our sample, the total population of neurons and glia in V1 mantle range from 30 and 14 million in *Otolemur*, respectively, to more than 1.1 billion and 700 million in *Homo*, respectively. Our estimates of the total cellular population of V1 layer 4 ranges from about 9 million in *Otolemur* to 460 million in *Homo*. These data also indicate a range of neurons and glia from 6 and 3 million in *Otolemur*, respectively, to 264 and 194 million in *Homo*, respectively. Plotting the log transformed total cell subtype counts revealed that the total number of glia scale with the total number of neurons across our sample (adjusted $R^2 = 0.9807$, $p < 0.001$; Figure 6). Our data revealed that, across the mantle and layer 4, the number of neurons is approximately twice the number of glia (glia to neuron ratio global mean = 0.456, SD = 0.110, 95% confidence range from 0.240 to 0.672), or stated another way, that the percentage of cells identified as neurons was around two-thirds (percent neurons global mean = 69.0%, SD = 4.9%, 95% confidence range from 59.5% to 78.6%) (Table 4). Our calculations thus reveal values for *Homo* (n=1; highest glia to neuron ratio = .704; lowest percent neurons = 58.7%) differ significantly (alpha = 0.05) from that of other primates (Figure 7).

Genus	Mantle Cells (M)	Mantle Neurons (M)	Mantle Glia (M)	Layer 4 Cells (M)	Layer 4 Neurons (M)	Layer 4 Glia (M)
Homo	1,867.7	1115.11	752.6	458.8	264.6	194.2
Pan	941.1	620.47	320.6	219.6	141.5	78.2
Papio	868.0	585.24	282.8	236.0	154.9	81.1
Macaca	666.2	471.93	194.3	178.9	125.1	53.8
Saimiri	581.7	428.73	153.0	144.8	105.5	39.3
Aotus	136.0	99.75	36.2	34.9	25.1	9.7
Saguinus	84.4	62.87	21.6	21.5	15.7	5.8
Callithrix	75.9	56.20	19.7	20.2	14.8	5.4
Otolemur	44.4	30.03	14.4	9.4	6.2	3.1

Table 5. Cellular composition of V1 mantle and layer 4 in primates.
Table shows stereological population estimates of cell subtypes using optical fractionator (all cells, neurons, and glia in millions, M) across the mantle and layer 4 of V1 in all primates included in this study.

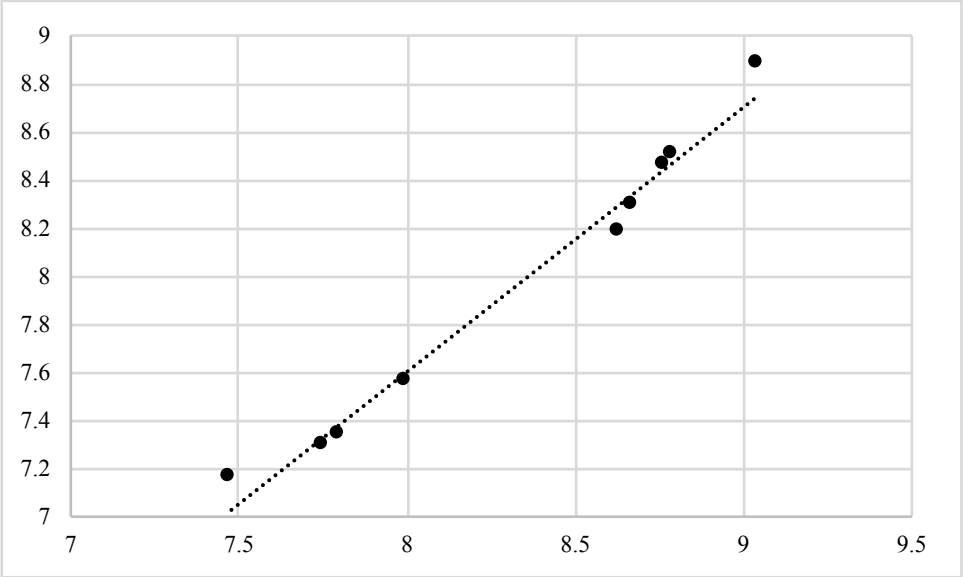

Figure 13. Plot of log-transformed population estimates of neurons and glial cells in primate V1 mantle. Graph depicts linear correlation between log-transformed values using the optical fractionator to estimate the populations of neurons (Y axis) and glia (X axis) in V1 mantle (same for values in V1 layer 4).

Genus	Mantle G:N Ratio	Layer 4 G:N Ratio	Average G:N Ratio	Mantle % Neuron	Layer 4 % Neuron	Average % Neuron
Homo	0.675	0.734	0.704	59.7%	57.7%	58.7%
Pan	0.517	0.553	0.535	65.9%	64.4%	65.2%
Papio	0.483	0.524	0.503	67.4%	65.6%	66.5%
Macaca	0.412	0.430	0.421	70.8%	69.9%	70.4%
Saimiri	0.357	0.373	0.365	73.7%	72.8%	73.3%
Aotus	0.363	0.386	0.375	73.4%	72.1%	72.7%
Saguinus	0.343	0.368	0.355	74.5%	73.1%	73.8%
Callithrix	0.351	0.366	0.359	74.0%	73.2%	73.6%
Otolemur	0.479	0.499	0.489	67.6%	66.7%	67.2%

Table 6. Summary table of cell subtype distribution across primates.
Table shows calculations of the distribution of cell subtypes in the sample. Glia to neuron ratio (G:N Ratio) and percent (%) neuron estimates are derived from Table 3 (see Methods for additional details).

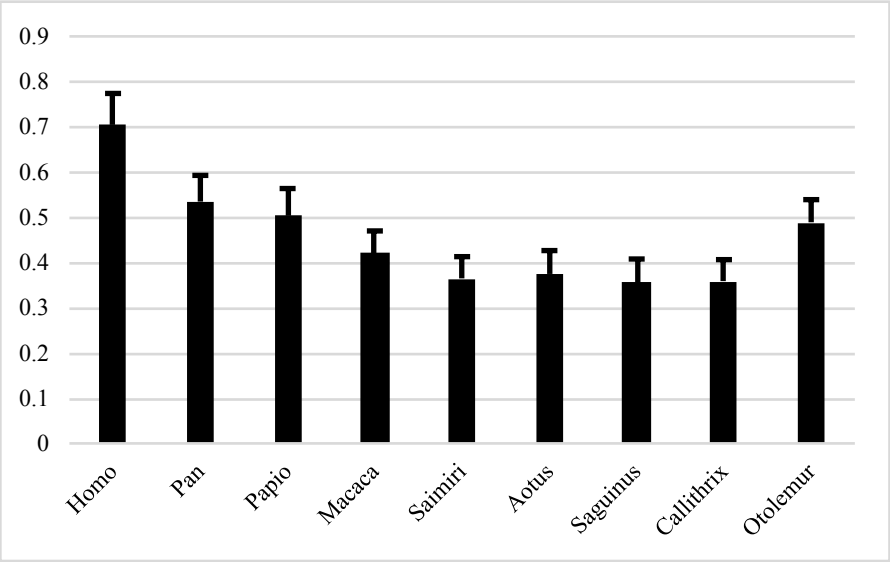

Figure 14. Average of mantle and layer 4 glia to neuron ratio across primates.
Bar chart depicting the glia to neuron ratio averaged across V1 mantle and layer 4 in each of the primates included in this report. Error bars depict SD.

Estimate densities

In V1 mantle, the data collected from this sample indicates the total cell density ranges from about 185,000 cells/mm^3 in *Otolemur* to about 584,000 cells/mm^3 in *Saimiri*, that neuron density ranges from about 124,000 neurons/mm^3 *Otolemur* to 430,000 neurons/mm^3 in *Saimiri*, and that glial density ranges from ~60,000 glia/mm^3 in *Otolemur* to 153,000 glia/mm^3 in *Saimiri*. Our data indicate higher average neuron density in V1 mantle of platyrrhine primates (~300,000 neurons/mm^3; *Callithrix, Saguinus, Aotus, Saimiri*) compared to catarrhine primates (~200,000 neurons/mm^3; *Macaca, Papio, Pan, Homo*), both of which are higher than the prosimian galago (~130,000 neurons/mm^3; *Otolemur*). A notable outlier in these data is the nocturnal owl monkey (*Aotus*) that exhibits V1 mantle neuron density much lower than other platyrrhines at ~200,000 neurons/mm^3. In contrast to neuron density, the density of glia in our sample of V1 mantle is more similar across large taxonomic groupings such that catarrhine and platyrrhines show glia densities around 110,000 glia/mm^3, with notable outliers being the high density of glia observed in *Homo* and *Saimiri*, and the low density of glia in nocturnal species (~70,000 glia/mm^3; *Aotus, Otolemur*) (Table 5).

	Mantle			Layer 4		
Genus	**Cells**	**Neurons**	**Glia**	**Cells**	**Neurons**	**Glia**
Homo	344.6	205.7	138.9	439.5	253.5	186.0
Pan	269.0	177.4	91.7	334.5	215.4	119.1
Papio	315.2	212.5	102.7	441.7	289.9	151.8
Macaca	366.8	259.8	106.9	497.3	347.8	149.5
Saimiri	584.4	430.7	153.7	819.3	596.7	222.5
Aotus	295.2	216.6	78.6	331.1	238.8	92.3
Saguinus	433.9	323.1	110.8	597.2	436.7	160.6
Callithrix	375.8	278.1	97.7	523.9	383.4	140.5
Otolemur	184.7	124.9	59.8	194.4	129.7	64.7

Table 7. Summary of cell subtype densities across primates.
Table shows density in thousands (K) of cell populations from Table 3 divided by the estimates in Table 2 (see Methods for additional details).

In V1 layer 4, our estimates reveal a range of total cell density from 194,000 cells/mm^3 in *Otolemur* to just over 800,000 cells/mm^3 in *Saimiri*, that neuron density ranges from 130,000 neurons/mm^3 in *Otolemur* to about 600,000 neurons/mm^3 in *Saimiri*, and that glial cell density ranges from 65,000 glia/mm^3 in *Otolemur* to ~222,000 glia/mm^3 in *Saimiri*. Similar to the taxonomic differences noted in data for V1 mantle, neuron density in V1 layer 4 is highest in platyrrhines at around 400,000 neurons/mm^3, intermediate in catarrhines at just under 300,000 neurons/mm^3, and lowest in the prosimian galago at about 130,000 neurons/mm^3. *Aotus* remains an outlier within platyrrhines exhibiting ~240,000 neurons/mm^3 in V1 layer 4. Similar to mantle data, glia density in V1 layer 4 is less variable across groups, with both platyrrhines and catarrhines exhibiting an average of ~150,000 glia/mm^3. Thus, as may be apparent by the highly stratified cortical layers in *Saimiri* (and other diurnal primates), and the relative lack of stratification in *Otolemur* (as well as the nocturnal *Aotus*), cellular density varies dramatically (up to 4 fold) between layer 4 and the mantle as a whole across different primate species (Table 5; Figure 8).

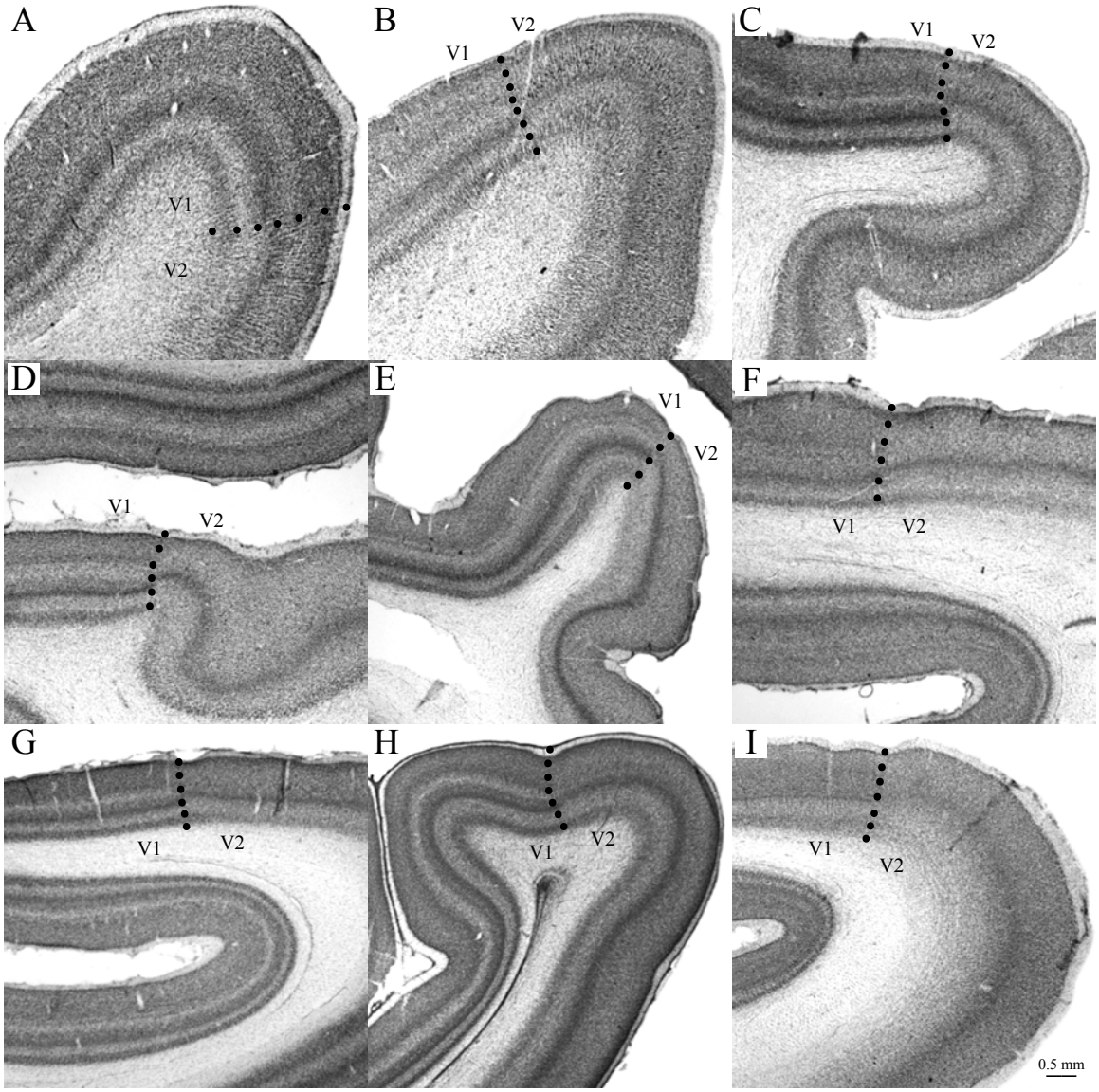

Figure 15. Low magnification images of the boundary between primary and secondary visual fields of the cerebral cortex across primates.
Images taken with a low magnification objective lens (x1) of sections stained for Nissl across the major primate taxa in this study: (A) *Homo*, (B) *Pan*, (C) *Papio*, (D) *Macaca*, (E) *Saimiri*, (F) *Aotus*, (G) *Saguinus*, (H) *Callithrix*, (I) *Otolemur*. Dotted line indicates the boundary between primary (V1) and secondary (V2) visual fields of the cerebral cortex. Scale bar is 0.5 millimeters (mm).

Comparing the estimates between mantle and layer 4 (Table 6), we initially describe an average increase in cell density across species of 29.1%. However, analysis of variance (ANOVA) showed the values from nocturnal primates *Aotus* and *Otolemur* had a significant effect upon the confidence interval estimate ($F = 36$, $p < 0.01$). Calculating the 95% confidence interval after excluding *Aotus* and *Otolemur* revealed a mean change in total cell density from mantle to layer 4 of 34.9%, with a SD of 5.9% and a confidence range of 23.2% to 46.6%. These calculations indicate the change in total cell density from mantle to layer 4 is significantly higher in diurnal (34.9%) compared to nocturnal (8.7%) species in our sample, a nearly 4-fold difference of the mean increase of cell density in the granular cell layer 4. Furthermore, our results

revealed an average increase in neuron and glia density between mantle and layer 4 across diurnal primates of 32.4% and 40.7%, respectively, and in nocturnal primates of 7.0% and 12.8%, respectively. Our data also revealed a small but consistent increase in the glia to neuron ratio of layer 4 across primates (mean = 6.1%, SD = 1.7%, confidence range = 2.7% to 9.5%). These data indicate that the majority of change in cell density from mantle to layer 4 is driven by neuron number, but that layer 4 exhibits a small but significant increase in the number of glia per neuron (Table 6; Figures 9-13). Our analysis also revealed, using phylogenetic general least squares (PGLS; see Methods) across measures in V1 mantle and layer 4, that *Homo* (n=1) exhibits a higher density of glia as neuron density increases than any other primate in this sample (Figure 14).

Percent Change from Mantle to Layer 4

Genus	Cell Density	Neuron Density	Glial Density	G:N Ratio
Homo	27.5%	23.2%	33.9%	8.7%
Pan	24.3%	21.4%	29.9%	6.9%
Papio	40.1%	36.4%	47.8%	8.4%
Macaca	35.6%	33.9%	39.8%	4.4%
Saimiri	40.2%	38.5%	44.8%	4.5%
Aotus	12.2%	10.3%	17.4%	6.4%
Saguinus	37.7%	35.2%	45.0%	7.3%
Callithrix	39.4%	37.9%	43.8%	4.3%
Otolemur	5.2%	3.8%	8.2%	4.2%

Table 8. Summary of changes in the cellular composition of V1 mantle to layer 4.
All values of percent change are calculated by dividing layer 4 by mantle values in each species included in this study (also see previous Tables).

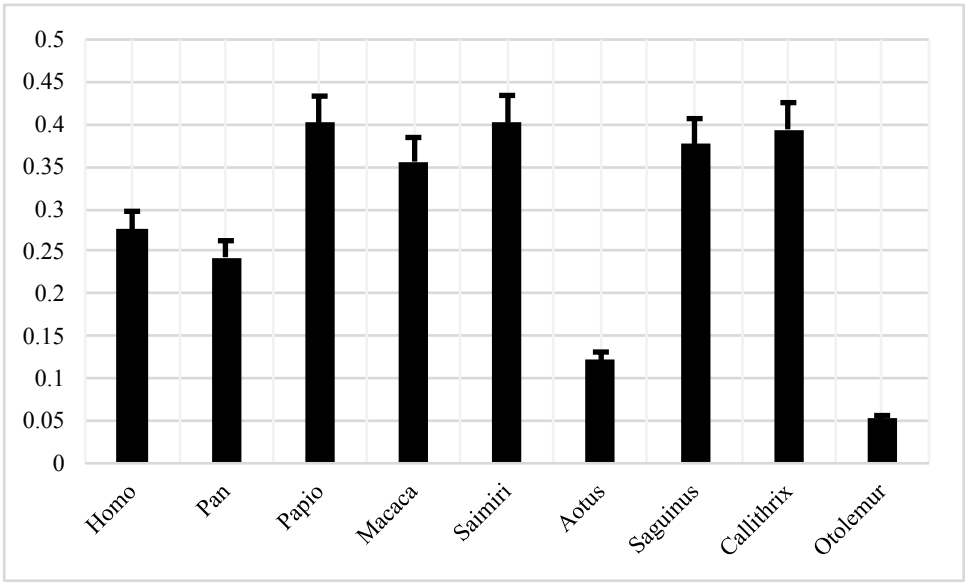

Figure 16. Graph of change in total cell density from V1 mantle to layer 4 across primates.

Bar graph depicts the estimated change in total cellular density from V1 mantle to layer 4 for each primate species included in this study. Error bars depict average variance of stereological estimates (8%). Nocturnal species (*Aotus, Otolemur*) exhibit values significantly lower than diurnal primates.

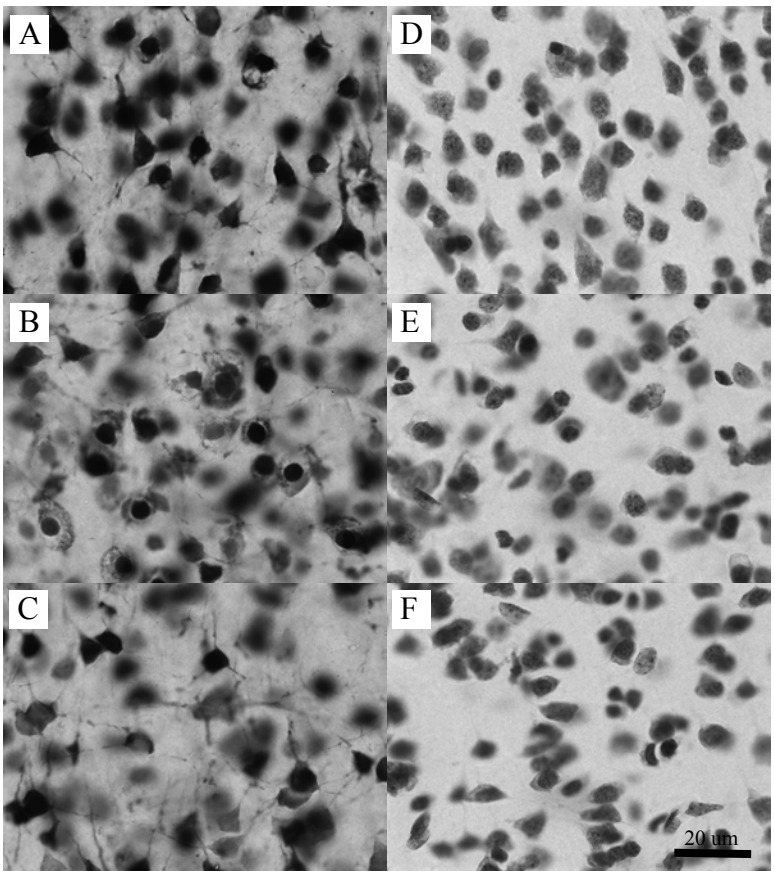

Figure 17. High magnification images of cells in macaque monkey (*Macaca*) V1.
Images taken with a high magnification oil-immersion objective lens (x100, 1.3 NA) of sections stained with an antigen to neuronal nuclei (A, B, C) and thionin for Nissl (D, E, F) in the macaque monkey (*Macaca*). Images depict cell density and morphology in the supragranular layer 3 (A, D), granular layer 4 (B, E), and the infragranular layer 6 (C, F) of V1. Scale bar is 20 μm.

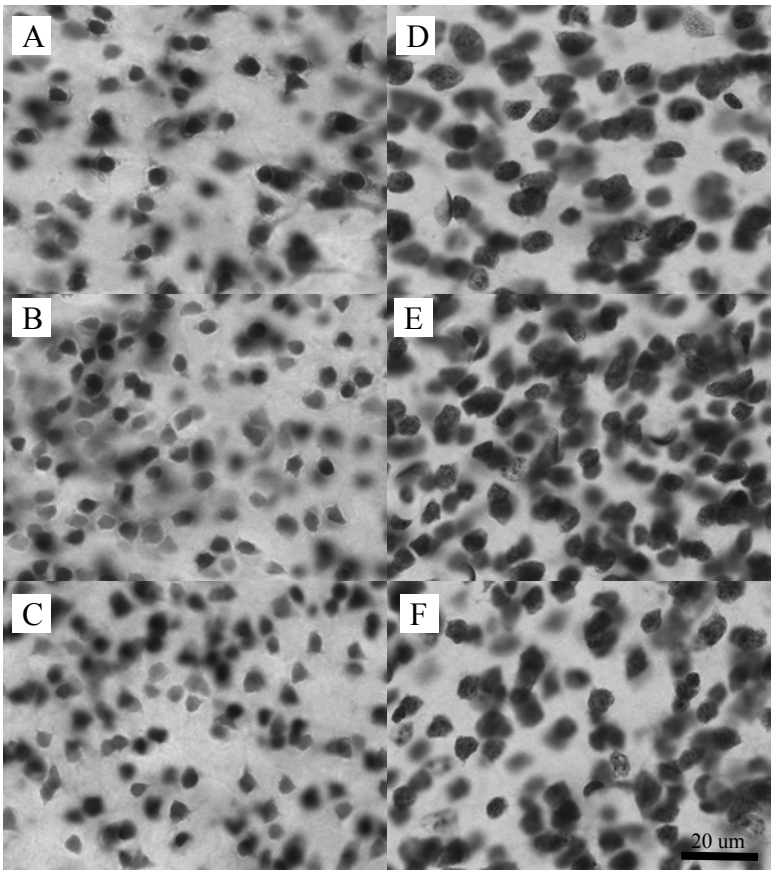

Figure 18. High magnification images of cells in the squirrel monkey (*Saimiri*) V1.
Images taken with a high magnification oil-immersion objective lens (x100, 1.3 NA) of sections stained with an antigen to neuronal nuclei (A, B, C) and thionin for Nissl (D, E, F) in the squirrel monkey (*Saimiri sciurius*). Images depict cell density and morphology in the supragranular layer 3 (A, D), the granular layer 4 (B, E), and the infragranular layer 6 (C, F) of V1. Scale bar is 20 µm.

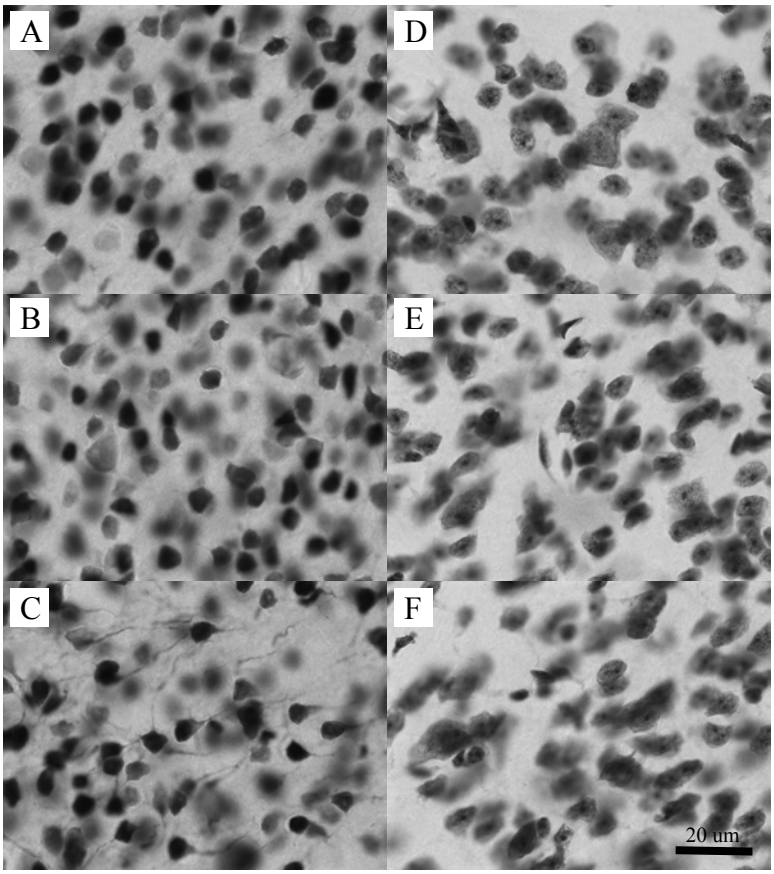

Figure 19. High magnification images of cells in the owl monkey (*Aotus*) V1.
Images taken with a high magnification oil-immersion objective lens (x100, 1.3 NA) of sections stained with an antigen to neuronal nuclei (A, B, C) and thionin for Nissl (D, E, F) in the owl monkey (*Aotus*). Images depict cell density and morphology in the supragranular layer 3 (A, D), the granular layer 4 (B, E), and the infragranular layer 6 (C, F) of V1. Scale bar is 20 µm.

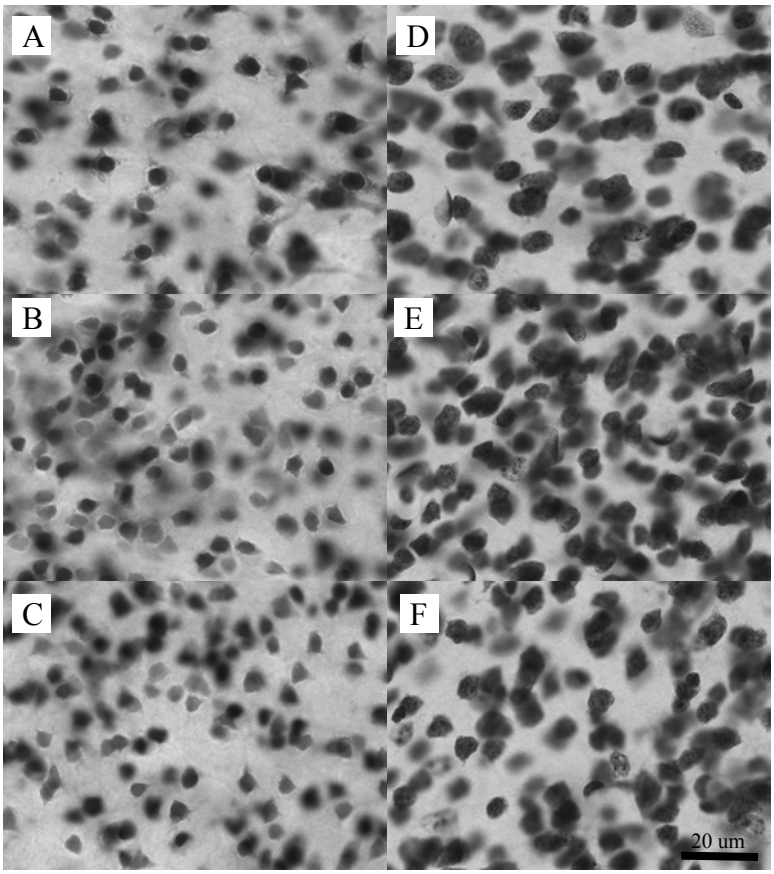

Figure 20. High magnification images of cells in the galago (*Otolemur*) V1.
Images taken with a high magnification oil-immersion objective lens (x100, 1.3 NA) of sections stained with an antigen to neuronal nuclei (A, B, C) and thionin for Nissl (D, E, F) in the prosimian galago (*Otolemur*). Images depict cell density and morphology in the supragranular layer 3 (A, D), the granular layer 4 (B, E), and the infragranular layer 6 (C, F) of V1. Scale bar is 20 μm.

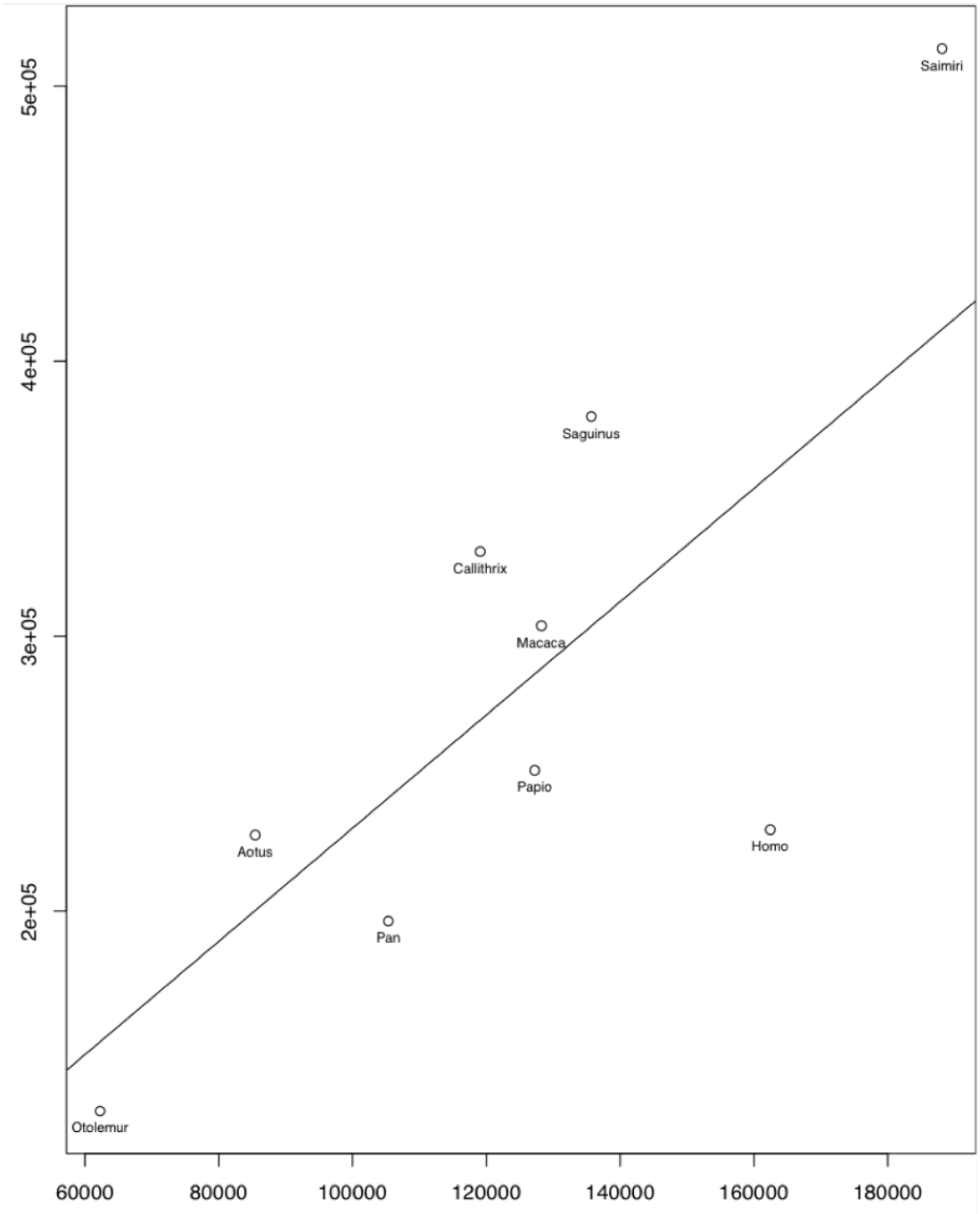

Figure 21. PGLS regression plot of glial against neuronal density in primate V1.
Graph depicts relationship between density of glial cells (X axis) as a function of neuron density (Y axis), revealing humans as outliers to bottom right of trendline ($R^2 = 0.613$).

Discussion

We report the first stereological estimates of the volume and cellular composition of the entire primary visual cortical field and primary geniculorecipient granular cell layer 4 across each of the major

primate taxonomic groups to reveal a mosaicism of phylogenetic trends in the evolution of cortical microstructure related to behavioral foraging ecology. Across primate V1 mantle, we show broad taxonomic differences such that platyrrhines exhibit the highest, prosimians the lowest, and that catarrhines exhibit intermediate cell density values. In agreement with previous qualitative comparative work, we provide a quantitative estimate of the increased cellular density in the anthropoid granular cell layer of approximately 30% (Brodmann, 1909; Hassler, 1967). We also provide evidence of a thicker granular cell layer 4 in nocturnal compared to diurnal primates, in agreement with Hassler (1967). Our data indicate the increased cell density of layer 4 is more pronounced in diurnal compared to nocturnal primates, and furthermore within diurnal primates, that hominoids (*Pan, Homo*) exhibit less change in layer 4 density than other catarrhines, or the platyrrhine primates in our sample. We also found that glia scale with neurons in V1 and that increasing neuron number drives the observed changes in overall cell density between V1 mantle and layer 4. Finally, our data provide evidence that the glia to neuron ratio is conserved across primate taxonomy, excepting humans. Together, these results provide evidence to suggest the volume and cellular composition of cortical visual circuits reflect the demands of diverse behavioral foraging ecologies across the primate order.

Understanding the anatomical constraints or parameters within which physiological processes occur in discrete circuits is an important index for the comparison of observations across nervous systems, whether those differ in clinical condition or phyletic relation; the most important of these for the current report consist of information about the connectivity, total volume, relative volume, and cellular composition of regions of interest. Korbinian Brodmann's (1909) pioneering work to use the homology of neurobiological structures as inferred from a broad mammalian sample as the basis of his schema of regional and laminar organization of the cerebral cortex set an important precedent to establish the utility of the comparative method. Brodmann (1909), using cellular morphology as well as to the position of cells within the cortical mantle, proposed the cortical mantle was composed of six layers. Of particular relevance to the current discussion, he proposed four subdivisions of the granular cell layer in V1 (4A, 4B, 4C alpha, 4C beta), such that an intermediate layer of larger pyramidal cells (Brodmann layer 4B) was included in this "granular cell layer" because of the presence of the supra- (4A) and subjacent (4C) layers that did actually contain small, granular cells (Hassler, 1967). Subsequent analysis of diurnal and nocturnal primates led Hassler (1967) to argue that Brodmann's layers 4A and 4B were actually part of layer 3 because Brodmann had supposedly misinterpreted the continuity of these layers across the transition into the secondary visual cortical field (Brodmann's area 18, or V2; for a review, see Casagrande & Kaas, 1994). However, neither Brodmann's (1909) nor Hassler's (1967) schemas were based upon more than an analysis of the distribution of cell bodies – they both lacked substantive information about the connectivity or function of these cells. However, the advent of single unit recording electrodes and anatomical tracers – molecules that when injected to tissue was transported either back to the cell body (retrograde) or towards the axon terminal (anterograde) – provided novel evidence to resolve the controversy. In particular, when subsequent research investigated the connections that characterize these cellular populations within V1, they found Brodmann's layer 4B consisted of projection neurons that received input from Brodmann's layer 4C alpha, and provided output to the middle temporal (MT) visual area (Allman & Kaas, 1972; reviewed in Casagrande & Kaas, 1994). Indeed, this pattern of projections from V1 to MT is now one of the known unique features of primate cortical organization, and which provides the most persuasive argument in favor of Hassler's (1967) terminology, as this projection is even conserved across primates exhibiting modifications to the supragranular layers (Preuss, 1999; Preuss & Coleman, 2002; Bryant et al., 2012). Although a complete review of connections between the lateral geniculate nucleus of the thalamus (LGN) and V1 are outside the scope of this report (for relevant reviews, see Casagrande & Ichida, 2011; Casagrande & Kaas, 1994), a few observations are pertinent to understanding the importance of the definition of the primary geniculorecipient granular cell layer 4 as defined by Hassler (1967), and its role in the primate visual system. Briefly then, the LGN contains three primary projection neuron subtypes, the magnocellular (M), parvocellular (P), and koniocellular (K) neurons, and the main projection to granule cells of V1 comes from the LGN. The use of tracers showed the upper tier of granule cells (Brodmann 4A; Hassler's layer 3)

receives input predominantly from K cells, while the lower tier is sometimes divided into two subdivisions, the top of which (Brodmann 4C alpha; Hassler's layer 4A) is dominated by input from LGN M neurons, the bottom of which (Brodmann 4C beta, Hassler's 4B) is dominated by input from LGN P neurons, and it is furthermore important to note that there is an intermediate zone within this tier of granule cells of overlapping projections from both M and P neurons (Casagrande & Ichida, 2011). Thus, the lower tier of granule cells receives the bulk of thalamic input, although because of the extensive degree of overlap in the physiological profile of M and P LGN neurons, discrete functions within the visual system apparently emerge downstream, leaving layer 4 to act as an important filter or bottleneck for the subsequent physiological activity of the visual system. Accordingly, the relative size and cellular composition of the primary geniculorecipient granular cell layer 4 within V1 mantle provides a measure of this circuit's relevance to the physiological phenotype of different primate species.

We measured the volume of V1 mantle and layer 4 across primates and generally found good agreement with the available literature. In particular, the stereological analysis of de Sousa et al. (2010) suggests a range of single hemisphere estimates of V1 mantle volume in *Homo* from as little as ~5 cm^3 to as much as ~10 cm^3, and Bush & Allman (2004) provide an estimate of 8 cm^3, suggesting that our estimate of 5.4 cm^3, although perhaps on the low end, is within the expected range. Volumetric estimates of V1 mantle for *Pan* are also in broad agreement, such that de Sousa et al. (2010) suggest a range of ~3 cm^3 to ~6 cm^3, and Bush & Allman (2004) provide an estimate of 5.5 cm^3, again suggesting that although our estimate of 3.5 cm^3 may on the low end, that it is still within the observed range. For V1 mantle in *Macaca*, estimates occupy a more restricted range, with de Sousa et al. (2010) indicating their specimen measured 1.4 cm^3, Bush and Allman (2004) indicate an estimate of 1.6 cm^3, and Giannaris & Rosene (2012) estimate an average of 1.48 cm^3, with a range from ~1 cm^3 to ~1.6 cm^3 (n=26). Our V1 mantle estimates include three subspecies of *Macaca*, and although we found an average of 1.8 cm^3, we also report a range of 1.3 to 2.4 cm^3 (our *Macaca mulatta* specimen was 1.7 cm^3), suggesting broad agreement across these samples. Bush & Allman (2004) also provide estimates for V1 mantle in some of the same species in our sample, and in general, given the above range of estimates in other species, our data are in broad agreement. In particular, Bush & Allman (2004) found an estimate for *Papio* of 3.8 cm^3, we report 2.8 cm^3, for *Saimiri* of 0.72 cm^3, we report 0.99 cm^3, for *Aotus* of 0.33 cm^3, we report 0.46 cm^3, and *Otolemur* of 0.27 cm^3, for which we report 0.24 cm^3. In contrast to V1 mantle estimates, we are the first to provide stereological estimates of the volume of layer 4 across the majority of primates in our sample. However, previous work has investigated the macaque monkey (primarily *Macaca mulatta*), and estimates from the Giannaris & Rosene (2012) study range from 257 to 389 mm^3. Our measurements of the volume of V1 layer 4 across three subsepecies of *Macaca* show relatively good agreement with the Giannaris & Rosene (2012) study, ranging from 311 to 427 mm^3 (our *Macaca mulatta* specimen was 340 mm^3). Another way of considering the commensurability of our estimates with that of previous work is to consider the ratio of volume devoted to the granular cell layer 4 out of the volume of the entire cortical mantle. The report from Giannaris & Rosene (2012) indicated the granular layer occupied an average of 22%, ranging from 18% to 24%, of the cortical depth. Our estimates of the average ratio of volume in V1 layer 4 to mantle in *Macaca* (mean = 19.4%, range from 16.3% to 21.4%) are in relatively good agreement, again considering that we report values from three different subspecies of *Macaca* (estimate for our *Macaca mulatta* case ranged from 17.9% to 20.7%). Given the dearth of research using stereological methods to investigate the granular cell layer across primates, we compared our delineation of V1 layer 4 to images and figures available from the literature (Balaram et al., 2013; Braitenburg, 1962; Bryant et al., 2012; Fitzpatrick et al., 1983; Garcia-Marin et al., 2013; Hassler, 1967; Lund, 1988; Mrzijak et al., 1996; Preuss & Coleman, 2002; Preuss et al., 1999; Wong & Kaas, 2010; Yoshioka & Hendry, 1995). In general, we found a comparable similarity between estimates as that observed with the Giannaris & Rosene (2012) study in *Macaca* (similar overall range with ~20% variation in specific estimates), but we also encountered a much greater variation in tissue preparation, and we found the greatest degree of agreement between estimates when multiple histological procedures were available. Thus, our volumetric estimates of V1 layer 4 reflect the common parcellation, and minor deviation from previous work is likely a consequence of sub-species differences, inter-individual variation, and the use of

distinct tissue preparation methods. Our results indicate layer 4 occupies less of the cortical mantle in diurnal (18.7%) compared to nocturnal primates (22.7%), but that the nocturnal owl monkey (*Aotus*) drove this difference as an outlier among platyrrhines (24.4%), in agreement with Hassler's (1967) previous observations. *Aotus* does not exhibit a retinal fovea (Wolin & Massopust, 1970), has lower visual acuity than the closely related diurnal *Saimiri*, and although the pattern of LGN M and P projections to V1 are similar to that seen in other primates, the increased thickness of layer 4 in this species is likely related to an increased reliance upon vision adapted for low-light conditions, favoring an increase in circuitry dedicated to motion detection over color vision and involving a reduction in layer 3 connections to and from extrastriate cortical areas (for reviews, see Casagrande & Kaas, 1994; Casagrande & Ichida, 2011).

In general, the cellular composition of the whole brain varies across taxonomic groups according to broad scaling rules, and a great deal of recent work has shown variation in the scaling of cell subtype populations across a variety of brain structures and mammalian taxa (for a review see Herculano-Houzel et al., 2015). Of particular interest, work in the cerebral cortex has shown the relationship between cell subtypes differs between primates and our closest mammalian relatives (Herculano-Houzel et al., 2006; 2007; 2012). Furthermore, previous work has shown variation in the cellular composition of regions across cerebral cortex (Herculano-Houzel et al., 2008; Collins et al., 2010), in cortical areas of closely related species exhibiting distinct behavioral foraging strategies (Campi et al., 2010), and within the same structure across broad samples of mammalian species (Lewitus et al., 2012). Together, these observations indicate diverse factors may influence cell subtype distribution, and that local variation in the cellular composition of specific pathways may reflect animal behavior, within the constraints imposed by phylogenetic trends. However, the interpretation of these data can at times be complicated by the use of distinct methods which by necessity may be more or less anatomically accurate both in terms of the regions sampled as well as the ability to distinguish cell subtypes (for review see Herculano-Houzel et al., 2015). In particular, the gold-standard method to distinguish glia from neurons must be considered immunolabeling, whether in slice-based histology (Giannaris & Rosene, 2012) or in homogenized samples (Herculano-Houzel & Lent, 2005). In this report, the majority of our counts were performed in sections stained following Nissl's method, and cell subtypes were identified according to the morphological characteristics recently summarized by Garcia-Cabezas et al. (2016), and may thus contain a certain degree of observer error, particularly in very densely populated brain areas (Herculano-Houzel et al., 2015), which is a primary factor in our decision to compare only the most robustly identifiable cells (i.e. neurons to glia as a group). Previous work by Giannaris & Rosene (2012) must be considered the gold-standard approach for quantitative analyses of the cellular composition of neurobiological samples as they had a large sample (n=26), used immunolabeling to identify cell subtypes, and counted cells across the full extent of V1 using stereological procedures. Giannaris & Rosene (2012) report an average of 416 million neurons and 184 million glia in V1 mantle, and in V1 granular layer, they report finding 120 million neurons and 53 million glia in one hemisphere, representing a G:N ratio of 0.44, percent neurons of ~68% (these authors found no difference in the G:N ratio between mantle and layer 4). Our results are in good agreement with this report, the only notable differences being that we found more neurons (490 million), thus reporting a slightly higher percent neurons or lower G:N ratio (0.42), that our volumetric estimates were higher, pushing our density estimates lower, and that we found a slightly higher number of glia in V1 layer 4. Perhaps most importantly, both studies found a similar increase in the number of neurons and glia (accounting for difficulties associated with identification using morphological criteria) moving from V1 mantle to layer 4. The volumetric differences are likely due to methodological differences such that Giannaris and Rosene (2012) performed counterstaining with NeuN, which may cause some shrinkage in free floating sections whereas our Nissl stained sections were mounted before staining and did not undergo additional procedures. Differences in the number of neurons and glia are likely due to the difficulty in our study, which did not perform immunolabeling, of correctly identifying neurons, particularly in highly populated areas such as layer 4 where we report finding an increase of the G:N ratio of ~6%. In another study of V1 mantle of *Macaca* by Lewitus et al. (2012) that used the traditional approach to stereology of counting objects per frame (Nv) rather than sampling the

entire cortical ROI, the authors report finding 380,000 neurons/mm^3, and 80,000 glia/mm^3, resulting in ~80% neurons or a G:N ratio of 0.23. In our sample, we found ~260,000 neurons/mm^3 and ~106,000 glia/mm^3, thus reporting a lower percent neurons (~70%) or higher G:N ratio of ~0.42. Differences between these estimates and the current report are likely due in part to Lewitus et al. (2012) not including layer 1 (which would increase the probability of encountering neurons), and their analysis of different subspecies of *Macaca* (of note, they report a G:N ratio of 0.27 for *Macaca mulatta*, which is closer to our estimates as well as that of Giannaris & Rosene, 2012). Lewitus et al (2012) report an analysis that covers the remaining taxa included in our sample, and thus we next compare the results from these species V1 mantle. Lewitus et al (2012) found neuron and glia density (estimates expressed in thousands for brevity), followed by G:N ratio, respectively (estimate from this report), for the following taxa: *Homo*: 234 (205) and 170 (138), 0.72 (.67); *Pan*: 208 (177) and 123 (91), 0.62 (.51); *Papio*: 275 (212) and 141 (102), 0.5 (.48); *Saimiri*: 478 (430) and 117 (153), 0.25 (.35); *Callithrix*: 320 (278) and 95 (97), 0.3 (.35); *Aotus*: 410 (216) and 59 (78), 0.12 (.36); *Otolemur*: 338 (124) and 151 (59), 0.45 (.47). Thus, we produced relatively good agreement in *Homo*, *Pan*, *Papio*, *Saimiri*, and *Callithrix*, and less agreement in *Otolemur* and *Aotus*. In general, these differences are most likely explained by inter-individual differences, the exclusion of layer 1 in the Lewitus et al (2012) study, potential differences in the processing of tissue samples, and by some potential difficulty in identifying cells by morphological criteria alone. However, if we consider what each study claimed to find, we find closer agreement. For instance, in this report, we conclude that neuron density drives cell density changes, and with this the Lewitus et al (2012) report is in broad agreement. Similarly, we found that *Homo* and *Pan* have lower cell density than other catarrhines, and that both of these groups have lower densities than platyrrhines, our reports are also in agreement. Similarly, both studies found relatively high G:N ratios in hominoids, and in particular *Homo*. The only real disagreement is that we found much lower cell counts in *Aotus* and *Otolemur*, and that we (as well as the Giannaris & Rosene 2012 study) tended to find higher numbers of glia, particularly in platyrrhines.

In comparing our estimates to the literature, we generally find agreement regarding the most important results that we discovered. In our estimates of V1 mantle volume, we found good agreement with previous work, notably that of de Sousa et al. (2010) and Bush & Allman (2004); we also found good agreement between our estimates and those reported by Giannaris & Rosene (2012) that also measured V1 layer 4 volume. Furthermore, Hassler reported in 1967 that *Aotus* had a thicker V1 layer 4, and our stereological estimate simply puts a number to that observation in a manner similar to how we also found an estimate for the increased density of cells in V1 layer 4 that is qualitatively apparent across anthropoid primates (~30%, also suggested by Giannaris & Rosene, 2012). Regarding the cellular composition of V1, we found excellent agreement with the Giannaris & Rosene (2012) paper that the increase in cell density between V1 mantle and layer 4 is approximately 30%, that this change is largely driven by increasing neuron number, and that glia scale nearly isometrically with neurons in V1. In comparison with the Lewitus et al. (2012) paper, we also found general agreement with the most important finding, namely that hominoids appear to have increased G:N ratios, and that humans in particular appear to be outliers.

In summary, our main findings indicate that *Aotus* and *Otolemur* exhibit lower neuron densities than in diurnal primates, and our estimate of the increased volume of V1 layer 4 in *Aotus* suggestive of significant modifications in this nocturnal primate to favor cortical laminar circuitry in support of the perception of motion over chromaticity. We also found that hominoids do not have as high neuron densities as other catarrhines, and that platyrrhines exhibit the highest neuron density. In addition, we found that glia in V1 scale with neuron number. Given the recent work by Mota & Herculano-Houzel (2014), it seems as though these data align with their predictions, such that if neuronal mass (i.e. size) is the primary predictor of glial numbers, then we could have anticipated, given the small size of neurons in V1, that fewer glia per neuron would be needed. Finally, our data agree with a previous report (Lewitus et al., 2012) that found *Homo* exhibits far more glia per neuron in V1 mantle than predicted by nonhuman primate data, suggesting, in light of our other findings of isometric scaling between neurons and glia in primate V1 and that hominoids exhibit lower neuron density than other catarrhines, that changes to the

supragranular circuits may be driving the production of larger neurons over the course of human evolution.

References

Aihara Y, Mashima H, Onda H, et al. (2000). Molecular cloning of a novel brain-type Na(+)-dependent inorganic phosphate cotransporter. J Neurochem. 74(6):2622–2625.

Allman J, Kaas JH. (1971). A representation of the visual field in the caudal third of the middle temporal gyrus of the owl monkey (*Aotus trivirgatus*). Brain Res. Aug7:31(1)85-105.

Balaram P, Hackett TA, Kaas JH. (2013). Differential expression of vesicular glutamate transporters 1 and 2 may identify distinct modes of glutamatergic transmission in the macaque visual system. J Chem Neuroanat. 50–51:21–38.

Balaram P, Kaas JH. (2014). Towards a unified scheme of cortical lamination for primary visual cortex across primates: insights from NeuN and VGLUT2 immunoreactivity. Front Neuroanat. Aug 15;8:81.

Balaram P, Kaas JH, Young N. (2014). Histological features of layers and sublayers in cortical visual areas V1 and V2 of chimpanzees, macaque monkeys, and humans. Eye Brain, 5.

Braitenburg V. (1962). A note on myeloarchitectonics. J Comp Neurol. Apr;118:141-56.

Brodmann K. (1909). Vergleichende Lokalisationslehre der Gro hirnrinde. Leipzig: Verlag von Johann Ambrosius Barth.

Bryant KL, Suwyn C, Reding KM, Smiley JF, Hackett TA, Preuss TM. (2012). Evidence for ape and human specializations in geniculostriate projections from VGLUT2 immunohistochemistry. Brain Behav Evol. 80(3):210-21.

Bush EC, Allman JM. (2004). Three dimensional structure and evolution of primate primary visual cortex. Anat Rec A Discov Mol Cell Evol Biol. Nov;281(1):1088-94.

Campi KL, Krubitzer L. (2010). Comparison of area 17 cellular composition in laboratory and wild-caught rats including diurnal and nocturnal species. Brain Behav Evol. 77(2):116-30.

Casagrande VA, Ichida JM. (2011). Processing in the Lateral Geniculate Nucleus (LGN). In Adler's Physiology of the Eye, 11th edition. A Alm, PL Kaufman, (lead) LA Levin, SFE Nilsson, J Ver Hoeve, SM Wu, editors. Mosby, Elsevier, pp. 574-585.

Casagrande VA, Kaas JH. (1994). The Afferent, Intrinsic, and Efferent Connections of Primary Visual Cortex in Primates. In Primary Visual Cortex in Primates. A Peters, KS Rockland, editors. Boston, MA: Springer US. Vol. 10, pp. 201–259.

Collins CE, Turner EC, Sawyer EK, Reed JL, Young NA, Flaherty DK, Kaas JH. (2016). Cortical cell and neuron density estimates in one chimpanzee hemisphere. Proc Natl Acad Sci U S A. 113(3), 740–745.

Cowey A, Stoerig P. (1989). Projection patterns of surviving neurons in the dorsal lateral geniculate nucleus following discrete lesions of striate cortex: implications for residual vision. Exp Brain Res. 75(3):631-8.

de Sousa AA, Sherwood CC, Schleicher A, Amunts K, MacLeod CE, Hof PR, Zilles K. (2010). Comparative cytoarchitectural analyses of striate and extrastriate areas in hominoids. Cereb Cortex. Apr;20(4):966-81.

Fitzpatrick D, Itoh K, Diamond IT. (1983). The laminar organization of the lateral geniculate body and the striate cortex in the squirrel monkey (*Saimiri sciureus*). J Neurosci. Apr;3(4):673-702.

Garcia-Cabezas MA, John YJ, Barbas H, Zikopoulos B. (2016). Distinction of Neurons, Glia and Endothelial Cells in the Cerebral Cortex: An Algorithm Based on Cytological Features. Front Neuroanat. Nov 1;10:107.

Garcia-Marin V, Ahmed TH, Afzal YC, Hawken MJ. (2012). Distribution of vesicular glutamate transporter 2 (VGluT2) in the primary visual cortex of the macaque and human. J Comp Neurol. 521(1):130–151.

Giannaris EL, Rosene DL. (2012). A stereological study of the numbers of neurons and glia in the primate visual cortex across the lifespan of male and female rhesus monkeys. J Comp Neurol. Oct 15;520(15):3492-508.

Goodman M, Grossman LI, Wildman DE. (2005). Moving primate genomics beyond the chimpanzee genome. Trends Genet. Sept;21(9):511-7.

Hässler RG. (1967). Comparative anatomy of the central visual system in day- and night-active primates. In: Hässler R, Stephen S, editors. Thieme, Stuttgart: Evolution of the forebrain. Springer. p. 419-434.

Hendrickson AE, Van Brederode JF, Mulligan KA, Celio MR. (1991). Development of the calcium-binding protein parvalbumin and calbindin in monkey striate cortex. J Comp Neurol. 307(4): 626–646.

Herculano-Houzel S, Catania K, Manger PR, Kaas JH (2015). Mammalian brains are made of these: a dataset of the numbers and densities of neuronal and nonneuronal cells in the brain of glires, primates, scandentia, eulipo- typhlans, afrotherians and artiodactyls, and their relationship with body mass. Brain Behav Evol 86:145–163.

Herculano-Houzel S, Collins CE, Wong P, Kaas JH. (2007). Cellular scaling rules for primate brains. Proc Natl Acad Sci U S A. Feb 27;104(9):3562-7.

Herculano-Houzel S, Collins CE, Wong P, Kaas JH, Lent R. (2008). The basic nonuniformity of the cerebral cortex. Proc Natl Acad Sci U S A. Aug 26;105(34):12593-8.

Herculano-Houzel S, Lent R. (2005). Isotropic fractionator: a simple, rapid method for the quantification of total cell and neuron numbers in the brain. J Neurosci. Mar 9;25(10):2518-21.

Herculano-Houzel S, Mota B, Lent R. (2006). Cellular scaling rules for rodent brains. Proc Natl Acad Sci U S A. Aug 8;103(32):12138-43.

Herculano-Houzel S. (2012). The remarkable, yet not extraordinary, human brain as a scaled-up primate brain and its associated cost. Proc Natl Acad Sci U S A. Jun 26;109 Suppl 1:10661-8.

Hubel DH, Wiesel TN. (1959). Receptive fields of single neurones in the cat's striate cortex. J. Physiol. 148:574–591.

Koo TK, Li MY. (2016). A guideline of selecting and reporting intraclass correlation coefficients for reliability research. J Chiropr Med Jun; 15(2):155-63.

Lewitus E, Hof PR, Sherwood CC. (2012). Phylogenetic comparison of neuron and glia densities in the primary visual cortex and hippocampus of carnivores and primates: evolutionary constraints on glia-neuron densities. Evolution. 66(8), 2551–2563.

Lund JS. (1988). Anatomical organization of macaque monkey striate visual cortex. Annu Rev Neurosci. 11:253-88.

Miller DJ, Balaram P, Young NA, Kaas JH. (2014). Three counting methods agree on cell and neuron number in chimpanzee primary visual cortex. Front Neuroanat, 8.

Mota B, Herculano-Houzel S. (2014). All brains are made of this: a fundamental building block of brain matter with matching neuronal and glial masses. Front Neuroanat. Nov 12;8:127.

Mrzljak L, Levey AI, Rakic P. (1996). Selective expression of m2 muscarinic receptor in the parvocellular channel of the primate visual cortex. Proc Natl Acad Sci U S A. Jul 9;93(14):7337-40.

Mullen RJ, Buck CR, Smith AM. (1992). NeuN, a neuronal specific nuclear protein in vertebrates. Development. Sep;116(1):201-11.

Nieuwenhuys R. (2013). The myeloarchitectonic studies on the human cerebral cortex of the Vogt-Vogt school, and their significance for the interpretation of functional neuroimaging data. Brain Struct Funct. Mar;218(2):303-52.

Pelvig DP, Pakkenberg H, Stark AH, Pakkenberg B. (2008). Neocortical glial cell numbers in human brains. Neurobiol Aging. Nov;29(11):1754-62.

Preuss TM, Qi H, Kaas JH. (1999). Distinctive compartmental organization of human primary visual cortex. Proc Natl Acad Sci U S A. 96(20):11601-11606.

Preuss TM, Coleman GQ. (2002). Human-specific organization of primary visual cortex: alternating compartments of dense Cat-301 and calbindin immunoreactivity in layer 4A. Cereb Cortex. Jul;12(7):671-91.

Schmitz C, Hof PR. (2005). Design-based stereology in neuroscience. J Neurosci. 130(4), 813–831.

Sherman SM, Guillery RW. (2005). Exploring the thalamus and its role in cortical function, 2nd edn. Cambridge, MA: MIT Press.

Sherwood CC, Stimpson CD, Raghanti MA, Wildman DE, Uddin M, Grossman LI, Goodman M, Redmond JC, Bonar CJ, Erwin J, Hof PR. (2006). Evolution of increased glia-neuron ratios in the human frontal cortex. Proc Natl Acad Sci U S A. 103(37), 13606– 13611.

Stoerig P, Cowey A. Blindsight. (2007). Curr Biol. Oct 9;17(19):R822-4.

Sun W, Tan Z, Mensh BD, Ji N. (2016). Thalamus provides layer 4 of primary visual cortex with orientation- and direction-tuned inputs. Nat Neurosci. Feb;19(2):308-15.

Wolf HK, Buslei R, Schmidt-Kastner R, et al. NeuN: a useful neuronal marker for diagnostic histopathology. J Histochem Cytochem. 1996; 44(10):1167–1171.

Wolin LR, Massopust LC. (1970). Morphology of the primate retina. In The Primate Brain. CR Noback, and W Montagna, editors. Appleton-Century-Crofts, New York, pp. 1-27

Wong-Riley M. (1979). Changes in the visual system of monocularly sutured or enucleated cats demonstrable with cytochrome oxidase histochemistry. Brain Res. 171(1):11–28.

Wong P, Kaas JH. (2010). Architectonic subdivisions of neocortex in the Galago (*Otolemur garnetti*). Anat Rec (Hoboken). 293(6):1033–1069.

Yoshioka T, Hendry SH. (1995). Compartmental organization of layer IVA in human primary visual cortex. J Comp Neurol. Aug 21;359(2)213-20.

CHAPTER 4

CELLULAR MORPHOLOGICAL EFFECTS OF DEAFFERENTATION

Introduction

Spinal cord trauma in humans is difficult to diagnose and treat because the anatomical changes most readily visible with noninvasive imaging methods to guide therapy in the clinic are not clearly related to the potential for recovery as our understanding of the effects of deafferentation on the primate sensorimotor system are not fully understood (Kaas et al., 1983; 2008; Rowland et al., 2008). Previous work in a variety of mammals has shown that deafferentation leads to physiological and anatomical reorganization across the neuraxis of all sensory systems (Cowan, 1970; Jones, 2000; Kaas et al., 1983; 2008). Indeed, the functional reorganization observed in animal models is markedly similar to clinical observations in humans of perturbed sensory experiences, such as phantom limb pain (Jones, 2000; Moore et al., 2000; Ramachandran, 1993). However, the cellular anatomical changes that follow deafferentation and correlate with functional reorganization are not well understood.

Primates are the most appropriate model to understand the effects of trauma affecting manual dexterity in humans because of the similarity of their somatosensory systems (Darian-Smith, 2009), but distinct types of trauma affect different combinations of pathways within this system, leading to conflicting reports of the effect of deafferentation (reviewed in Kaas et al., 1983; 2008). In humans and primates, sensory information from the hand is conveyed through peripheral receptors in the skin through the cervical dorsal root ganglion (DRG), which sits just outside the spinal cord, and on to two alternative pathways within the somatosensory system which support holistic tactile sensation and the proprioceptive feedback necessary for smooth, coordinated movement (Mountcastle, 2005). Projections from the DRG either ascend directly through the dorsal column pathway (DC) to the ipsilateral cuneate nucleus of the brainstem (the focus of our investigation is on the internal cuneate nucleus, or ICN), or ramify upon sensory neurons within the dorsal horn of the spinal cord, primarily in lamina IV (Liao et al., 2015). Neurons within the dorsal horn then project to the ipsilateral ICN, forming a second-order pathway to the ICN, as well as contralaterally to form the spinothalamic pathway, most known for its role in the sensation of temperature and pain (Reed et al., 2016). Within this second-order pathway of projections from the dorsal horn to the ipsilateral ICN, the majority of axons (~95%) travel through the cuneate fasciculus within the DC, as had been previously known (Kaas et al., 2008). Recent work, however, has shown that a small minority (~5%) of connections within this second-order pathway travel through the dorsolateral funiculus (Liao et al., 2015), ostensibly forming a third-order path from peripheral receptors to the ipsilateral ICN. Projections from the ICN terminate in the ventroposterior lateral thalamic nucleus (VPL), from which connections to multiple sensory fields of the cerebral cortex supporting sensorimotor functions arise (Reed et al., 2016). Thus, limb amputation removes peripheral receptor input, but leaves the dorsal root ganglion (DRG) intact, whereas dorsal rhizotomies sever all input from affected DRG but leave overlapping input from adjacent DRG intact, and lesions to the spinal cord itself may affect or avoid multiple, potentially redundant pathways by virtue of the size and location of the lesion (Darian-Smith, 2009; Jones, 2000; Kaas et al., 1983; Reed et al., 2016). In addition, doubt as to the potential role that even a few (~1%) spared connections might play in plasticity-related processes has left open questions about the consequences of deafferentation upon the transneuronal atrophy of cellular microstructure which mediates behavioral recovery (Kaas et al., 2008).

Previous work has shown that deafferentation produces significant functional reorganization of the somatosensory neuraxis in a variety of mammals (for a review see Kaas, 1994). However, several studies of the sensorimotor system in the rat (Waite, 1984; Wall & Cusick, 1984; 1986), cat (Kalaska & Pomeranz, 1979; McKinley & Smith, 1990; Juliano et al., 1994), raccoon (Carson et al., 1981; Kelahan et al., 1981; Kelahan & Doetsch, 1984), and primates (Florence et al., 1996) suggest important differences

in the physiological effects of deafferentation in development compared to adulthood (see review by Cusick, 1996).

A variety of studies provide evidence of numerous measures of anatomical atrophy following deafferentation during either development or adulthood (Arvidsson & Aldskogius, 1978; Arvidsson & Grant, 1979; Avendano & Dykes, 1996a; 1996b; Jacquin & Rhoades, 1985; Loewy, 1973; Renehan et al., 1989; Rhoades et al., 1993; Woods et al., 2000), including but not limited to changes in regional volume, connectivity, cellular chemistry, cellular morphology, and the number or distribution of neurons within deafferented regions of interest. However, few studies have explicitly measured the same anatomy following deafferentation during development and as adults (Bowlus et al., 2003). In order to more closely evaluate the anatomy of transneuronal atrophy following deafferentation in primates, this project seeks to provide more information about the effect of dissimilar types of trauma during development, as well as the consequences of a single type of trauma in a developmental and adult sample.

Materials & Methods

Sample

All procedures involving animals and animal tissues followed the NIH Guidelines for the Use of Laboratory Animals, and were approved in advance by the Vanderbilt University Institutional Animal Care and Use Committee. The study sample consisted of tissue from the brainstem of macaque monkeys (*Macaca radiata*, n = 6), galagos (*Otolemur*, n = 2), and squirrel monkeys (*Saimiri boliviensis* n = 17; *Saimiri sciurius* n = 3). Specimens either underwent trauma during development (*Macaca, Otolemur*), as a result of amputation or lesion to the dorsal column (DCL), or DCL as an adult (*Saimiri*). In our developmental sample of three macaques and one galago, we observed the effects of DCL in two macaques (one with unilateral, one with bilateral lesions), and amputation in one macaque and one galago.

Surgerical procedures

In all specimens that underwent dorsal column lesions, animals were first anesthetized with ketamine (15 mg kg^{-1}, intramuscular) and xylazine (0.4 mg kg^{-1}, intramuscular), and the dorsal column fibers were sectioned at the C3-C5 level with sharp fine forceps. In cases with amputations, animals underwent therapeutic amputation of the arm by veterinary doctors for treatment of injuries. Therapeutic amputation or DCL in developmental cases occurred within the first year of life.

Perfusion

Following electrode mapping, specimens were injected with a lethal dose of sodium pentobarbital (60 mg/kg or more; Sigma-Aldrich, Saint Louis, MO, USA) and perfused intracardially, first with PBS, and then in quick succession by 4% paraformaldehyde (PFA, Sigma-Aldrich, Saint Louis, MO, USA) in PBS, and finally 4% PFA in PBS with 10% sucrose. Following perfusion, the cortical hemispheres were bisected along the corpus callosum, cortical and brainstem structures were separated, the brain was cleaned of vasculature and pia, and then cut into blocks containing regions of interest. After blocking, samples were immersed in 30% sucrose and PBS at 4 degrees Celsius overnight prior to sectioning at between 40 and 50 µm on a sledge microtome (American Optical, model #860, clearance angle = 19˚) while the tissue was held below 0 degrees Celsius. Upon sectioning, brain slices are grouped into 1 in 10 series for histological processing.

Histology and Identification of Anatomical Regions and Objects

All specimens included in this research project were stained for cytochrome oxidase (CO, Wong-Riley, 1979), and either thionin for Nissl or an antigen to neuronal nuclei (NeuN; AB667 from Millipore, Billerica, MA, USA), which selectively stains neurons (Mullen et al., 1992), and when available, cholera toxin subunit B (CTB) to visualize tracers injected to peripheral structures (Angelucci et al., 1996; Liao et al., 2016). For full details of histology and immunohistochemistry, see Qi et al., 2011; 2013. The use of multiple stains and previously published descriptions facilitated the identification of the cuneate nucleus in each species of primate included in this project (Strata et al., 2003). We primarily defined the cuneate nucleus by its dense reactivity for CO, which decreases in the bordering fiber tracts which separate it from the external cuneate, trigeminal nucleus, and gracile nucleus (Florence et al., 1988; 1989; Strata et al., 2003). Immunohistochemical staining for NeuN selectively reveals the presence of neurons (Mullen et al., 1992; Wolf et al., 1996), and thionin was used following Nissl's staining method to visualize ribosomes within the cell body to reveal the cellular morphology used to distinguish neurons from glia (Garcia-Cabezas et al., 2016). Neurons were distinguished from glia based upon their size, opacity, and the presence of nucleoli. As recently reviewed by Garcia-Cabezas et al. (2016), neurons were distinguished by the presence of darkly stained nucleoli within a more moderately stained nucleus within the more pale-staining perikaryon or cytoplasm-filled cell soma, and which, in the brainstem, are often noticeably larger than the other objects within the field of view.

Stereological measurement of regional volume and cell number

All measurements and images were collected using a computerized stereology system that consisted of a Nikon E80i microscope outfitted with ×2 to ×100 oil immersion (NA = 1.3) objective lenses, and connected to a motorized stage (Ludl Instruments) running the commercially available StereoInvestigator software (MBF Bioscience, Williston, VT) on a Dell desktop with 8 GB RAM and 1TB storage. Contours were drawn under ×4 objective lens magnification, and images were acquired or counts were made with 100× oil immersion objective lens magnification under Köhler illumination. A mean of 324 probes, with a standard error of the mean (SEM) of 41, were investigated per specimen included in this report. We used the Cavalieri estimator, optical fractionator, and nucleator workflows available with StereoInvestigator to measure the volume of anatomical regions, the number of neurons, and the volume of neurons, respectively (Gundersen et al., 1988).

DJM performed the initial pilot tests in each species included in this project to establish the appropriate stereological sampling parameters to maintain a low coefficient of error (Gundersen (m=1) CE < 0.08) (Schmitz & Hof, 2005): number of sections to be investigated (n = 9-11, mode = 10), probe area (15-25 μm^2), probe height (6 μm), guard zone (3 μm), frame step (120 μm^2 to 180 μm^2) and frequency of thickness measurements (1 in 8). Across all specimens investigated, we ended up counting a mean of 78, and a standard deviation of 21, neurons per specimen, yielding Gundersen (1999) and Schmitz & Hof (2005) coefficients of error (CE) that ranged from 0.07 to 0.19 (mean = 0.13, standard deviation = 0.06). DJM conducted all the regional volumetric analyses using the Cavalieri method (180 μm^2) in sections stained for CO, Nissl, or NeuN. DJM performed the first counts using the optical fractionator in each species in this study before using the systematic random sampling image stack acquisition workflow to archive stereological images for subsequent analysis by additional investigators (RP, as well as for DJM's confirmatory analyses) through our custom crowdsourcing website built with support from the Vanderbilt Institute for Digital Learning.

Objects were marked as neurons or glia either according to evidence of cellular morphology as discussed above, or by immunolabeling. The majority of the counting performed in this project took place on sections stained for NeuN, minimizing the potential for glia to be counted and measured as neurons across investigators. We used the top of the cell soma as the unique identifying feature of each object to avoid the double-counting problem. Lines of inclusion and exclusion defined the probe dimensions within the X and Y domain, and the top section following the guard zone was excluded as the third dimensional (Z domain) line of exclusion. We replicated these stereological parameters on our custom crowdsourcing website, with the addendum that markers were placed in the first image where the top of the cell soma

came into focus within the dimensions of the probe (image depth = 0.5 μm), and that the size of neurons using an adjustable crosshair (rays = 4) was measured on the image depicting the middle Z-range of the cell of interest. The total number of cells was then determined by multiplying the number of counts by the reciprocals of the area section fraction (asf), serial section fraction (ssf) and the tissue section fraction (tsf) (Schmitz & Hof, 2005).

Statistical Analysis

Stereological parameters were designed to produce data that approximate a normal distribution by increasing the sampling frequency in highly heterogeneous biological samples. In the cuneate nucleus, this was facilitated by an approximately spherical shape (shape coefficient in cuneate = 1.7, where sphere = 1 and shape 4 = rectangular or highly convoluted oblong object (e.g. primary visual cortex)), and thus we evaluate hypothesized changes in neuron number by calculating the 95% confidence intervals of Z-score transformed data. In the analysis of neuronal volume, initial descriptive statistical measures indicated the data are not normally distributed within the nucleus on each side of the brainstem within a given specimen, but are in fact bimodal, such that neurons fall into categories of large or small, in line with previous research (Beidenbach, 1972). However, an advantage of the nucleator protocol (Gundersen et al., 1988) is that it calculates the volume of objects from the mean measured radius (rays = 4), which is more normally distributed than this value multiplied and raised to the third power (Volume = 4/3*pi*radius^3). In addition, the distribution of mean measured radius length is approximately normal when Z-score transformed and compared across subjects (i.e. in lengths measured across groups of nuclei, such as control vs lesioned). Thus, we compared Z-score transformed mean measured radius length across nuclei in different experimental conditions to assess differences in neuronal size. We present our statistical tests by evaluating the 95% confidence intervals on the Z-scores of these radius lengths by groups.

We report good intra-rater and inter-rater reliability as assessed through intra-class correlation coefficients, validating the combination of user data into a single pool for comparisons across experimental conditions (Koo & Li, 2016). DJM and RP had intra-rater reliability estimates of 0.84 (n = 4, CI: 0.81 to 0.87) and 0.89 (n = 6, CI: 0.86 to 0.92), respectively, and inter-rater reliability was 0.78 (n = 5; CI: 0.71 to 0.85).

Results

Regional Volume

Three primate species (Table 1) were used to study the effects of trauma on the internal cuneate nucleus (ICN), which can be delineated most easily in sections stained for cytochrome oxidase (CO) by the CO-light septa representing the passage of the cuneate fasciculus that runs dorsally, medially, and laterally to ICN, and by the presence of the trigeminal and gracile nuclei (Figure 1).

Genus	Case	Stain	Side	Degree	Recovery
Macaca	98_83	Nissl	Both	100%	1868
Macaca	99_26	CO	Right	Amputation	1825
Macaca	99_84	Nissl	Left	Extensive	1421
Macaca	02_56	CO	Both	N/A	N/A
Macaca	14_26	Nissl	Both	N/A	N/A
Macaca	14_43	Nissl, NeuN	Both	N/A	N/A
Otolemur	16_22	CO	Left	Amputation	1000
Otolemur	02_71	CO	Both	N/A	N/A
Saimiri	12_30	NeuN	Left	22%	63
Saimiri	12_53	CO	Left	61.20%	365
Saimiri	13_24	CO	Left	73%	100
Saimiri	12_16	NeuN	Right	79%	57
Saimiri	12_61	NeuN	Right	82%	133
Saimiri	11_50	CO	Left	89.50%	414
Saimiri	11_57	NeuN	Right	90%	184
Saimiri	13_01	CO	Right	91%	14
Saimiri	11_22	CO	Left	95%	491
Saimiri	13_17	CO	Right	97%	14
Saimiri	12_15	NeuN	Right	98%	49
Saimiri	12_52	CO	Left	100%	14
Saimiri	13_35	NeuN	Right	100%	238
Saimiri	13_40	NeuN	Both	100%	102
Saimiri	11_49	NeuN	Left	Extensive	169
Saimiri	98_08	CO	Right	Extensive	400
Saimiri	13_52	Nissl, NeuN	Both	N/A	N/A
Saimiri	14_24	Nissl	Both	N/A	N/A
Saimiri	15_01	Nissl, NeuN	Both	N/A	N/A

Table 9. Specimens used in this study.
Rows show individual cases, indicating taxonomy, available stains, degree of trauma (spared nuclei are not listed for brevity), and the recovery period in days. Cytochrome oxidase (CO) stains were always available for each case and when listed alone indicates cases where only volumetric data were available for this study. Degree of trauma is indicated by percentage when quantitative data are available or the investigator's notes when not. Macaques (*Macaca*) and the galago (*Otolemur*) underwent trauma during development; all squirrel monkeys (*Saimiri*) were lesioned as adults. NeuN, antigen for neuronal nuclei; N/A indicates control specimens.

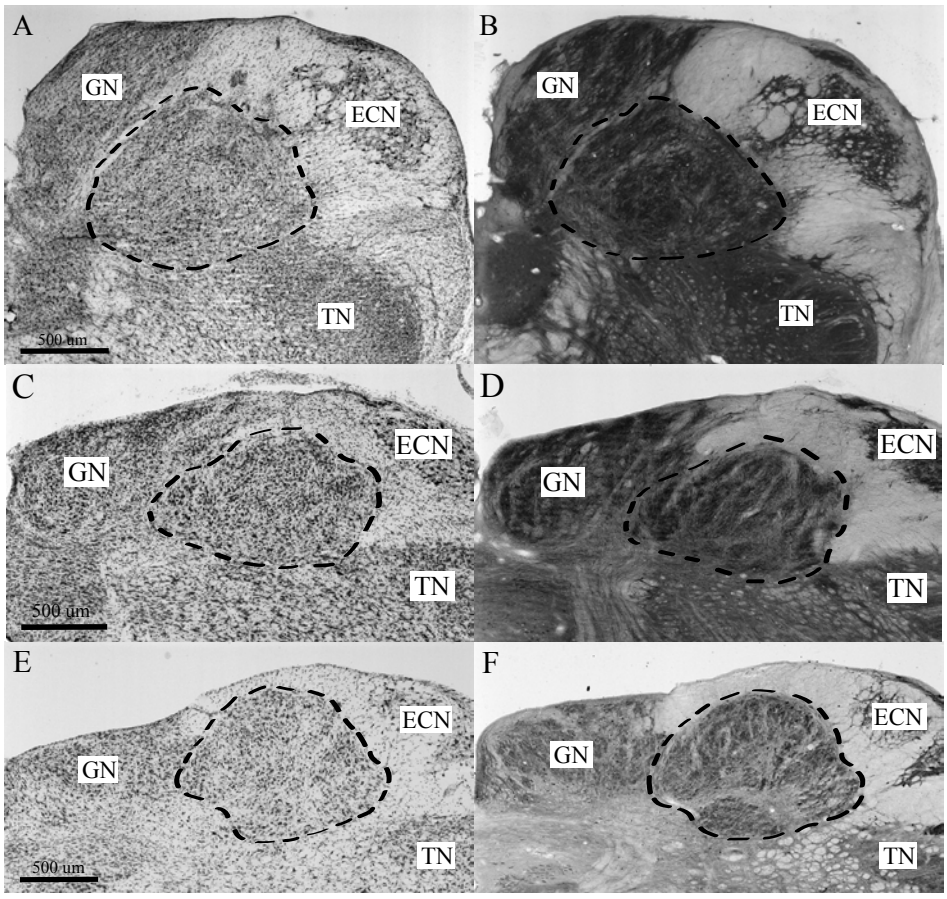

Figure 22. Low magnification images of the cuneate nucleus in control cases of each species included in this study.
Images taken near the obex, and dashed contour indicates the location and extent of the internal cuneate nucleus investigated in this project. Low magnification images of sections stained for Nissl substance (A, C, E) or CO (B, D, F), in macaques (*Macaca*, A, B), squirrel monkeys (*Saimiri*, C, D), and galagos (*Otolemur*, E, F). ECN, external cuneate nucleus; GN, gracile nucleus; TN, trigeminal nucleus. Scale bar is 500 μm.

We used Cavalieri's method to calculate the volume of the ICN bilaterally in each case, the average control values for which varied across species from 1.2 mm^3 in *Otolemur* to 2.1 mm^3 in *Saimiri* to 6.1 mm^3 in *Macaca*, and because values in controls were statistically indistinguishable from volume estimates for spared nuclei contralateral to the lesion (alpha = 0.05), we refer to control and spared nuclei as unaffected, and to partially or fully deafferented nuclei as affected (Table 2). We measured an average contralateral difference of 5.7% (SD = 2.1%) in control *Saimiri* specimens (n = 4), and found an average decrease in ICN volume following deafferentation of 22.5% (Table 2). We did not observe any statistically significant association between volume loss and lesion severity, which ranged from 22% to 100% (complete), or the time of recovery, which ranged from 14 to more than 400 days.

Macaca

	Average	SEM	CI_low	CI_high
Unaffected	6.073	0.2449	5.593	6.553
Affected	3.170	0.4749	2.239	4.100

Otolemur

	Average	SEM	CI_low	CI_high
Unaffected	1.247	0.0249	1.198	1.296
Affected	1.080	n/a		

Saimiri

	Average	SEM	CI_low	CI_high
Unaffected	2.131	0.0332	2.066	2.196
Affected	1.651	0.0870	1.480	1.821
Percent Change	-22.54%			

Table 10. Group measures and statistical evaluation of ICN regional volume following trauma. Table displays the average volume of the cuneate nucleus (mm^3) as measured using the Cavalieri method. Volumetric measurements of spared nuclei fell within the 95% confidence interval for controls in all species examined; this grouping is indicated as unaffected, whereas cases with trauma are indicated as affected. Percent change is calculated by subtracting the ratio of measures from one to depict change relative to measures from unaffected nuclei. SEM, standard error of the mean; CI, confidence interval (alpha = 0.05).

In our developmental sample (Table 3) of unilateral injury, we report smaller contralateral changes to regional volume in cases that underwent amputation (30.3% *Macaca* n=1; 12.9% *Otolemur*, n=1) than DCL (51.3% *Macaca*, n=1). In the case of bilateral developmental DCL, one side was 30% smaller than the other (3.41 mm^3 and 2.24 mm^3), and the average difference between these and control nuclei (mean = 6.13 mm^3, SD = 0.48 mm^3) was 53.9% (Table 3). The average difference in regional volume between developmentally affected and unaffected nuclei in *Macaca* was 45.2%, and the average difference between nuclei deafferented through amputation in this sample (*Macaca, Otolemur*) was 21.6%. In comparing developmental to adult DCL cases, we observed an approximately two-fold greater difference in shrinkage of 45.7% and 22.5%, respectively. Interestingly, the average effect of developmental amputation across species was similar to that of DCL in adults (~20%).

Macaca		
Average (n=4)	Control	6.13 +/- 0.48
99_84	DCL	2.64
99_84	Spared	5.41
Percent Change	vs Contralateral	-51.3%
98_83	DCL	3.41
98_83	DCL	2.24
Percent Change	vs Control	-53.9%
99_26	Spared	6.30
99_26	Amputation	4.39
Percent Change	vs Contralateral	-30.3%
Otolemur		
02_71	Control	1.28
02_71	Control	1.22
16_22	Amputation	1.08
16_22	Spared	1.24
Percent Change		-12.9%

Table 11. Regional volume of developmental sample in this study.
Table shows individual cases for each species where specimens underwent developmental trauma. Calculated percent change subtracted from 1 to depict direction of volume change. Control macaque values depict average +/- standard deviation.

Neuron Number

We used the optical dissector within a fractionator sampling scheme to estimate the number of neurons in this sample (see Methods, optical fractionator), and because we found that estimates from control nuclei were statistically indistinguishable (alpha = 0.05) from spared nuclei across species, we refer to this group as unaffected. We did not discover any statistically significant difference between the number of neurons in affected compared to unaffected nuclei in specimens that underwent trauma as adults (*Saimiri*, alpha = 0.05). In these adult cases, we estimated the mean neuron number to be 116,404, with a standard deviation (SD) of 6,497, and a standard error of the mean (SEM) of 2,165. In cases available for cell counts that underwent trauma during development (*Macaca*), we found an approximately 8% reduction in neuron number (Table 4). Specifically, our measurements revealed an average of 140,402 neurons, with a standard error of the mean (SEM) of 1,725, in unaffected nuclei, and in affected or deafferented nuclei, we estimated an average of 128,373 neurons, with a SEM of 2,075.

Macaca

	Mean	SEM	CI_low	CI_high
Unaffected	140,402	1,725	137,020	143,783
Affected	128,373	2,075	124,305	132,440
Percent Difference	-8.57%			

Table 12. Number of neurons following injury during development in macaque monkeys.
Table shows estimates neuron number using the optical fractionator. Percent difference is calculated by subtracting the ratio of measures from one to depict direction and magnitude of change relative to unaffected nuclei. SEM, standard error of the mean; CI, confidence interval calculated at the 95% level (alpha = 0.05).

Neuronal Volume

We used the nucleator principle to estimate the size of neurons encountered while performing counts using the optical fractionator. Our measurements revealed an approximately 20% reduction in neuronal volume following DCL, whether administered during development or in adults (Table 5, alpha = 0.05). Specifically, we found that affected ICN neurons in *Macaca* shifted from an average of about 2,600 μm^3 to around 2,000 μm^3 (change in averages of 21.4%), and that affected ICN neurons in *Saimiri* changed from around 2,000 μm^3 to approximately 1,600 μm^3 (change in averages of 22.3%), following DCL.

Macaca

	Average Vol	SEM	CI_low	CI_high
Unaffected	2,589.1	261.2	2,077.3	3,101.0
Affected	2,034.1	141.9	1,756.0	2,312.2
Percent Change	-21.44%			

Saimiri

	Average Vol	SEM	CI_low	CI_high
Unaffected	2,081.8	217.0	1,656.5	2,507.2
Affected	1,616.6	169.9	1,283.5	1,949.7
Percent Change	-22.35%			

Table 13. Volume of neurons within the cuneate nucleus following injury.
Table displays the volume of neurons (μm^3) within the cuneate nucleus as measured using the nucleator. Measurements of neurons within spared nuclei fell within the 95% confidence interval for controls in both *Macaca* and *Saimiri*, this grouping is indicated as unaffected, whereas cases with trauma are indicated as affected. Percent change is calculated by subtracting the ratio of measures from one to depict change relative to measures from unaffected nuclei. SEM, standard error of the mean; CI, confidence interval (alpha = 0.05, critical value = 1.96).

In addition, we found that the change in average neuronal volume followed a time-course, such that significant neuronal volume loss only really started to appear after approximately 60 days post-lesion (Figure 2).

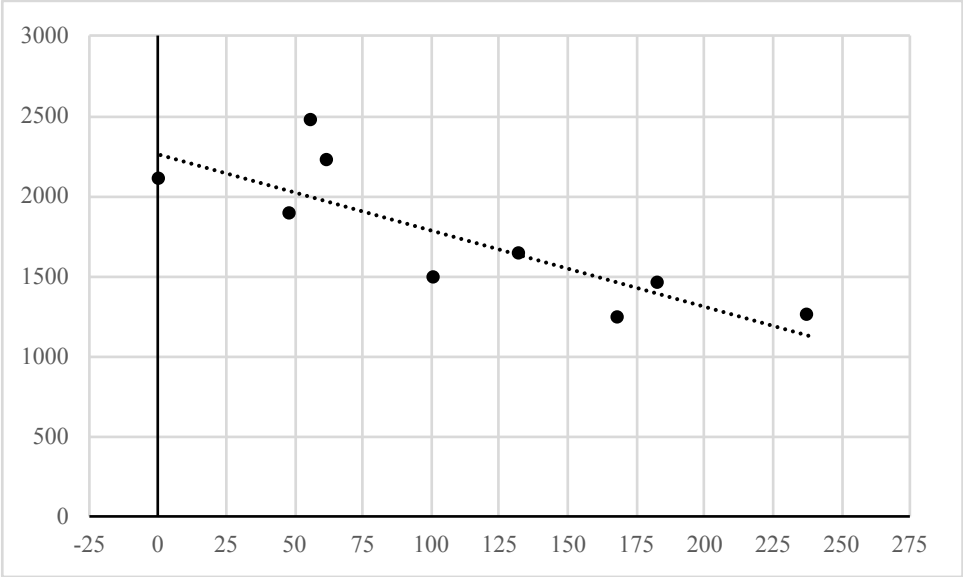

Figure 23. Neuronal volume loss over time following adult lesions.
Graph depicts the loss of neuronal volume (μm^3 along Y-axis) within affected nuclei over recovery period (time in days along X-axis). Average volume of neurons in unaffected nuclei depicted at day 1. Equation calculated excluding unaffected values: slope = -5.4025; intercept = 2,360.9; $R^2 = 0.679$.

Finally, we also found a significant change in the average skew of our neuron volume estimates in affected compared to unaffected nuclei following trauma during development (*Macaca*), but not in adult (*Saimiri*) DCL (Table 6, alpha = 0.05).

Macaca

	Average Skew	**SEM**	**CI_low**	**CI_high**
Unaffected	1.495	0.366	0.776	2.213
Affected	2.208	0.279	1.662	2.754

Saimiri

	Average Skew	**SEM**	**CI_low**	**CI_high**
Unaffected	1.475	0.384	0.722	2.227
Affected	1.571	0.395	0.796	2.346

Table 14. Skew of neuronal volume estimates.
Table shows changes to the average skew of neuronal populations measured using the nucleator in affected compared to unaffected ICN nuclei.

Discussion

Our results are the first to indicate in nonhuman primates the differential influence of the timing of trauma on the primary transneuronal atrophy that is known to follow chronic deafferentation within the mammalian somatosensory system. In particular, our measurements document a nearly two-fold greater change in the regional volume, differential neuron loss, and a shift in the distribution of neuronal volumes within nuclei deafferented through DCL during development compared to as adults.

In general, damage to afferent sensory circuits such as occurs in nerve transection, or after the removal of a peripheral structure like the eye or a limb, initiates a series of molecular events that, although not completely understood, culminates in gross anatomical changes in regional volume, neuronal morphology, and neuron number (Cowan, 1970; Kaas et al., 1983; Darian-Smith, 2009). The modulation of cellular microstructure following trauma, or transneuronal atrophy, has been recognized for more than a century (earliest reports describe transneuronal "degeneration"), from changes in the coloring of cells (Cook et al., 1951; Warrington, 1898) to the loss of dendrites (Powell, 1967) to changes in the chemistry and volume of entire anatomical regions (Avendano & Dykes, 1996a; 1996b; Jacquin & Rhoades, 1985; Loewy, 1973; Rhoades et al., 1993; Woods et al., 2000). Indeed, anatomical transneuronal atrophy has been observed across a variety of mammalian species following deafferentation in the visual (Cook et al., 1951; Matthews et al., 1966; Sloper et al., 1987), olfactory (Matthews & Powell, 1962; Powell, 1967), auditory (Powell & Erulkar, 1962), and somatosensory (Avendano & Dykes, 1996a; 1996b; Jacquin & Rhoades, 1985; Rhoades et al., 1993) systems. These observations accompany the larger body of work investigating the physiological consequences of peripheral trauma (see reviews by Cowan, 1970; Cusick, 1996; Darian-Smith, 2009; Jacquin & Rhoades, 1985; Kaas et al., 1983; Reed et al., 2016), and together form the basis of our understanding of the neurobiological plasticity that may mediate any recovery process useful in guiding therapeutic strategies in humans (Rowland et al., 2008). Despite the widespread observation of concerted changes following peripheral trauma in mammals, questions remain regarding the exact impact upon neuroanatomical plasticity that different types of trauma produce, particularly when they occur at different periods in development, and in species with subtle, but known, differences in circuitry (Cusick, 1996; Darian-Smith, 2009; Reed et al., 2016). Regardless, transneuronal atrophy is ubiquitous and represents an important factor in the activity-dependent reorganization of all sensory systems.

Our report of 1.2 mm^3 for the ICN in *Otolemur* is the first stereological report on the volume of this structure for this species. The mean measured volume of the ICN in our sample of macaques (*Macaca radiata*) ranged from less than 3 mm^3 in affected to just over 6 mm^3 in unaffected nuclei, slightly less on average than in a previous stereological study of the ICN in macaque monkeys (*Macaca fascicularis*), but well within the range of expected values for 6 of the 7 cases (Woods et al., 2000). Despite heterogeneity in our sample of two macaques with developmental DCL, one with unilateral and the other with bilateral trauma, we discovered a similar average decrease in ICN volume as the Woods et al (2000) study of around 50%. Previous work studying the effect of developmental nerve ablation in the rodent trigeminal system found that deafferentation resulted in regional volume loss ranging from 24% to 32% (Jacquin & Rhoades, 1985). Additional work in rodents investigating the effects of developmental forelimb amputation has revealed a similar range of average regional volume loss in the cuneate nucleus following deafferentation of between 19% (Bowlus et al., 2003), and 37% (Rhoades et al., 1993). In our sample of primates, we found an effect of therapeutic developmental amputation on ICN volume of around 13% (*Otolemur* n=1) and 30% (*Macaca* n=1), much lower than our own as well as previously published effects of developmental lesions (~50%; Woods et al., 2000). It should be noted that, in rodent studies, amputations and lesions are done quite early (postnatal day 1 or during embryonic development), and that trauma in these primate samples generally occurred after a few postnatal months (Taub, 1980). Distinctions in the developmental timing of trauma aside, these observations suggest differences between primates and rodents in the anatomy of this circuitry may play an important role in determining the volumetric effects of deafferentation (Kaas et al., 1983; Darian-Smith, 2009).

The mean measured volume of the ICN in our sample of squirrel monkeys (*Saimiri*) that underwent DCL as adults was approximately 2 mm^3, and is the first stereological report of the volume of this structure in this species. We measured an average decrease in ICN volume following deafferentation of 22.5%. This estimate agrees well with earlier work in the macaque where the effect of dorsal column lesions to the gracile fasciculus in adults was reported to reduce regional nuclear volume by about 20% (Loewy, 1973). Previous stereological work investigating the effects of peripheral nerve transection in the adult cat cuneate nucleus found similar shrinkage, reporting a range of 11% to 23% shrinkage following deafferentation (Avendano & Dykes, 1996b). Interestingly, work in rodents to compare the effect of peripheral limb amputation during development to that in adults found no statistically significant difference in the volume of the cuneate nucleus following deafferentation in adults (Bowlus et al., 2003). A few major methodological differences between the cat and primate studies compared to the work in rodents may help explain the difference between these reports. First, as opposed to the rodent studies, the cat and primate work deployed stereological methods (Avendano & Dykes, 1996b; Bowlus et al., 2003). Second, and perhaps most poignantly, these studies report effects following different types of deafferentation. Specifically, the previous work in rodents investigated the effect of amputation, whereas the cat and primate results are reported differences following nerve transection or DCL. Given the difference in shrinkage that we observed following DCL (~50%) compared to amputation (~22%) in developmental cases, and the nearly two-fold difference we found when comparing DCL during development to the same trauma in adults, plus the fact that even with stereological methods a variance in estimates of 8% is not unrealistic, it is possible that methodological differences account for the majority of this discrepancy in reported volumetric results following deafferentation in adults, and that some species differences explain any remainder. Together, this research shows a significant decrease in regional volume following deafferentation of the cuneate nucleus by nervous system lesion in adult mammals.

As neurons constitute the basic functional unit of neural circuits, determining whether neurons are lost following trauma has been a primary directive of basic research seeking to provide guidance to therapeutic strategies in the clinic. Our results did not reveal any significant loss of neurons following DCL in adult monkeys (*Saimiri*), similar to a previous stereological study of nerve transection in the adult cat (Avendano & Dykes, 1996b). On the other hand, we did discover a loss of approximately 8% of neurons following DCL during development in the macaque (*Macaca radiata*). These results agree with previous research in the macaque (*Macaca fascicularis*) that underwent extensive dorsal rhizotomies during development and exhibited a decrease in the number of neurons in deafferented cuneate nuclei of approximately 10% (Woods et al., 2000). Together, these results indicate a small but significant loss of neurons in the cuneate nuclei of macaque monkeys that underwent extensive deafferentation during development, and suggests important differences in the timing of trauma affects somatosensory system plasticity and the process of recovery.

Measures of transneuronal atrophy have often focused on changes in cellular morphology following deafferentation, not in small part because cellular or microstructural changes are likely to be a driving force in the reduction of gross regional nuclear volume, but because dendritic and axon collateral remodeling must underlie the pronounced and often immediately observable changes in receptive field properties that follow deafferentation (Kaas et al., 1983; Reed et al., 2016). For example, immediately after lesion, neurons in the cuneate nucleus are silent, only regaining receptive fields after weeks post-trauma that correlate with behavioral recovery and the sprouting of collaterals in spared axons representing nearby receptive fields which lead to a consolidation of the body map over months following deafferentation (Darian-Smith, 2009; Kambi et al., 2014). Although the specific molecular cascades which mediate these processes are not completely understood, anatomical observations have long suggested the importance of modulating dendritic arbors (Powell, 1967; Jones & Schallert, 1992), axon terminal ramifications (Antonini et al., 1998; Antonini & Stryker, 1993), and the expression of neuromodulators in studies of nervous system plasticity (Avendano & Dykes, 1996a; Castro-Lopez et al., 1993; Ralston et al., 1997). Furthermore, the time courses of molecular, cellular and gross anatomical changes in different systems and structures are not well understood (Cowan, 1970; Darian-Smith, 2009).

In our sample, we used the nucleator principle to estimate the mean radius of neurons in order to estimate the total volume of each neuronal body (see Methods). We discovered a similar, significant effect of DCL on the average estimate of neuronal volume following deafferentation during development (*Macaca*, 21.4%) or in adults (*Saimiri*, 22.3%). These observations largely agree with previous work investigating change in the volume of neurons (10-44%) in macaques following multiple years of recovery after extensive dorsal rhizotomies during development (Woods et al., 2000). Early work investigating the effect of DCL in adult macaques found similar changes in the volume of neurons (24%) within the gracile nucleus after 6 months (Loewy, 1973). Previous work on the effect of peripheral forelimb nerve transection in the adult cat also reported similar changes in neuronal volume (15%), noting that this effect lagged behind changes in regional volume, becoming more pronounced over the time interval sampled (up to 36 weeks; Avendano & Dykes, 1996b). This observation agrees with the findings of the Woods et al (2000) study, which described a linear relationship between recovery time and increasingly reduced neuronal volumes. We discovered a similar, slightly less dramatic, effect of increasingly shrunken neurons as survival time lengthened, but only in our sample of adult DCL (*Saimiri*). In addition, we report a delayed onset of decrease in the average neuron volume (somewhere between 63 and 100 days, or 9-14 weeks in *Saimiri*) that is similar to but slightly longer than the 9 weeks reported by the Avendano & Dykes (1996b) study of adult cat nerve transection. Finally, we also report a shift in the distribution of neuron volumes characterized by the skew of the sampled population (see Methods), such that neurons in nuclei deafferented during development by DCL (*Macaca*) contained a greater number of small neurons along with a smaller number of increasingly large neurons. Avendano & Dykes (1996b) report this effect following lesion in adult cats, whereas in our sample this effect only reached significance in the developmental DCL macaque cases. Taken together, these observations document some of the profound changes visible in the morphology of deafferented neurons of the somatosensory brainstem, and furthermore provide evidence of the more dramatic effects which follow deafferentation during development, suggesting therapy for spinal cord injuries may need distinct strategies to achieve optimal success following different types of trauma occurring during development or in adults.

In summary, our results sit at the intersection between previous studies in mammals, and go beyond confirming and extending previous observations of the effects of deafferentation on regional and cellular anatomy to provide some of the first evidence for significant differences in the effect of alternative types of trauma in three primate species. Finally, we also provide novel evidence of the differential effects of deafferentation at distinct periods of development that may help guide future therapeutic strategies aimed at optimizing the recovery of manual dexterity in humans with spinal cord trauma.

References

Angelucci A, Clasca F, Sur M. (1996). Anterograde axonal tracing with the subunit B of cholera toxin: a highly sensitive immunohistochemical protocol for revealing fine axonal morphology in adult and neonatal brains. J Neurosci Methods. 65(1):101–112.

Antonini A, Stryker MP. (1993). Rapid remodeling of axonal arbors in the visual cortex. Science. 260:1819–1821.

Antonini A, Gillespie DC, Crair MC, Stryker MP. (1998). Morphology of single geniculocortical afferents and functional recovery of the visual cortex after reverse monocular deprivation in the kitten. J Neurosci. 18:9896 –9909.

Aldskogius H, Arvidsson J. (1978). Nerve cell degeneration and death in the trigeminal ganglion of the adult rat following peripheral nerve transection. J Neurocytol. Apr;7(2):229-50.

Arvidsson J, Grant G. (1979). Further observations on transganglionic degeneration in trigeminal primary sensory neurons. Brain Res. Feb16;162(1):1-12.

Avendańo C, RW Dykes. (1996a). Evolution of morphological and histochemical changes in the adult cat cuneate nucleus following fore-limb denervation. J Comp Neurol. 370:479490.

Avendańo C, Dykes RW. (1996b). Quantitative analysis of anatomical changes in the cuneate nucleus following forelimb denervation: A stereological morphometric study in adult cats. J Comp Neurol. 370: 491–500.

Bowlus TH, Lane RD, Stojic AS, Johnston M, Pluto CP, Chan M, Chiaia NL, Rhoades RW. (2003). Comparison of reorganization of the somatosensory system in rats that sustained forelimb removal as neonates and as adults. J Comp Neurol. Oct 20;465(3):335-48.

Carson LV, Kelahan AM, Ray RH, Massey CE, Doetsch GS. (1981). Effects of early peripheral lesions on the somatotopic organization of the cerebral cortex. Clin Neurosurg. 28:532–546.

Castro-Lopes JM, Tavares I, Coimbra A. (1993). GABA decreases in the spinal cord dorsal horn after peripheral neurectomy. Brain Res. 1993;620:287–91.

Cook WH, Walker JH, Barr ML. (1951). A cytological study of transneuronal atrophy in the cat and rabbit. J Comp Neurol. 94:267–291.

Cowan, WM. (1970). Anterograde and retrograde transneuronal degeneration in the central and peripheral nervous system. In Contemporary Research Methods in Neuroanatomy. WJH Nauta, SOE Ebbeson, editors. pp. 217-251.

Cusick CG. (1996). Extensive cortical reorganization following sciatic nerve injury in adult rats versus restricted reorganization after neonatal injury: implications for spatial and temporal limits on somatosensory plasticity. Prog Brain Res. 108:379–390.

Darian-Smith C. (2009). Synaptic plasticity, neurogenesis, and functional recovery after spinal cord injury. Neuroscientist. Apr;15(2):149-65.

Florence SL, Jain N, Posphichal MW, Beck PD, Sly DL, Kaas JH. (1996). Central organization of sensory pathways following peripheral nerve regeneration in fetal monkeys. Nature. 381:69–71.

Florence SL, Wall JT, Kaas JH. (1988). The somatotopic pattern of afferent projections from the digits to the spinal cord and cuneate nucleus in macaque monkeys. Brain Res. Jun 14;452(1-2):388-92.

Florence SL, Wall JT, Kaas JH. (1989). Somatotopic organization of inputs from the hand to the spinal gray and cuneate nucleus of monkeys with observations on the cuneate nucleus of humans. J Comp Neurol. Aug 1;286(1):48-70.

Garcia-Cabezas MA, John YJ, Barbas H, Zikopoulos B. (2016). Distinction of Neurons, Glia and Endothelial Cells in the Cerebral Cortex: An Algorithm Based on Cytological Features. Front Neuroanat. Nov 1;10:107.

Gundersen HJG, Bagger P, Bendtsen TF, Evans SM, Korbo L, Marcussen N, Moller A, Nielsen K, Nyengaard JR, Pakkenberg B, Sorensen FB, Vesterby A, West MJ. (1988). The new stereological tools:

disector, fractionator, nucleator and point sampled intercepts and their use in pathological research and diagnosis. APMIS. 96:857–881.

Jacquin MF, Rhoades RW. (1985). Effects of neonatal infraorbital lesions upon central trigeminal primary afferent projections in rat and hamster. J Comp Neurol. May 1;235(1):129-43.

Jones EG. (2000). Cortical and subcortical contributions to activity-dependent plasticity in primate somatosensory cortex. Annu Rev Neurosci. 23:1-37.

Jones TA, Schallert T. (1992). Overgrowth and pruning of dendrites in adult rats recovering from neocortical damage. Brain Res. 581:156–60.

Juliano SL, Eslin DE, Tommerdahl M. 1994. Developmental regulation of plasticity in cat somatosensory cortex. J Neurophysiol. 72:1706–1716.

Kaas JH. 1994. The reorganization of sensory and motor maps in adult mammals. In: Gazzamiga MS, editor. The cognitive neurosciences. Cambridge: MIT Press. p 51–71.

Kaas JH, Merzenich MM, Killackey HP. (1983). The reorganization of somatosensory cortex following peripheral nerve damage in adult and developing mammals. Annu Rev Neurosci. 6:325-56.

Kaas JH, Qi HX, Burish MJ, Gharbawie OA, Onifer SM, Massey JM. (2008). Cortical and subcortical plasticity in the brains of humans, primates, and rats after damage to sensory afferents in the dorsal columns of the spinal cord. Exp Neurol. Feb;209(2):407-416.

Kambi N, Halder P, Rajan R, Arora V, Chand P, Arora M, Jain N. (2014). Large-scale reorganization of the somatosensory cortex following spinal cord injuries is due to brainstem plasticity. Nat Commun. 5:3602.

Kalaska J, Pomeranz B. (1979). Chronic paw denervation causes an age-dependent appearance of novel responses from forearm in “paw cortex” of kittens and adult cats. J Neurophysiol. 42:618–633.

Kelahan AM, Doetsch GS. (1984). Time-dependent changes in the functional organization of somatosensory cerebral cortex following digit amputation in adult raccoons. Somatosens Res. 2:49–81.

Kelahan AM, Ray RH, Carson LV, Massey CE, Doetsch GS. (1981). Functional organization of adult raccoon somatosensory cerebral cortex following neonatal digit amputation. Brain Res. 223:151–159.

Koo TK, Li MY. (2016). A guideline of selecting and reporting intraclass correlation coefficients for reliability research. J Chiropr Med. Jun; 15(2):155-63.

Liao CC, DiCarlo GE, Gharbawie OA, Qi HX, Kaas JH. (2015). Spinal cord neuron inputs to the cuneate nucleus that partially survive dorsal column lesions: A pathway that could contribute to recovery after spinal cord injury. J Comp Neurol. Oct 1;523(14):2138-60.

Liao CC, Reed JL, Kaas JH, Qi HX. (2016). Intracortical connections are altered after long-standing deprivation of dorsal column inputs in the hand region of are 3b in squirrel monkeys. J Comp Neurol. May 1;524(7):1494-526.

Loewy AD. (1973). Transneuronal changes in the gracile nucleus. J Comp Neurol. Feb 15;147(4):497-510.

Matthews MR, Powell TPS. (1962). Some observations on transneuronal cell degeneration in the olfactory bulb of the rabbit. J Anat. 96:89–102.

Matthews MR, Cowan WM, Powell TPS. (1966). Transneuronal cell degeneration in the lateral geniculate nucleus of the macaque monkey. J Anat. 94:145–169.

McKinley PA, Smith JL. (1990). Age-dependent differences in reorganization of primary somatosensory cortex following low thoracic (T12) spinal cord transection in cats. J Neurosci. 10:1429–1443.

Moore CI, Stern CE, Dunbar C, Kostyk SK, Gehi A, Corkin S. (2000). Referred phantom sensations and cortical reorganization after spinal cord injury in humans. Proc Natl Acad Sci U S A. Dec 19;97(26):14703-8.

Mountcastle, VB. (2005). The Sensory Hand. Harvard Univ Press; Cambridge, MA.

Mullen RJ, Buck CR, Smith AM. (1992). NeuN, a neuronal specific nuclear protein in vertebrates. Development. 116(1):201-11.

Powell TPS. (1967). Transneuronal cell degeneration in the olfactory bulb shown by the Golgi method. Nature. 215:425–426.

Powell TPS, Erulkar SD. (1962). Transneuronal cell degeneration in the auditory relay nuclei of the cat. J Anat. 96:249–268.

Qi HX, Gharbawie OA, Wong P, Kaas JH. (2011). Cell-poor septa separate representations of digits in the ventroposterior nucleus of the thalamus in monkeys and prosimian galagos. J Comp Neurol. 519(4):738–758.

Qi HX, Gharbawie OA, Wynne KW, Kaas JH. (2013). Impairment and recovery of hand use after unilateral section of the dorsal columns of the spinal cord in squirrel monkeys. Behavioural brain research. 2013; 252:363–376.

Ralston D, Behbehani S, Sehlhorst S, Meng X-W, Ralston H. (1997). Immunoreactivity in the dorsal horn of the rat following partial constriction of the sciatic nerve correlates with the behavioral manifestation of pain: a light and electron microscopic study. Prog Pain Res Mgmt. Seattle: I.A.S.P. Press; p. 547-60.

Ramachandran VS, Hirstein W. (1998). The perception of phantom limbs. The D. O. Hebb lecture. Brain. 121:1603–1630.

Reed JL, Liao CC, Qi HX, Kaas JH. (2016). Plasticity and recovery after dorsal column spinal cord injury in nonhuman primates. J Exp Neurosci. Aug 18;10(Suppl 1):11-21.

Renehan WE, Klein BG, Chiaia NL, Jacquin MF, Rhoades RW. (1989). Physiological and anatomical consequences of infraorbital nerve transection in the trigeminal ganglion and trigeminal spinal tract of the adult rat. J Neurosci. Feb;9(2):548-57.

Rhoades RW, Wall JT, Chiaia NL, Bennet-Clarke CA, Killackey HP. (1993). Anatomical and functional changes in the organization of the cuneate nucleus of adult rats after fetal forelimb amputation. J Neurosci. Mar;13(3):1106-19.

Rowland JW, Hawryluk GW, Kwon B, Fehlings MG. (2008). Current status of acute spinal cord injury pathophysiology and emerging therapies: promise on the horizon. Neurosurg Focus. 25(5):E2.

Schmitz, C, Hof, PR (2005) Design-based stereology in neuroscience. J Neurosci. 130: pp. 813-831.

Sloper J, Headon MP, Powell TP. (1987). Effects of enucleation at different ages on the sizes of neurons in the lateral geniculate nucleus of infant and adult monkeys. Brain Res. 428:259–265.

Strata F, Coq JO, Kaas JH. (2003). The chemo- and somatotopic architecture of the Galago cuneate and gracile nuclei. J Neurosci. 116(3):831-50.

Waite PM. (1984). Rearrangement of neuronal responses in the trigeminal system of the rat following peripheral nerve section. J Physiol. 352:425–445.

Wall JT, Cusick CG. (1984). Cutaneous responsiveness in primary somato- sensory (S-I) hindpaw cortex before and after partial hindpaw deaffer- entation in adult rats. J Neurosci. 4:1499–1515.

Wall JT, Cusick CG. (1986). The representation of peripheral nerve inputs in the S-I hindpaw cortex of rats raised with incompletely innervated hindpaws. J Neurosci. 6:1129–1147.

Warrington WB. (1898). On the structural alterations observed in nerve cells. J. Physiol. (London), 23:112-129.

Wolf HK, Buslei R, Schmidt-Kastner R, et al. (1996). NeuN: a useful neuronal marker for diagnostic histopathology. J Histochem Cytochem. 44(10):1167–1171.

Wong-Riley M. (1979). Changes in the visual system of monocularly sutured or enucleated cats demonstrable with cytochrome oxidase histochemistry. Brain Res. 171(1):11–28.

Woods TM, Cusick CG, Pons TP, Taub E, Jones EG. (2000). Progressive transneuronal changes in the brainstem and thalamus after long-term dorsal rhizotomies in adult macaque monkeys. J Neurosci 20:3884–99.

CHAPTER 5

CONCLUDING REMARKS

Summary

The aim of the present research was to evaluate the differential effect of specific methodological decisions to visualize regions and objects of interest in order to optimize the subsequent analysis of two archival collections where the type, number, and size of regions or objects of interest is thought to broadly correlate with circuit function. We thus pursued a few main questions, the first of which concerned the primary trade-off in quantitative studies of anatomy, and how to best mitigate or cross-validate different measurements. Subsequently, we investigated changes in the density of cell subtypes in the primary visual cortex of primates adapted to vision in low compared to high levels of light. Finally, we investigated the changes in cellular morphology of the somatosensory brainstem that follow primary deafferentation.

In this research, we found that the primary trade-offs in quantitative studies of neuroanatomy primarily concern the speed and reliability of acquiring information at the cost of precision. In particular, we found that faster, destructive methods necessitate the loss of spatial information, although improvements to the precision of estimates may follow, although different estimates are impacted by different factors (e.g. slice vs dissolution preparations; cellular morphology vs immunolabeling in histological procedures). In studies where spatial information is paramount, highly reliable estimates may be obtained, but at the cost of increasingly sophisticated experimental design and an increase in time of labor. In summary however, many of the issues confronted when pursuing anatomical studies of the nervous system may be mitigated by foreknowledge of the indices to be investigated, and clear goals for the desired results.

In pursuit of the second question, we found agreement with emerging work to show that metabolic indices of circuit function are available through quantitative analysis of the cellular composition of specific neural pathways. In particular, we found that shifts in the cellular composition of cortical circuitry reveals phyletic modifications in the primate visual system related to high (diurnal) or low light (nocturnal) ecologies. Thus, information regarding the cellular composition of entire brain regions reveals deviation from broader scaling rules suggestive of physiological modifications to sensory systems.

Pursuant to the third goal of this work, we confirmed previous research regarding the main effects of deafferentation in the somatosensory neuraxis, extended these observations to species which had previously not been investigated, and found novel evidence of the differential effect of injury during development compared to adulthood. In particular, we found larger effects upon the cellular morphology of neurons deafferented during development than adulthood, and discovered shifts in the distribution of neuron volumes previously observed in cats but not known to be present in primates, as well as to provide evidence of this effect over a longer period of time following injury. Thus, our investigation of the anatomical indices available to infer the effects of deafferentation confirmed and extended previous observations, as well as providing novel insights into the time course of this effect in primates.

In conclusion, this dissertation provided evidence of the relationship between brain structure and function, such that trends in the evolution of primate vision were confirmed and extended to a greater number of species than had previously been investigated, as well as to reveal the re-organization that occurs following injury in the somatosensory system and supports the retention of the somatotopy critical to behavioral recovery following spinal cord injury.

Future Directions

In this dissertation, we sought fundamental structural information about the organization of the visual system in a diverse sample of primates, as well as the reorganization of the brainstem nucleus that supports touch after deafferentation. Our results only reveal small pieces of the much larger variance in the anatomical structures which support vision across the primate order, and answers only basic questions about the effect of the timing of injury on the cellular morphology of deafferented nuclei. Indeed, this work focused on the cellular anatomical changes associated with broad, sweeping changes in animal behavior and the recovery of behavior following injury to primary spinal cord pathways. Although these results may represent the first of their kind, they reflect a myriad of molecular changes and furthermore can only be loosely associated with physiological measurements. The results of this investigation thus provide a stepping stone to a more nuanced understanding of the relationship between brain structure and function by providing data about the distribution and size of different cell subtypes.

This work provides quantitative estimates of observations known from previous qualitative investigations, revealing a complex relationship exists between the density of cell subtypes and the physiological role of cortical layers. In particular, although we identify a 30% increase in the density of cells in the primary thalamorecipient layer 4 of the visual cortex in diurnal compared to nocturnal primates, and know that the majority of this change is due to increased neuron number, additional information about the number and distribution of neuron subtypes is important to understanding the physiological impact of this observation. For example, the size and orientation of the dendritic arbors of neuron subtypes may have subtle effects upon circuit function, as does variance in the projection pattern of each cell subtype. Similarly, more information about neuron subtypes may be gleaned from analyses of the distribution of genes and gene products than from cellular morphology, leaving open questions of the specific impact of phyletic changes in the molecular profile of cell subtypes within cortical layers. Thus, one promising future direction for research is to investigate the molecular identity of neurons, and to thus test for differences in the cellular composition of cortical microstructure along multiple dimensions, such as the distribution of neurons exhibiting distinct pharmacological properties in addition to size and connections. In addition, analysis of the relationship between the primary thalamorecipient layer and the cortical mantle in a variety of cortical regions would help to resolve the question of how similar this layer is across regions, and whether or not variance in this layer underlies changing physiological dynamics across the mantle.

The results from this work also point to differences in the anatomy and physiology of somatosensory pathways serving the sense of touch following injury during development compared to as adults. However, some of our measures are related to each other in poorly understood ways that could be improved by physiological and genetic measurements. For example, our data reveal decreases in cell size and nuclear volume without being able to provide information about the similarity or distinctiveness of the underlying molecular causes. In addition, we were not able to provide more information about the changes in dendritic arbors of shrinking neurons, and if the same molecular events are triggered in fully compared to partially deafferented neurons. Our results also leave open questions about the specific physiological changes likely to follow deafferentation because we only provide information about the cellular anatomy and relatively gross information about each cell, whereas analyses at the level of the electron microscope could reveal changes in the arrangement of synapses and the expression of neurotransmitter subtypes. Thus, while our data answer a few basic questions about the impact of deafferentation on cellular morphology, many questions remain regarding the specific mechanisms underlying these changes, as well as their physiological impact.

Taking these observations together, the current work provides basic data on a limited number of anatomical features of interest, and which are only loosely correlated with known physiological changes. Subsequent research focusing on the genetic as opposed to morphological identity of cell subtypes will not only expand and enrich these fundamental observations, but will also provide insight into their pharmacology and physiology. It is also possible that cortical regions of interest may be more clearly delineated using a more broad array of genetic identities to characterize similar from distinct modules within the brain, and similarly that an analysis of the genetic identity of cells might reveal smaller and more subtle functional subdivisions within sensory systems.